Application of Caquot's solution to the analysis of stability of shallow circular cavities in Tresca material

A THESIS

SUBMITTED TO THE FACULTY OF THE

UNIVERSITY OF MINNESOTA

BY

Tyler J. Reich

IN PARTIAL FULFILLMENT OF THE REQUIREMENTS

FOR THE DEGREE OF

Master of Science

Professor Carlos Carranza-Torres (Advisor)

November, 2016

© Tyler J. Reich 2016

ALL RIGHTS RESERVED

This thesis has been typeset using the LaTeX system together with the University of Minnesota 'mnthesis.cls' style package. Figures have been produced using the software CorelDraw®. Diagrams have been produced using the software Grapher®, with numerical results generated using the software MathCad®. The mechanical models presented in this thesis have been produced using the software FLAC®.

Acknowledgements

I am very grateful to the University of Minnesota and the faculty and staff of the Swenson College of Science and Engineering. The time I spent exploring my interests as part of the inaugural class of Civil Engineering graduates at University of Minnesota, Duluth Campus, has embarked me on an exciting and engaging career. Most of all, I would like to thank Professor Carlos Carranza-Torres for supporting me during my research and guiding me throughout the process of developing this thesis.

Abstract

The primary objective of this study is to expand upon and investigate a statical admissible solution for the stability of shallow cavities proposed by Caquot in 1934. Despite its relevance, this solution appears to have been overlooked in the literature. In this thesis, Caquot's analytical model is re-formulated to express the stability condition of a shallow cavity (a section of long cylindrical tunnel or a spherical opening) in terms of a *factor of safety* using the *strength reduction technique*, as commonly done in the evaluation of stability of slopes, embankments and levees. Caquot's analytical model is also extended to account for the presence of a mechanical surcharge on the ground surface, water pressure in the ground, and two conditions of water presence inside the cavity, namely, dry or flooded cavities. For the purpose of this study, the plastic constitutive model assumed for the ground is the Tresca shear failure criterion. This material model is a particular case of the Mohr-Coulomb material model with zero internal friction angle and cohesive strength only. Closed-form solutions for computation of factor of safety under dry and saturated ground conditions are presented and the effect of input variables involved in the problem are evaluated. Since the developed analytical model is a static admissible solution, the values of factors of safety predicted with the solution are only conservative approximations of the 'true' values of factor of safety. Assuming that numerical finite element or finite difference models for which the size of elements in the mesh is fine enough will provide factors of safety values that are reasonably close to the 'true' ones, the results of factors of safety obtained with the closed-form solutions are compared (and the differences quantified) with those obtained with the commercial finite difference software FLAC®, a program that is widely used in the practical design of underground structures. The relatively small difference in results obtained with both methods (10% or less difference in values of factor of safety) suggests that the extended Caquot's solution presented in this thesis could be a valuable tool for practical

evaluation of stability conditions of circular cavities, such as sections of long cylindrical tunnels or spherical openings, excavated near the ground surface.

Contents

Acknowledgements **i**

Abstract **ii**

List of figures **vii**

1 Introduction **1**

1.1 Motivation of this thesis 1

1.2 Literature review on existing solutions of tunnel stability 3

1.2.1 Analytical models 3

1.2.2 Numerical models 11

1.2.3 Physical models 12

1.3 Objectives and structure of this thesis 14

2 Caquot's solution for dry ground **18**

2.1 Problem statement 18

2.2 Scaled form of Caquot's solution 22

2.3 Computation of factor of safety for Caquot's solution 24

2.4 Influence of input parameters on factor of safety 25

2.4.1 Influence of cavity depth 25

2.4.2 Influence of internal pressure 30
2.4.3 Influence of ground surcharge load 34

3 Extension of Caquot's solution accounting for water in the ground 38
3.1 Problem Statement 38
3.2 Scaled form of Caquot's solution 42
3.3 Computation of factor of safety for Caquot's solution 44
3.4 Comparison with cavity in dry ground 46
3.4.1 Case of water surface coinciding with ground surface 47
3.4.2 Case of water surface above ground surface 49
3.4.3 Case of water surface below ground surface 54

4 Comparison of Caquot's solution with numerical models 60
4.1 FLAC® models 60
4.2 Comparison of factors of safety obtained with analytical and numerical models 66
4.2.1 Cavity depth 67
4.2.2 Cavity type. Cylindrical and spherical cavities 70
4.2.3 Uniform vs. Caquot's internal pressure distribution 73
4.2.4 Density of the mesh in the numerical model 79

5 Conclusions 82

References 86

Appendix A. Derivation of Caquot's solution for dry ground 89
A.1 Solution of stresses along cavity crown-surface segment 90
A.2 Solution of stresses inside the integration circle 92

A.3 Compatibility of stresses at the boundary of the integration circle 93

Appendix B. Derivation of Caquot's solution accounting for water in the ground 96

B.1 Solution of stresses along cavity crown-surface segment 96

B.1.1 Case of water surface above or at ground surface 97

B.1.2 Case of water surface below or at ground surface 98

List of figures

1.1 Green Park London tunnel collapse, 1964 (after Clay & Takacs, 1997) 2

1.2 Lamé's solution for circular tunnel in elastic medium subjected to axi-symmetrical loading 4

1.3 Kirsch's solution for circular tunnel in elastic medium subjected to non-axi-symmetrical loading, where the far-field vertical stresses are different from the far-field horizontal stresses 5

1.4 Methods for performing stability analysis of geotechnical structures (e.g., slopes and foundations) —after Potts & Zdravkovic (1999) 7

1.5 Terzaghi's limit equilibrium model (after Terzaghi, 1943) 8

1.6 Stress field solution proposed by Caquot (1934) 8

1.7 Statically admissible plastic solution for a) cylindrical tunnel; and b) front of a tunnel regarded as a spherical cavity (after Davis et al., 1980) 10

1.8 Principal stresses and incremental displacements at failure for a tunnel front (after Vermeer, P.A. et al., 2002) 13

1.9 Tresca failure envelope represented in the 3D space of principal stresses 15

2.1 Extended Caquot model considered in this research as applied to the analysis of stability of shallow circular cavities in plastic material 19

2.2 Tresca failure envelope represented in the 2D space of principal stresses 20

2.3 Tresca failure envelope represented in the 2D space of shear and normal stresses 21

2.4 Relationship between factor of safety and scaled cohesion as a function of scaled depth for cylindrical cavities 26
2.5 Relationship between factor of safety and scaled cohesion as a function of scaled depth for spherical cavities 28
2.6 Relationship between scaled factor of safety and scaled cavity depth for cylindrical and spherical cavities 29
2.7 Relationship between factor of safety and scaled cohesion as a function of scaled internal pressure for cylindrical cavities 31
2.8 Relationship between scaled factor of safety and scaled internal pressure for cylindrical and spherical cavities 33
2.9 Relationship between factor of safety and scaled cohesion as a function of scaled ground surcharge load for cylindrical cavities 35
2.10 Relationship between scaled factor of safety and scaled ground surcharge load for cylindrical and spherical cavities 37
3.1 Extended Caquot model as applied to the analysis of stability of shallow cavities for the case of a water surface above the ground surface 39
3.2 Extended Caquot model as applied to the analysis of stability of shallow cavities for the case of a water surface below the ground surface 40
3.3 Relationship between factor of safety and scaled cohesion for the case of water surface coinciding with the ground surface, and cases of flooded and dry cavities. The case of dry ground is also represented for comparison 48
3.4 Relationship between factor of safety and scaled cohesion for the case of water surface above the ground surface, and cases of flooded and dry cavities. The case of dry ground is also represented for comparison 50

3.5 Relationship between scaled factor of safety and scaled water surface elevation considered to be above the ground surface, for the cases of flooded and dry cavities. The case of dry ground is also represented for comparison 53
3.6 Relationship between factor of safety and scaled cohesion for the case of water surface below the ground surface, and cases of flooded and dry cavities. The case of dry ground is also represented for comparison 57
3.7 Relationship between factor of safety and scaled cohesion for the case of water surface at the lowest elevation, and cases of flooded and dry cavities. The case of dry ground is also represented for comparison 58
3.8 Relationship between factor of safety and scaled cohesion for the case of water surface below the ground surface, and cases of flooded and dry cavities. The case of dry ground is also represented for comparison 59
4.1 Example of FLAC® model used to perform the numerical analysis component of this research 61
4.2 Strength reduction technique for the case when the given ground strength leads to a stable shallow excavation 63
4.3 Strength reduction technique for the case when the given ground strength leads to an unstable shallow excavation 64
4.4 Application of the strength reduction technique to the FLAC® models. The different plots show a sequence of reduction of ground strength. Shaded regions indicate elements behaving plastically 65
4.5 Comparison of numerical and analytical results for cylindrical cavities, using a similar representation as in Figure 2.4 68
4.6 Ratio of factors of safety obtained with numerical and analytical models, as represented in Figure 4.5 69

4.7 Comparison of numerical and analytical results for cylindrical and spherical cavities, using a similar representation as in Figures 2.4 and 2.5 71
4.8 Ratio of factors of safety obtained with numerical and analytical models for cylindrical and spherical cavities, as represented in Figure 4.7 72
4.9 Graphical representation of three cases of internal pressure considered for the numerical models. Case PD#1: Caquot's pressure distribution; Case PD#2: uniform pressure distribution; and Case PD#3: averaged uniform pressure distribution 74
4.10 Comparison of numerical and analytical results for the different cases of internal pressure distribution represented in Figure 4.9 77
4.11 Ratio of factors of safety obtained with numerical and analytical models, as represented in Figure 4.10 78
4.12 Ratio of factors of safety obtained with numerical and analytical models as a function of the element size considered in the numerical model mesh. 'Element size' refers to the side-length of the square elements in the 'inner region' of the mesh in Figure 4.1 81
A.1 Extended Caquot's model as applied to the analysis of stability of shallow circular cavities in plastic material, with particular reference to the stresses at the crown-surface segment A-B 91
A.2 Extended Caquot's model as applied to the analysis of stability of shallow circular cavities in plastic material, with particular reference to the stresses at the at the boundary of the integration circle 94

Chapter 1

Introduction

1.1 Motivation of this thesis

The stability of shallow circular tunnels in soils and rocks is an important and practical problem in geotechnical engineering. The shallow underground space in urban areas increases in value as surface space becomes more crowded. As more and more underground construction develops in the form of buried utilities and transportation tunnels, the importance of safe construction of these underground structures becomes paramount. The collapse of a shallow tunnel in an urban area is not only dangerous to the people involved in the tunnel construction, it is also dangerous to people and property above the ground surface.

There are several mechanical methods of tunnel excavation used to construct shallow tunnels including the *Earth Pressure Balance* and *Slurry Shield* methods. The application of these methods involves removing soil from the face of a tunnel using cutters attached to machinery that is advanced behind a shield. As the shield advances, support for the tunnel, typically in the form of a concrete liner, is placed behind the shield to protect the machinery and operators. Throughout this process, the shield must maintain a minimum pressure upon the face of the tunnel to prevent the formation of a cave at the front (Guglielmetti, Grasso, Mahtab,

& Xu, 2008). An example of a tunnel cave-in that occurred while implementing a shielded construction method is presented in Figure 1.1. This collapse occurred in the neighborhood of Green Park, London, in the United Kingdom in 1964. The construction method involved the use of a drum digger shield. During excavation of the tunnel, the crown of the shield penetrated through the London Clay into water bearing sand and gravel. This sand and gravel caved into the excavation, burying most of the shield.

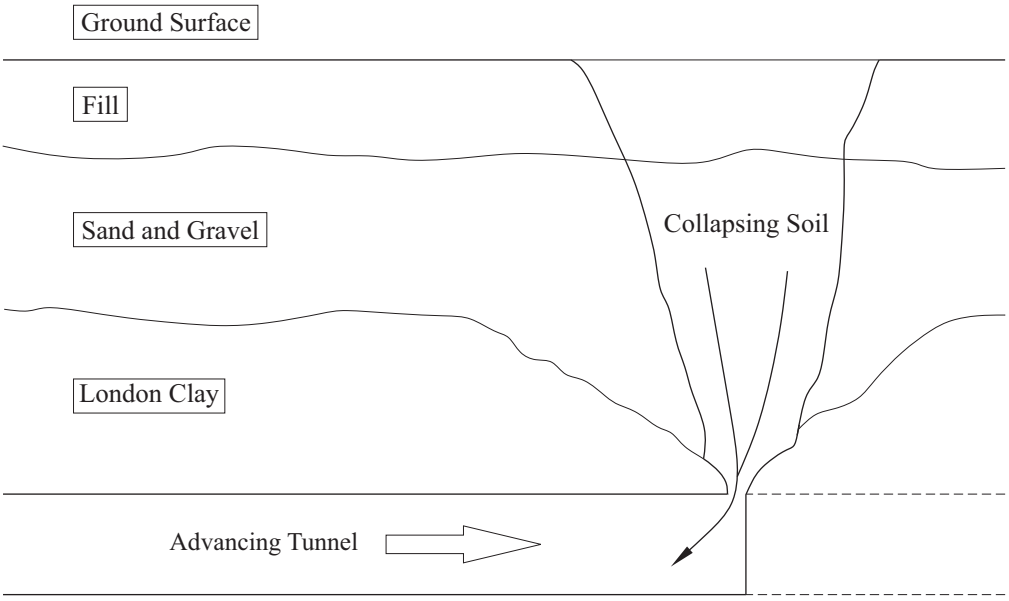

Figure 1.1: Green Park London tunnel collapse, 1964 (after Clay & Takacs, 1997)

Failures such as the one described above could be prevented by further investigating the relationship between support pressure, the properties of the ground around the excavation, and the geometry of the tunnel. These relationships can be explored through analytical and numerical modeling of the problem, allowing the examination of the dependance of different variables on shallow tunnel stability. Further understanding of the relationships among variables involved in the stability of shallow excavations, with the objective of understanding and preventing shallow tunnel collapses, is the main motivation of this thesis.

1.2 Literature review on existing solutions of tunnel stability

There are three primary methods used for the design of geotechnical structures. These methods are analytical, numerical and physical. This section includes a brief and general review of research related to the stability of shallow tunnels with regard to each of these methods. This review will focus on different methods and models that have been developed to analyze the stress and deformation states in the ground after excavation of tunnels. Additional research topics related to tunneling, which are also relevant to the developments in this thesis, will be discussed.

1.2.1 Analytical models

Several analytical models for excavation of tunnels have been developed to determine the redistribution of stresses and displacements that occurs in a soil (or rock) after excavation.

The simplest material constitutive behaviour that can be adopted for the ground is a linear elastic behaviour. Analytical models for tunnels in assumed elastic (homogenous and isotropic) media will be discussed first.

Lamé (1852) developed a closed form solution for the stresses and displacements in an infinite elastic medium around a cylindrical tunnel —see Figure 1.2. The solution is applicable when the far-field stresses acting in the medium (i.e., the stresses prior to excavation) are uniform and equal in all directions so axi-symmetry of loading exists.

Kirsch (1898) developed a solution for a problem similar to the one by Lamé —Figure 1.3. In the Kirsch's solution though, the far-field stresses acting vertically and horizontally in the medium are different. This is a useful consideration because in actual geotechnical situations, in-situ horizontal stresses are typically different from in-situ vertical stresses.

Stress distributions found through elastic analyses such as Lamé's solution or Kirsch's solution (or other existing solutions for tunnel shapes other than circular) are valuable tools for

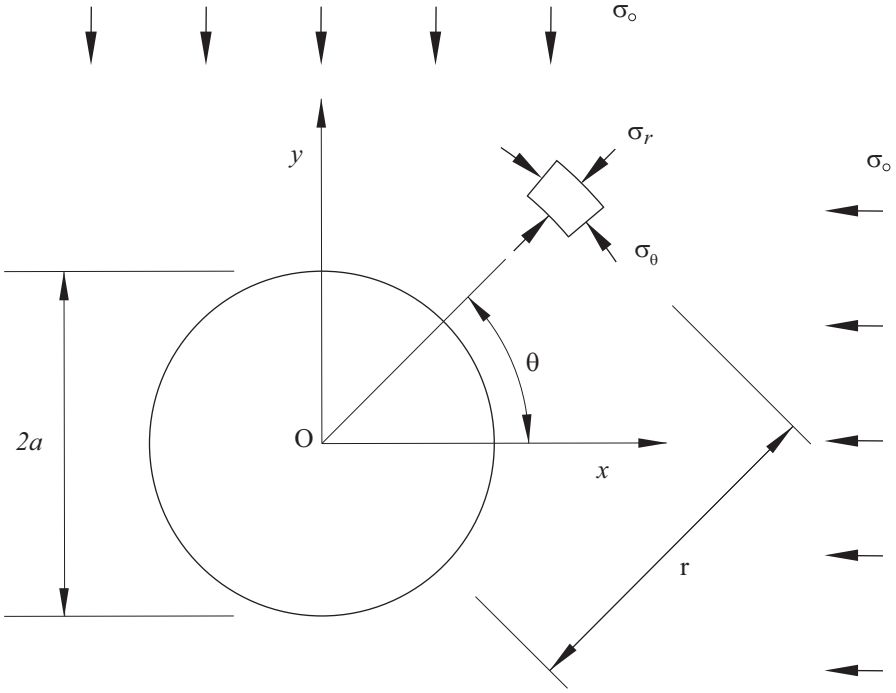

Figure 1.2: Lamé's solution for circular tunnel in elastic medium subjected to axi-symmetrical loading

determining critical areas where plastic deformation is likely to occur around an excavation, for example, if a more elaborated plastic model were to be considered for the ground, as it will be discussed later in this section.

With this regard, elliptical sections of tunnels were theorized to be the optimal design shape for tunnels excavated in ground subjected to high in-situ stresses having a large difference of vertical and horizontal stresses. The design consisted in taking a height-to-width ratio for the (elliptical) tunnel to be equal to the ratio of far-field stresses —considering the height-to-width ratio to be equal to the vertical (assumed major)-to-horizontal (assumed minor) ratio of principal far-field stresses. This design approach was referred to as the *harmonic* design of elliptical tunnels (Fairhurst & Carranza-Torres, 2002). Though if the behaviour of the material was indeed elastic the hoop stresses on the periphery of the elliptical section could be proved to be

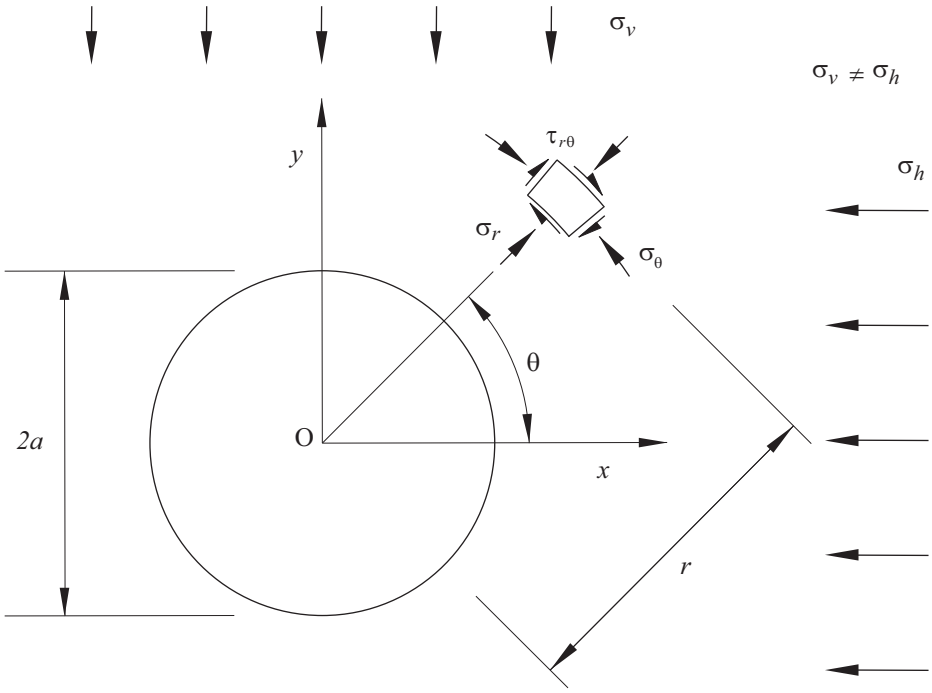

Figure 1.3: Kirsch's solution for circular tunnel in elastic medium subjected to non-axi-symmetrical loading, where the far-field vertical stresses are different from the far-field horizontal stresses

actually constant, Carranza-Torres (1998) presented numerical models revealing that highly non-uniform areas of hoop stresses and extent of plastic failure around the elliptical boundary were expected to occur if the ground was assumed to behave plastically. Therefore, if the ground was behaving plastically rather than elastically, the harmonic design of elliptical openings was not an optimum configuration to be considered.

A more elaborated material constitutive behavior that can be considered for the ground is a plastic or elasto-plastic behavior. In that case, when the strength of the material is low enough compared with the magnitude of (redistributed) loads, there is a region that fully (or partially) surrounds the tunnel boundary, where the redistribution of stresses causes permanent deformation. This is called the *plastic* zone. One of the most commonly used plastic models

for soils is the Mohr-Coulomb failure criterion (Terzaghi, 1943; Terzaghi et al., 1996; Coduto et al., 2011). Another common plastic model used for intact rock and rock masses is the Hoek-Brown failure criterion (Hoek & Brown, 1980, 1997; Brady & Brown, 2004). Since this thesis work pertains mostly to shallow cavities in soils, tunnels stability solutions applicable to Mohr-Coulomb material models will be emphasized.

Potts & Zdravkovic (1999), classify the available methods for performing stability analyses of geotechnical structures (e.g., slopes and foundations) as shown in Figure 1.4.

Lamé's solution and Kirsch's solution described earlier on are examples of *closed-form* methods (see first row in the table of Figure 1.4) applicable to tunnel analysis.

Terzaghi (1943) solution is an example of a *limit equilibrium* method (see second row in the table of Figure 1.4) applicable to tunnel stability analysis. Indeed, Terzaghi developed one of the first limit equilibrium solutions for the vertical stress acting on the roof of a tunnel in sand. He assumed a simplified model, presented in Figure 1.5, where the yielding soil above the excavation acted as a loading strip that extended upwards from the roof of the excavation to the ground surface. The width of this strip was governed by the geometry of the excavation and the Rankine active state for the walls of the cavity. Terzaghi also assumed that the yielding-soil was bounded by planes on which frictional strength was developed. A few years later this model was further adapted and it became a quite common procedure for engineering design of tunnel supports, particularly in the U.S. (Terzaghi, 1946).

As originally proposed, Caquot (1934) solution (which will be the focus of this thesis work) is an example of a *stress field* method (see third row in the table of Figure 1.4) applicable to tunnel stability analysis. The solution, which is represented in Figure 1.6, allows determination of the minimum internal support pressure required to maintain stability of the shallow tunnel.

Caquot's solution considers that after excavation, stresses around a circular tunnel redistribute around a concentric circular domain with radius that extends from the crown of the tunnel to the ground surface (see Points A and B in Figure 1.6) without developing shear stresses, and

METHOD OF ANALYSIS		SOLUTION REQUIREMENTS				
		Equilibrium	Compatibility	Constituitive behaviour	Boundary conditions	
					Force	Disp
Closed form		S	S	Linear elastic	S	S
Limit equilibrium		S	NS	Rigid with a failure criterion	S	NS
Stress field		S	NS	Rigid with a failure criterion	S	NS
Limit analysis	Lower bound	S	NS	Ideal plasticity with associated flow rule	S	NS
	Upper bound	NS	S		NS	S
Beam-Spring approaches		S	S	Soil modelled by springs or elastic interaction factors	S	S
Full Numerical analysis		S	S	Any	S	S

S - Satisfied; NS - Not Satisfied

Figure 1.4: Methods for performing stability analysis of geotechnical structures (e.g., slopes and foundations) —after Potts & Zdravkovic (1999)

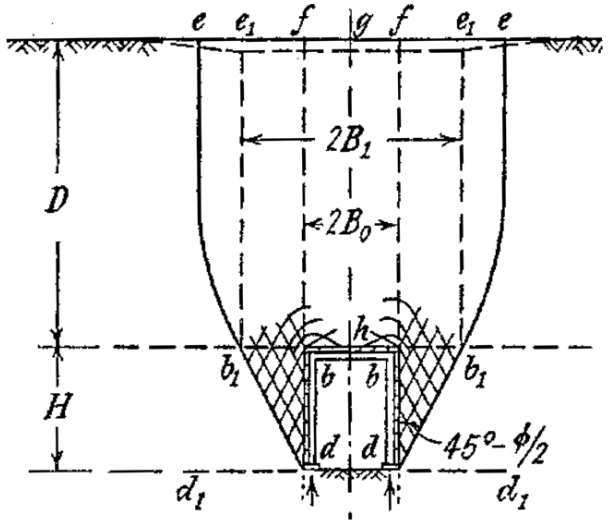

Figure 1.5: Terzaghi's limit equilibrium model (after Terzaghi, 1943)

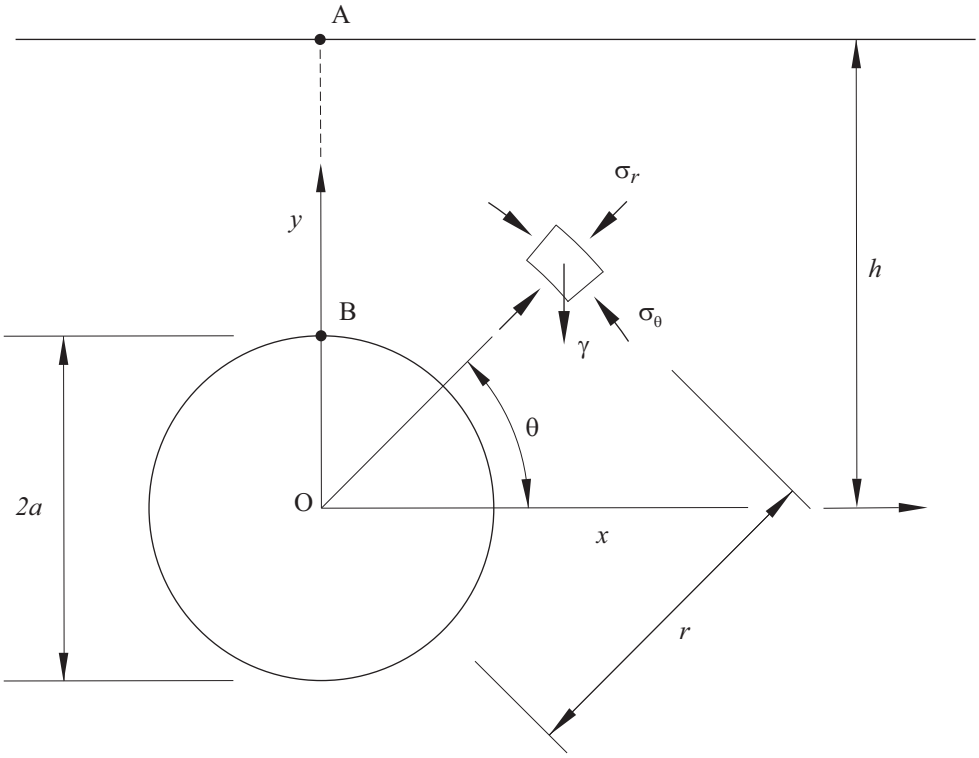

Figure 1.6: Stress field solution proposed by Caquot (1934)

considering that the hoop stresses are major principal stresses and the radial stresses are minor principal stresses. Caquot's solution, as originally proposed, considered that the soil was yielding only along the crown-surface segment A-B in Figure 1.6. Also, as originally proposed, the solution did not verify compatibility of stresses between the inside and outside of the integration domain, so the original solution would have classified as a *stress field* solution (according to the third column of third row in the table of Figure 1.4, solutions that do not satisfy compatibility are classified as *stress field* solutions). [1]

An important method for analysis of stability of geotechnical structures is the one known as *limit analysis* method, which is comprised of lower bound and upper-bound (sub) methods (see fourth row in the table of Figure 1.4). The limit analysis method is based in two theorems of plasticity which are known as the lower bound and the upper bound theorems (Davis & Selvadurai, 2002).

The lower bound theorem states that if a statically admissible solution is found that nowhere violates the plastic constitutive law (i.e., stresses are in equilibrium everywhere and the stress state within the media is either below or at the plastic failure 'envelope' surface, i.e., the material is in elastic or plastic state respectively) then such a statically admissible solution is a lower bound for the support load (in the case of cavities, the internal support pressure) that is required to avoid collapse. In other words, a lower bound (or statically admissible) solution will give a 'safe' estimate of the support load required for the tunnel not to collapse. Note that in the case of slopes, which are normally characterized by *factors of safety*, the lower bound solution will give a *factor of safety* that is lower than the 'actual' one.

The upper bound theorem states that if a kinematically admissible solution is found for

[1] This thesis will investigate Caquot's solution further, and among others, it will show that under certain conditions, there exists compatibility of stresses along the boundary of the integration circle, reason for which, Caquot's solution is actually a *lower bound* solution rather than a *stress field* solution —see fourth row in the table of Figure 1.4.

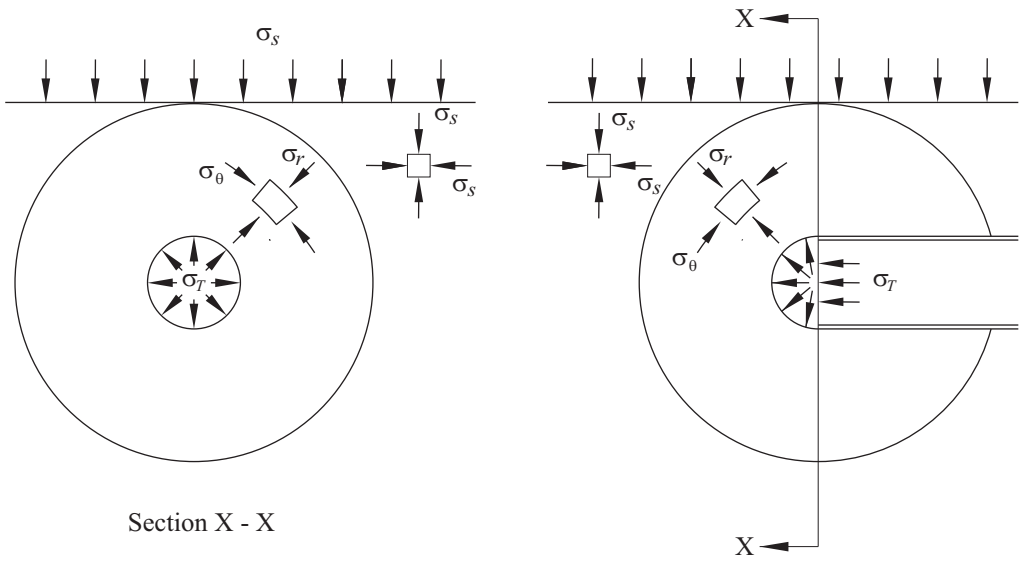

Figure 1.7: Statically admissible plastic solution for a) cylindrical tunnel; and b) front of a tunnel regarded as a spherical cavity (after Davis et al., 1980)

which discrete movement of material is taking place already, then such a kinematically admissible solution is an upper bound for the support load (e.g., internal pressure in a tunnel) that is necessary to avoid collapse. In other words, an upper bound (or kinematically admissible) solution will give an 'unsafe' estimate of the support load required for the tunnel not to collapse. Again, note that in the case of slopes (characterized by factors of safety) the upper bound solution will give a factor of safety that is larger than the 'actual' one.

As an example of limit analysis method, Davis et al. (1980) presented comprehensive applications of the limit theorems, developing models to find the upper and lower bound solutions for two cases of circular tunnels in cohesive material. These two cases were for cylindrical cavity with an unsupported span long enough to consider a plane strain analysis perpendicular to the tunnel heading, and lined tunnels where the unsupported span near the front was short enough to consider a spherical surface with a radius just large enough to encompass the unsupported region. These two cases are presented in Figure 1.7.

1.2.2 Numerical models

Full numerical analyses (see last row in the table of Figure 1.4) are important methods for analysis of stability of geotechnical structures. Potts & Zdravkovic (1999) identify these methods as the most powerful existing methods for performing stability analyses of geotechnical structures. Full numerical methods include the *finite element method* (FEM), *finite difference methods* (FDM), *discrete element methods* (DEM), *boundary element methods* (BEM) and others (Brady & Brown, 2004). A large number of publications exists on this topic. In this section, reference to a quite limited number of these will be made only.

Oden (1990) presents a thorough discussion on the historical development and origins of several numerical methods including the finite element method and finite difference method. Even during the development of the earliest numerical models, it was found that the accuracy of the results increased as the number of elements was increased and the discretization of the mesh became finer. Increasing the model size and level of detail also meant a significant increase in the number of calculations that had to be made to solve a problem. As numerical models involve iterative processes (particularly for non-linear problems, for example, when accounting for plastic materials), the use of these methods was limited prior to the development of powerful computing machinery. Now that there exists powerful computers that can be used affordably, a wide array of complex problems can be solved.

Variations of numerical methods to solve physical and mechanical problems governed by differential equations have been applied to almost every field of engineering. Numerical methods are especially valuable for modeling geotechnical problems because of the discrete behavior of rock and soil conditions due to bedding planes, faults, and joints.

There are two primary ways of treating a numerical geomechanic problem. The medium can be modeled as a discontinuum, where the domain is broken up into a series of blocks or particles that interact with each other discretely, or the medium can be modeled as a continuum, where the domain of elements is discretized to treat discontinuities as internal boundaries.

As one of the many existing publications dealing with stability analysis of shallow tunnels, two will be briefly described next.

Anagnostou & Kovari (1996) evaluated the effects of the ground while performing tunneling with an earth pressure shield. These shields use the freshly excavated soil to apply pressure to the face of the excavation while conveying material away from the tunnel face using a screw conveyor. Their study involved the development of a 3D finite element model that was used to determine the support pressure required for different levels of internal friction in the soil and hydraulic pressure head present in the slurry shield. Their research also investigated the relationship between surcharge loading on the ground surface and the effect it had on tunnel stability.

Vermeer, P.A. et al. (2002) revisited research conducted previously on the subject of stability numbers involving shallow tunnels in soil under the drained condition. In their revisited work, the authors applied the finite element method to model stability of tunnel fronts in ground considered to obey the Mohr-Coulomb plastic failure criterion. In addition to finding the support pressure required to maintain stability in shallow tunnels, the authors explained that this method could be used to predict stress distribution and particularly the resulting displacement field at the critical equilibrium state. As reported in Vermeer, P.A. et al. (2002), Figure 1.8 shows examples of stress distributions and displacements for the case of a 2D (plane strain) section of lined tunnel in the vicinity of the front. Figure 1.8 also shows the effect of reducing the friction angle of the material on the stress distribution and displacements in the neighbourhood of the front. The results from the models with increasing levels of friction demonstrated the effect of arching occurring in the soil above the unsupported face of the tunnel.

1.2.3 Physical models

Physical laboratory methods involve direct observation of behavior of tunnel models in the laboratory and the quantitative and/or qualitative response of these models. Though capable

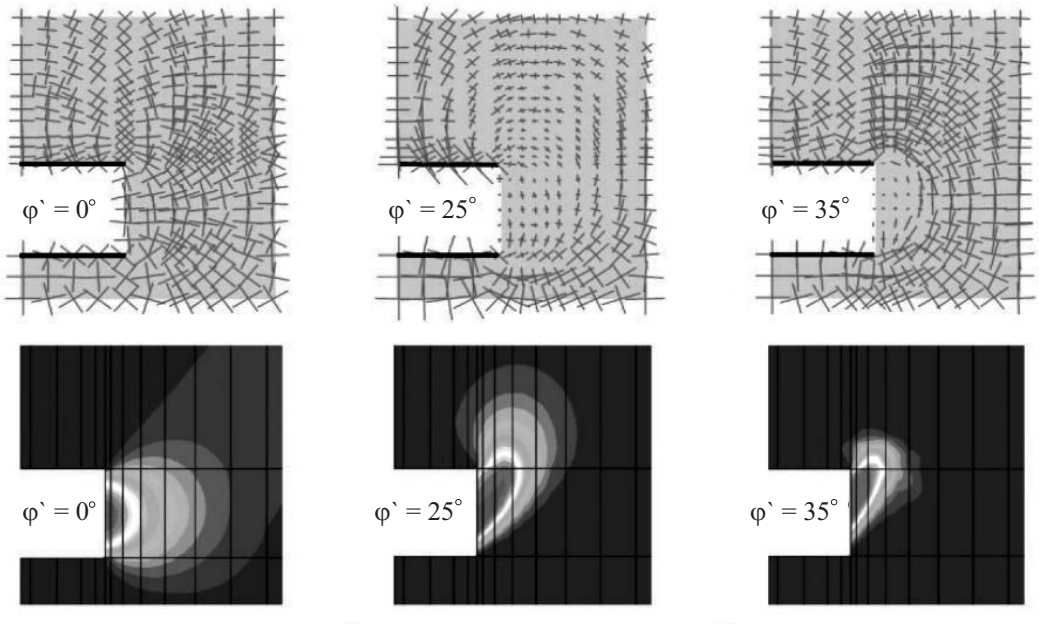

Figure 1.8: Principal stresses and incremental displacements at failure for a tunnel front (after Vermeer, P.A. et al., 2002)

of verifying general behaviors of excavations in soils, these models are not always feasible in determining accurate support requirements of shallow tunnels because soil behavior is highly susceptible to error introduced by scaling the size of the model in the lab to the size of the actual tunnel in the field.

As an example of physical laboratory analysis, the work by Atkinson & Potts (1977) will be briefly discussed, particularly, since it relates to the *limit analysis* methods discussed in Section 1.2.1.

Atkinson & Potts (1977) performed several experiments with physical models of excavations in a sand that had well documented plastic strength properties. They used an impermeable membrane on the interior of the excavation to apply internal support pressure which was reduced at regular intervals until collapse of the tunnel occurred. Photographs were taken at each incremental pressure reduction to document the displacements occurring in the body of soil and

the excavation lining. The theoretical collapse pressures were calculated using the upper and lower bound methods described in Section 1.2.1, for perfectly plastic material. They showed that the experimental results for their tunnel internal pressure at collapse mostly coincided with the upper and lower bound predictions. Error in the experimental results were assumed to be because of the assumed dilation angle of the material. Atkinson & Potts (1977) only experimented with dry sands but went to elaborate on the process of analyzing saturated soils with theoretical upper and lower bound methods.

1.3 Objectives and structure of this thesis

The primary objective of this thesis is to investigate further and to expand upon Caquot's model (Figure 1.6) as a tool for analysis of stability of shallow tunnels. Caquot's model will be further developed to account for various improvements as described below.

It is standard practice in geotechnical engineering to assess the stability of soil slopes (including embankments and levees) by applying the *strength reduction technique* (or SRT) (Dawnson et al., 1999) and determining a scalar *factor of safety* (or FS) for the structure (Abramson, L.W. et al., 2002). Assessment of stability conditions of shallow tunnels in terms of factors of safety has been rarely been done in the past. Taking as a precedent two existing publications (Carranza-Torres, 2004; Carranza-Torres, Reich, & Saftner, 2013) that proposes the use of factor of safety for shallow tunnels, one of the objectives of this thesis work is to reformulate Caquot's solution for cases of dry and saturated ground to express the stability conditions in terms of a factor of safety.

For the sake of space and with the purpose of limiting the scope of this thesis work, the plastic material model to be considered for the ground in Caquot's extended model will be the Tresca plastic model. The Tresca model, which is represented in the 3D space of principal stresses in Figure 1.9, is a particular case of the Mohr-Coulomb plastic model for which the

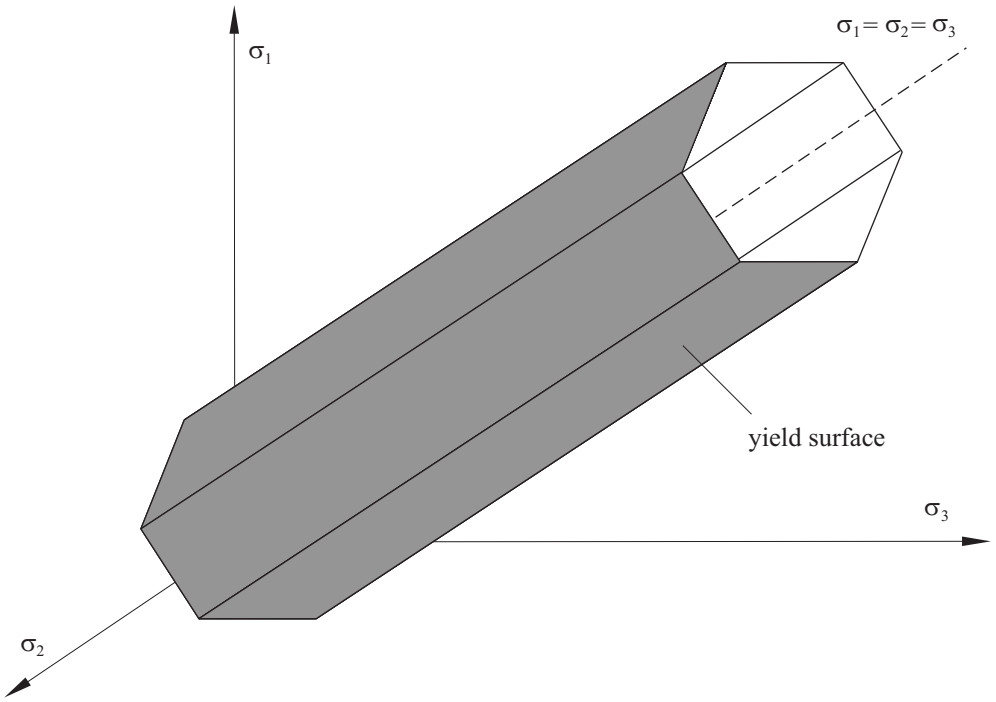

Figure 1.9: Tresca failure envelope represented in the 3D space of principal stresses

material is assumed to have cohesion only (i.e., an angle of internal friction equal to zero).

The structure of this thesis is as follows.

Chapter 2 discusses the simplest version of the extended Caquot's model corresponding to a cylindrical or spherical cavity excavated in dry ground, and considering that a surcharge load exists on the ground surface. Scaling rules for the variables involved are introduced together with the expressions that define the stress field around the cavity, and the factor of safety of the model. The influence of the several factors and variables involved in the solution on the resulting factor of safety, such as whether the cavity is assumed to be cylindrical or spherical, the scaled depth of the cavity, the scaled internal pressure and the scaled surcharge load on the ground, are investigated. Appendix A provides the derivation of equations presented in Chapter 2. Appendix A also shows that the extended Caquot's solution is a statically admissible solution,

i.e., that there exists continuity of stresses at the boundary between redistributed stresses and original in-situ stresses (see footnote in page 9, Section 1.2.1).

Chapter 3 considers the extended Caquot's model (for cylindrical and spherical cavities) in the case in which there exists water in the ground. Two situations are considered for the derivation of factor of safety equations with regard to the elevation of the water surface, namely the case in which the water surface is above the ground surface, and the case in which the water surface is below the ground surface. Also, for both cases mentioned above, the cavity is considered to be 'dry' (with only a mechanical pressure acting inside the cavity), or to be 'flooded' (with both mechanical and hydrostatic pressure acting inside the cavity). The influence of the different variables involved in the solution on the resulting factor of safety is investigated, including also a comparison of resulting factors of safety for the cases of saturated ground and dry ground, and cases of 'dry' cavity and 'flooded' cavities. Appendix B provides a derivation of the equations presented in Chapter 3.

Considering that analytical models developed in Chapters 2 and 3 are static admissible models (and therefore give lower bound results of stability conditions), the values of factors of safety predicted with these models are only conservative approximations of the 'true' values of factor of safety for the cavities. Also considering that numerical finite element or finite difference models for which the size of elements in the mesh is fine enough will give factors of safety values that are close to the 'true' ones (this is in view that that numerical solutions satisfy all governing equations for the problems at hand, see last row in Figure 1.4), a comparison between analytical and numerical results seems justified. Chapter 4 presents a comparison of factor of safety results obtained with both the extended Caquot's solution for dry ground and with the commercial finite difference software FLAC®, implementing the strength reduction technique. Chapter 4 also quantifies the differences between analytical and numerical results and discusses the influence of variables involved in the solution of the numerical models, such as configuration of assumed internal pressure and mesh size.

Finally, Chapter 5 summarizes the conclusions of this research work.

Chapter 2

Caquot's solution for dry ground

2.1 Problem statement

The extended Caquot's model of a shallow circular cavity to be investigated is presented in Figure 2.1. The ground is assumed to be dry, to have a unit weight, γ, and to obey a Tresca failure criterion with cohesion, c.

The circular cavity has a radius, a, with its center located at a depth, h, from the ground surface (as shown in Figure 2.1, the origin of a cartesian system x-y is assumed to be at the center of the cavity). The circular cavity shown in Figure 2.1 is considered to represent either a plane-strain section of cylindrical tunnel or a axi-symmetric spherical cavity.

The cavity is assumed to be subjected to an internal support pressure distribution as indicated in Figure 2.1. The pressure at the crown of the cavity (point A) is denoted as p_s^A, the pressure at the spring line of the cavity (point C) is denoted as p_s^C, and the pressure at the invert of the cavity (point D) is denoted as p_s^D. The way in which the pressure varies in between these locations will be discussed later on.

A uniform surcharge load, q_s, is assumed to act on the ground surface. This surcharge load represents, for example, the load transfer to the ground from a temporary embankment.

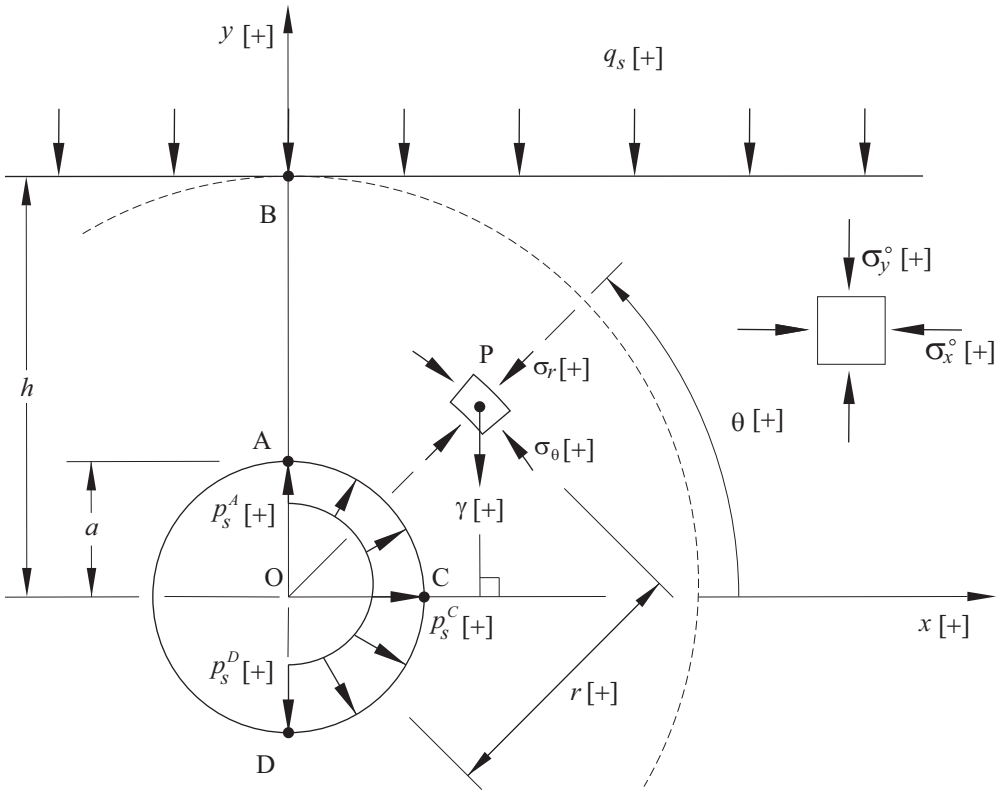

Figure 2.1: Extended Caquot model considered in this research as applied to the analysis of stability of shallow circular cavities in plastic material

A circular area concentric with the center of the cavity and tangent to the ground surface (at point B in Figure 2.1), and therefore having a radius h, is referred to as the *integration circle*. The point P shown in Figure 2.1 represents an arbitrary point projected from the origin with cylindrical coordinates (r and θ), that falls inside the integration circle. The stress state at point P is represented by a radial stress, σ_r, and a tangential (or hoop) stress, σ_θ. Note that as in the case of the original Caquot's model, shear stresses are neglected, and σ_r and σ_θ are assumed to be minor and major principal stresses, respectively (see Section 1.2.1).

Before excavation, the stress state in the ground is defined by lithostatic vertical and horizontal stresses, σ_y^o and σ_x^o, respectively. These stresses are defined in terms of the variables

introduced above as

$$\sigma_y^o = q_s + \gamma(h - y) \tag{2.1}$$

and

$$\sigma_x^o = K_o \, \sigma_y^o \tag{2.2}$$

In Equation 2.2, K_o is the lateral earth pressure coefficient.

After excavation, the stress state given by Equations 2.1 and 2.2 still applies to the ground outside the integration circle (see Figure 2.1).

Figure 2.2 represents the Tresca yield envelope in the 2D space of principal stresses, σ_1 and σ_3. The point of intersection between the failure envelope and the vertical axis is the unconfined compressive strength, σ_c.

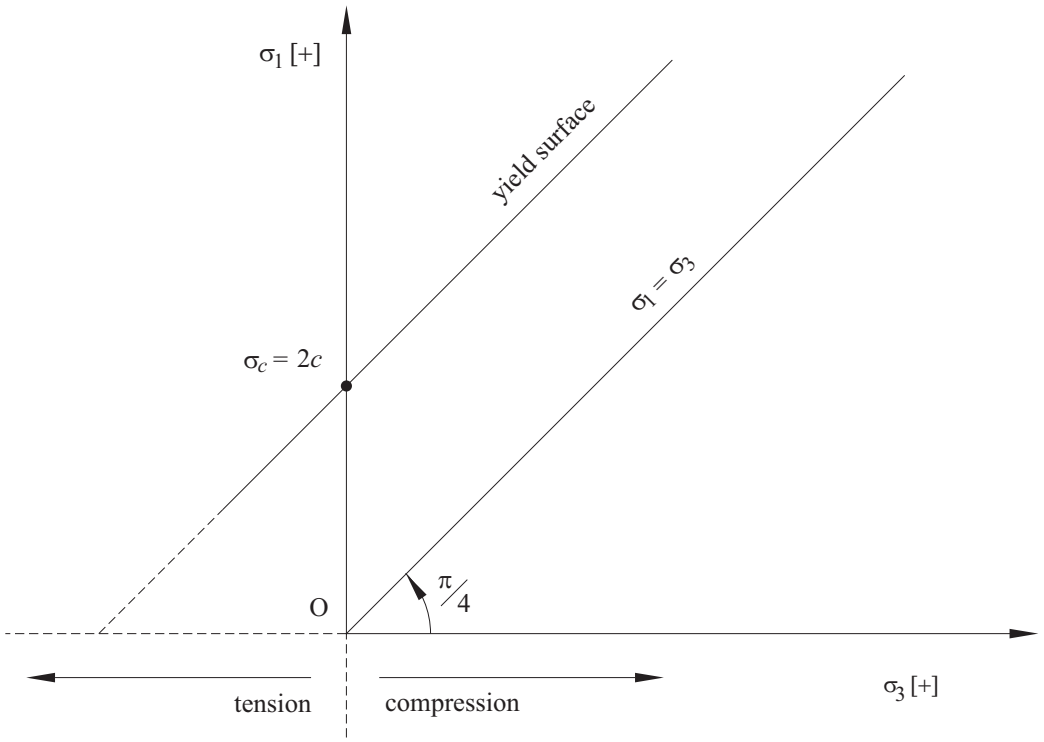

Figure 2.2: Tresca failure envelope represented in the 2D space of principal stresses

The Tresca failure criterion represented in Figure 2.2 is written as follows

$$\sigma_1 = \sigma_3 + \sigma_c \tag{2.3}$$

The Tresca failure envelope can also be expressed in terms of normal and shear stresses on the failure plane, σ_n and τ_s, respectively, as shown in Figure 2.3.

In the representation of Figure 2.3, the intercept of the failure envelope and the vertical axis is the cohesion, c. The (Mohr) circle represented in Figure 2.3 corresponds to the principal stress state at failure without confinement. Figure 2.3 shows that the unconfined compressive strength, σ_c, must be equal to two times the cohesion, c, i.e.,

$$\sigma_c = 2\,c \tag{2.4}$$

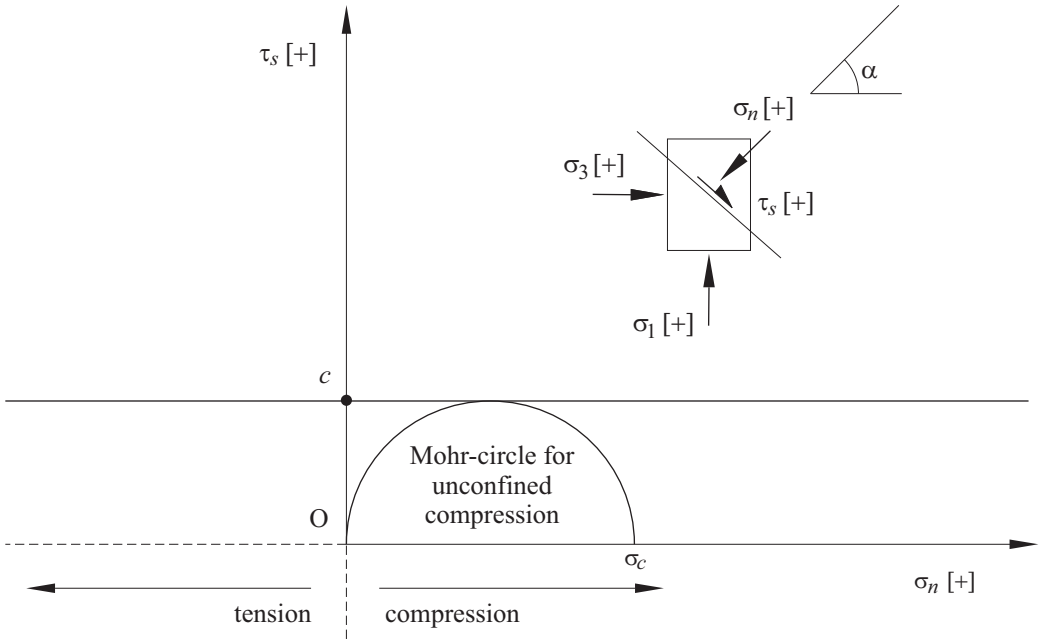

Figure 2.3: Tresca failure envelope represented in the 2D space of shear and normal stresses

Figure 2.3 also shows that for the Tresca failure criterion, where the failure envelope is parallel to the horizontal axis, there is no intercept between failure envelope and horizontal axis

and therefore the 'natural' tensile strength predicted by the Tresca failure criterion is infinite. Although this observation is not relevant for the case of cavities in dry ground addressed in this chapter, the tensile strength of the material plays a role in the case of cavities in saturated ground, as it will be discussed in the next chapter.

2.2 Scaled form of Caquot's solution

In order to present the solution of the problem introduced in the previous section in a concise and neat manner, input variables for the model are scaled with respect to key cavity geometry and ground strength parameters.

The ratio of the radial distance from the cavity center, r, and the radius of the cavity, a, defines the scaled radial distance, ρ, as follows

$$\rho = \frac{r}{a} \tag{2.5}$$

The scaled radial distance corresponding to scaled radius of the integration circle, and therefore the scaled depth of the cavity, is denoted as ξ,

$$\xi = \frac{h}{a} \tag{2.6}$$

Stress quantities are scaled by dividing them by the unit weight of the soil, γ, and the radius of the cavity, a. These scaled stresses are denoted using a 'tilde' above their symbols. Therefore

$$\tilde{q}_s = \frac{q_s}{\gamma a}; \qquad \tilde{p}_s = \frac{p_s}{\gamma a} \tag{2.7}$$

and

$$\tilde{\sigma}_r = \frac{\sigma_r}{\gamma a}; \qquad \tilde{\sigma}_\theta = \frac{\sigma_\theta}{\gamma a} \tag{2.8}$$

The cohesion, c, of the ground is similarly scaled as follows

$$\tilde{c} = \frac{c}{\gamma a} \tag{2.9}$$

When expressed in terms of the scaled quantities introduced above, Caquot's solution for the scaled radial stress, $\tilde{\sigma}_r$, and for the scaled tangential stress, $\tilde{\sigma}_\theta$, in the integration circle results (Appendix A provides the derivation of the equations below)

$$\tilde{\sigma}_r(\rho,\theta) = \tilde{\sigma}_r^{AB}(\rho) + \rho(1-\sin\theta) \tag{2.10}$$

and

$$\tilde{\sigma}_\theta(\rho,\theta) = \tilde{\sigma}_\theta^{AB}(\rho) + \rho(1-\sin\theta) \tag{2.11}$$

where the stresses $\tilde{\sigma}_r^{AB}(\rho)$ and $\tilde{\sigma}_\theta^{AB}(\rho)$ represent the distribution of radial and hoop stresses on the crown-surface segment A-B represented in Figure 2.1. These stresses are

$$\tilde{\sigma}_r^{AB}(\rho) = \tilde{q}_s + \xi - \rho + 2\tilde{c}k\ln\frac{\rho}{\xi} \tag{2.12}$$

and

$$\tilde{\sigma}_\theta^{AB}(\rho) = \tilde{\sigma}_r^{AB}(\rho) + 2\tilde{c} \tag{2.13}$$

As noted before, these equations are valid for both cases of cylindrical cavities, when $k = 1$, and for spherical cavities, when $k = 2$.

Considering that the solution given by Equations 2.10 through 2.13 is valid when the cavity is at the verge of collapse, and considering that the scaled internal pressure at the crown of the cavity, $\tilde{p}_s^A$, (at point A in Figure 2.1) must be equal to the scaled radial stress defined by Equations and 2.10 and 2.12, when $\rho = 1$ and $\theta = \pi/2$, the critical scaled internal pressure at the crown needed to maintain equilibrium results

$$\tilde{p}_s^A = \tilde{q}_s + \xi - 1 - 2\tilde{c}k\ln\xi \tag{2.14}$$

The solution for the scaled internal pressure at the crown of the cavity given by Equation 2.14 is a particular case of a more general equation that defines the distribution of the scaled internal pressure on the periphery of the cavity, which can be obtained by considering $\rho = 1$ in Equation 2.10. This gives

$$\tilde{p}_s(\theta) = \tilde{p}_s^A + 1 - \sin\theta \tag{2.15}$$

The internal pressures at the spring line and invert of the cavity (at points C and D, respectively, in Figure 2.1) can be found considering the values $\theta = 0$ and $\theta = -\pi/2$, respectively, in Equation 2.15. This gives

$$\tilde{p}_s^C = \tilde{p}_s^A + 1 \tag{2.16}$$

and

$$\tilde{p}_s^D = \tilde{p}_s^A + 2 \tag{2.17}$$

Comparison of Equation 2.14 with Equations 2.16 and 2.17 indicates that the distribution of internal pressure inside the cavity in Caquot's solution is not uniform, but varies hydrostatically with depth, as if provided by an imaginary fluid that has the same unit weight as the material surrounding the cavity. The effect of considering a different type of internal pressure distribution in Caquot's model will be investigated further in Chapter 4.

2.3 Computation of factor of safety for Caquot's solution

According to the standard definition of factor of safety, for a Tresca material, the factor of safety, *FS*, can be defined as the ratio of *existing* cohesion, c, and *critical* cohesion, c_{cr}, that causes the cavity to collapse. Considering scaled values of cohesion, the definition becomes

$$FS = \frac{\tilde{c}}{\tilde{c}_{cr}} \tag{2.18}$$

or

$$\tilde{c}_{cr} = \frac{\tilde{c}}{FS} \tag{2.19}$$

As mentioned already in the previous section, the solution for the scaled internal pressure at the crown of the cavity given by Equation 2.14 is valid when the cavity is at the verge of equilibrium (in the critical situation in which it is about to collapse). Therefore, replacing the variable $\tilde{c}$ in Equation 2.14 by the variable $\tilde{c}_{cr}$, while considering the definition of $\tilde{c}_{cr}$ given by

Equation 2.19, and solving for the variable FS in the resulting equation, the factor of safety for the cavity results

$$FS = \frac{2\tilde{c}\,k \ln \xi}{\tilde{q}_s - \tilde{p}_s + \xi - 1} \tag{2.20}$$

In Equation 2.20, the scaled cohesion, $\tilde{c}$, is the given scaled cohesion for the ground (see Equation 2.9). Also, in Equation 2.20, the scaled pressure, $\tilde{p}_s$, is the pressure at the crown of the cavity (for simplicity in the notation, the superscript 'A', as in Equation 2.14, has been dropped).

2.4 Influence of input parameters on factor of safety

The explicit solution for factor of safety given by Equation 2.20 provides a means to investigate the influence of involved parameters on the resulting factor of safety for the problem of stability of a shallow cavity. The objective of this section is to present this investigation and to remark on significant observations in the results.

The first relevant observation made for the factor of safety predicted by Equation 2.20 is that since the parameter k acts as a multiplier in the numerator of Equation 2.20, the value of factor of safety for a spherical cavity (considering $k = 2$ in Equation 2.20) will always be two times the value of factor of safety for a cylindrical cavity (considering $k = 1$ in Equation 2.20), certainly, with all other input parameters being the same.

With this first observation in mind, the following subsections investigate the influence of other parameters involved in Equation 2.20 on the resulting factor of safety, namely, the scaled depth of the cavity, ξ, the scaled internal pressure at the crown, $\tilde{p}_s$, and the scaled ground surcharge load, $\tilde{q}_s$.

2.4.1 Influence of cavity depth

Figure 2.4 represents the relationship between factor of safety, FS, (vertical axis) and scaled cohesion, $\tilde{c}$, (horizontal axis) as a function of scaled depth, ξ, for cylindrical cavities, as given

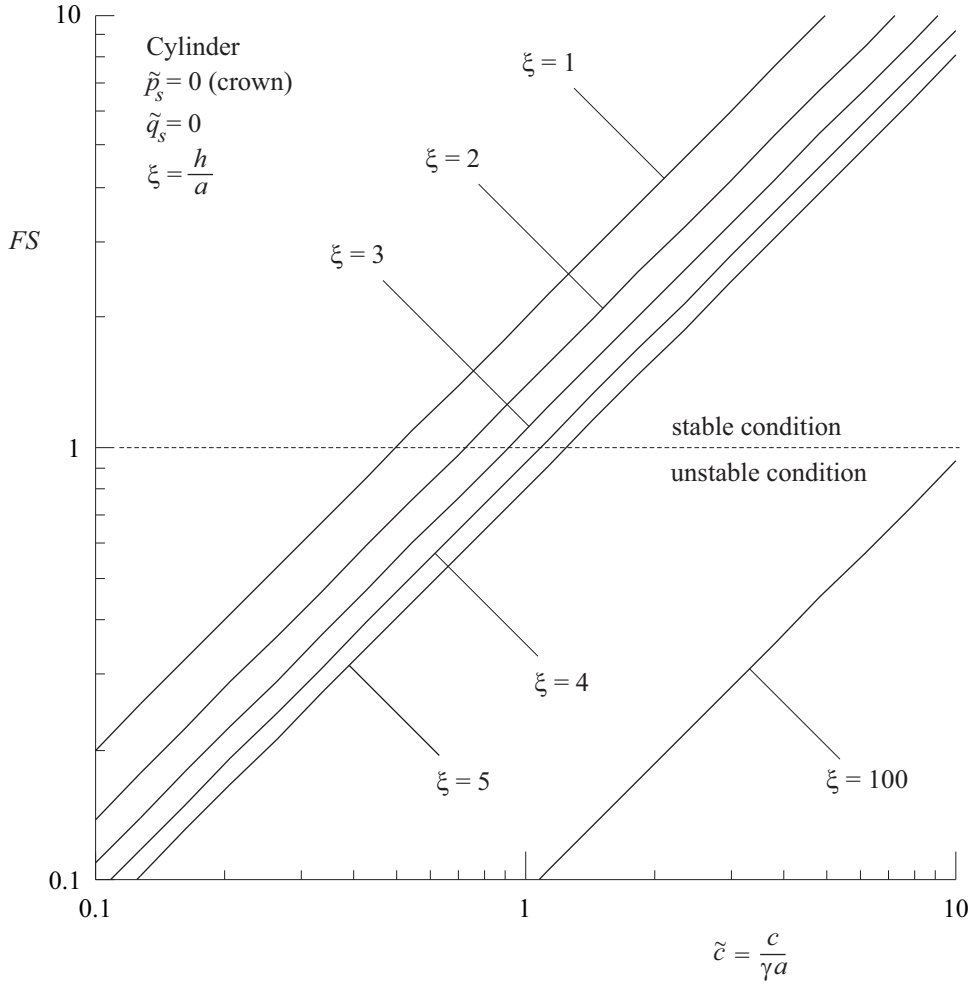

Figure 2.4: Relationship between factor of safety and scaled cohesion as a function of scaled depth for cylindrical cavities

by Equation 2.20. Cases of cylindrical cavities at ξ equal to 1, 2, 3, 4, 5 and 100 (the last value taken as as an arbitrary large value to inspect the trend of results) are represented in the figure as different parallel lines (note that in a logarithmic representation as in Figure 2.4, the relationship between FS and $\tilde{c}$ for constant ξ is linear). Figure 2.4 considers that the surcharge load on the ground and the internal pressure at the crown of the cavity are both zero ($\tilde{q}_s = 0$ and $\tilde{p}_s = 0$,

respectively). The line $\xi = 1$ corresponds to the theoretical minimum depth for the cavity. The factor of safety obtained for such case is a maximum, and can be obtained by taking the limit when ξ tends to 1 in Equation 2.20, to give

$$FS = 2\tilde{c}k \tag{2.21}$$

Figure 2.4 shows that as the scaled cohesion of the ground increases (when moving to the right on the horizontal axis), the factor of safety increases. Also, as the scaled depth of the cavity increases (ξ increases) the factor of safety decreases. This somehow counterintuitive observation can be explained by considering that as the cavity depth increases, the magnitude of loading around the cavity increases, and therefore the 'ease' for a plastic zone to develop and extend to the ground surface to produce instability also increases.

For completeness, Figure 2.5 presents a similar representation as that in Figure 2.4 but for the case of spherical cavity. As already mentioned, the predicted values of factor of safety for spherical cavities are twice the predicted values of factor of safety for cylindrical cavity.

To obtain a unique dimensionless representation for how the factor of safety decreases with scaled cavity depth, valid for both cylindrical and spherical cavities (and for the case $\tilde{q}_s = 0$ and $\tilde{p}_s = 0$), the ratio f_{FS}^{ξ} is introduced

$$f_{FS}^{\xi} = \frac{FS(\xi)}{FS(1)} \tag{2.22}$$

In Equation 2.22, $FS(\xi)$ is the factor of safety for an arbitrary value of ξ (given by Equation 2.20), while $FS(1)$ is the maximum theoretical factor of safety for the theoretical shallowest cavity (see Equation 2.21).

Figure 2.6 represents the variation of the ratio f_{FS}^{ξ} (vertical axis) with the scaled depth ξ (horizontal axis). As expected, the ratio f_{FS}^{ξ} is one when $\xi = 1$ and tends to zero as ξ tends to infinity.

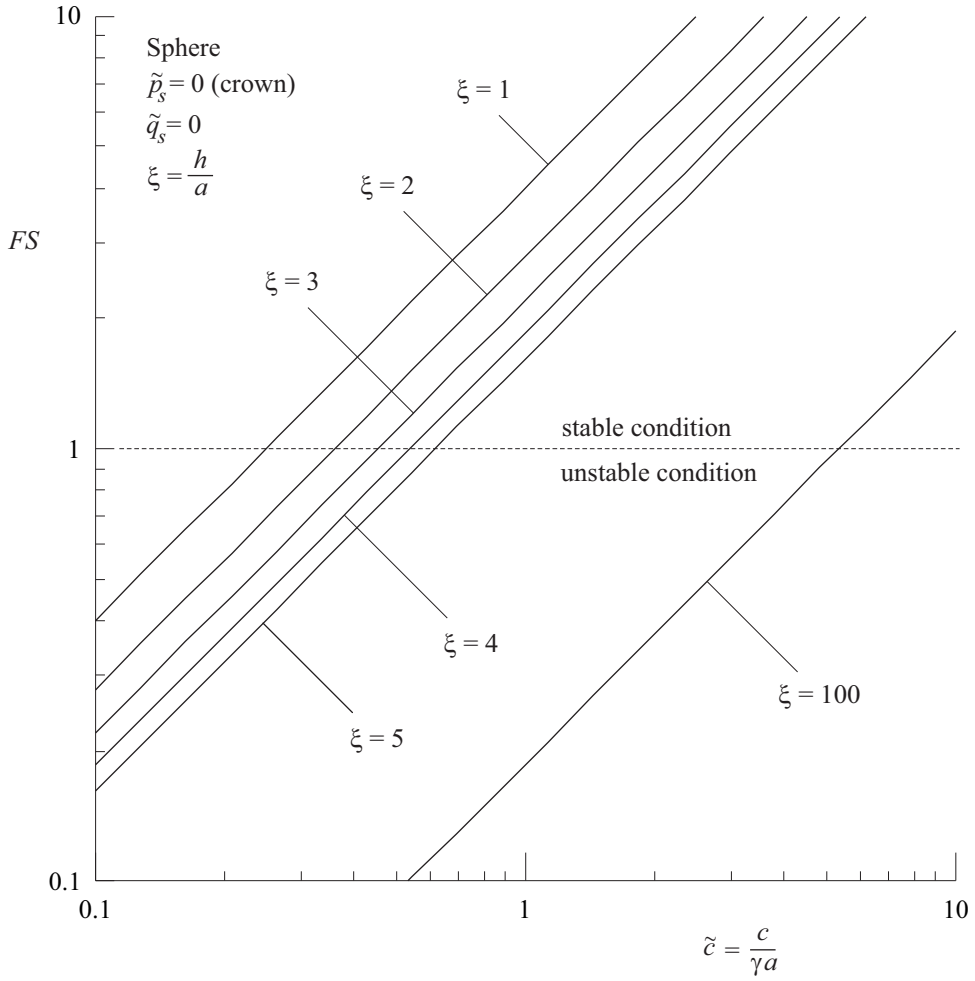

Figure 2.5: Relationship between factor of safety and scaled cohesion as a function of scaled depth for spherical cavities

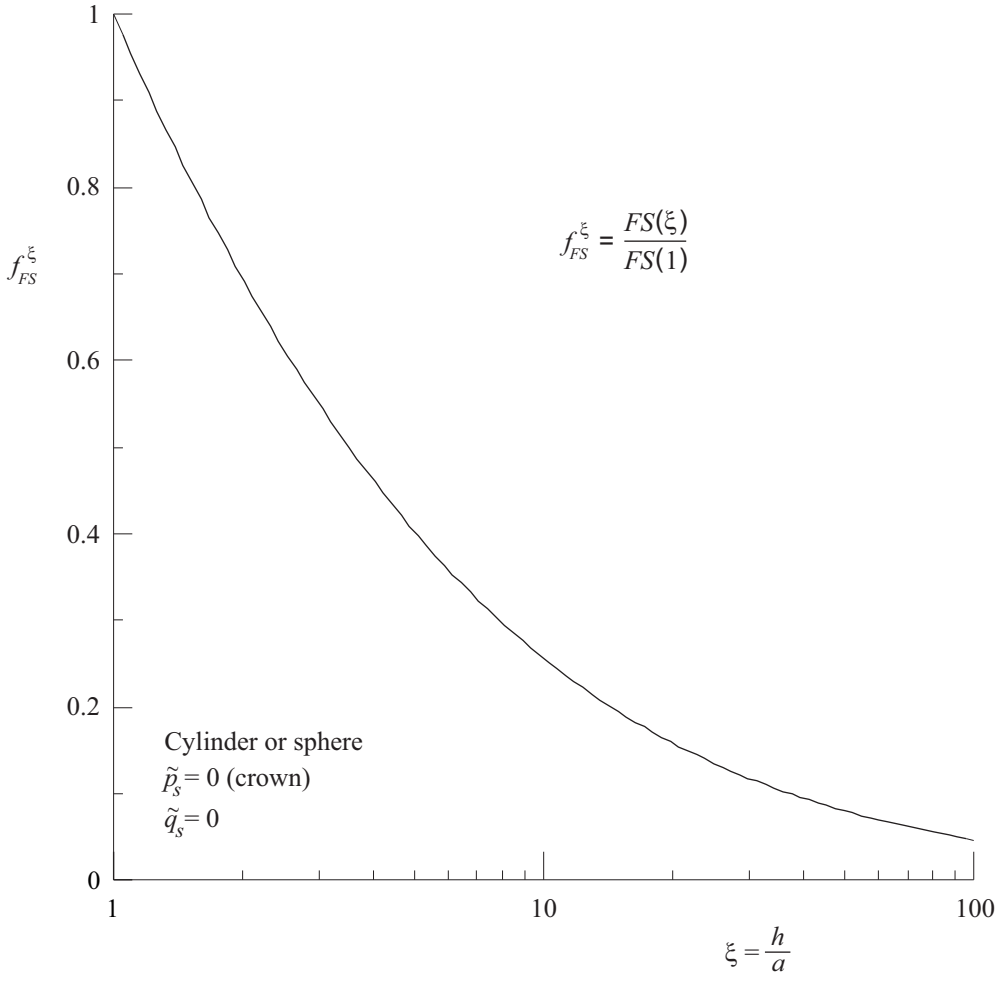

Figure 2.6: Relationship between scaled factor of safety and scaled cavity depth for cylindrical and spherical cavities

2.4.2 Influence of internal pressure

First, it is noted that for a 'contracting' cavity the maximum possible internal pressure at the crown of the cavity corresponds to the pressure associated with the in-situ stresses prior to excavation (see Equation 2.1). Considering scaled geometrical and stress quantities (as defined by Equations 2.6 through 2.9), the maximum internal pressure at the crown of the cavity, $\tilde{p}_s^o$, is obtained from Equation 2.1 and results

$$\tilde{p}_s^o = \tilde{q}_s + \xi - 1 \tag{2.23}$$

For a given scaled depth of cavity, ξ, the factor of safety will become infinite, if the pressure at the cavity crown is taken to be equal to $\tilde{p}_s^o$ (this can be confirmed by replacing Equation 2.23 into Equation 2.20, in such case the denominator of Equation 2.20 becomes zero). For decreasing values of scaled pressure at the cavity crown (for values of $\tilde{p}_s$ less than $\tilde{p}_s^o$), the factor of safety will decrease.

Next, a ratio, $f_{\tilde{p}s}$, of arbitrarily scaled (crown) pressure, $\tilde{p}_s$, and maximum scaled (crown) pressure, $\tilde{p}_s^o$, is introduced

$$f_{\tilde{p}s} = \frac{\tilde{p}_s}{\tilde{p}_s^o} \tag{2.24}$$

Note that the ratio $f_{\tilde{p}s}$ is equal to zero if no (crown) cavity pressure is considered, and equal to one if the (crown) cavity pressure is considered to be the one associated with the in-situ stresses.

Figure 2.7 represents the relationship between factor of safety, *FS*, (vertical axis) and scaled cohesion, $\tilde{c}$, (horizontal axis) as a function of the cavity crown pressure expressed in terms of the ratio $f_{\tilde{p}s}$ introduced above for a cylindrical cavity at a scaled depth $\xi = 2.5$, with zero ground surcharge load ($\tilde{q}_s = 0$). Cases of scaled crown pressure, $f_{\tilde{p}s}$, equal to 0 (no internal pressure), 0.25, 0.5, 0.75, and 0.95 (the last value taken as as an arbitrary large value less than one to inspect the trend of results) are presented as different parallel lines in Figure 2.7. Figure 2.7 shows again that as the cohesion of the ground increases (when moving to the right on the horizontal axis), the factor of safety increases. Also, as the scaled cavity crown pressure

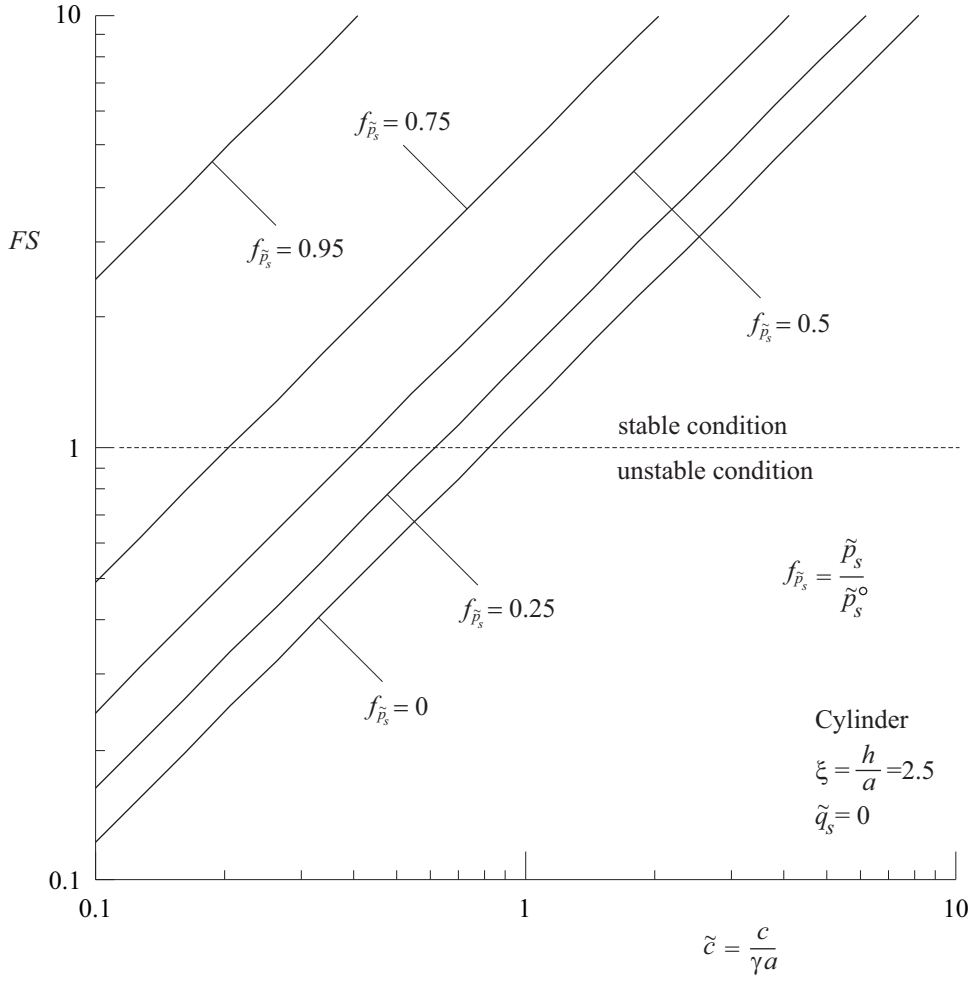

Figure 2.7: Relationship between factor of safety and scaled cohesion as a function of scaled internal pressure for cylindrical cavities

increases ($f_{\tilde{p}s}$ increases from the minimum value zero) the factor of safety increases.

To obtain a dimensionless representation of how the factor of safety increases with increased cavity crown pressure, that is valid for both cylindrical and spherical cavities, and for any scaled depth, ξ, and surcharge load, $\tilde{q}_s$, the ratio $f_{FS}^{\tilde{p}s}$ is introduced

$$f_{FS}^{\tilde{p}s} = \frac{FS(\tilde{p}_s)}{FS(0)} \tag{2.25}$$

In Equation 2.25, $FS(\tilde{p}_s)$ is the factor of safety for an arbitrary value of $\tilde{p}_s$, expressed in terms of the ratio $f_{\tilde{p}s}$ introduced in Equation 2.24. Replacing $\tilde{p}_s$ in Equation 2.20, with the value of $\tilde{p}_s$ in Equation 2.24, and replacing also the value $\tilde{p}_s^o$ in Equation 2.24 with the value of $\tilde{p}_s^o$ given by Equation 2.23, the numerator in Equation 2.25 results

$$FS(\tilde{p}_s) = \frac{2\tilde{c}k\ln\xi}{(1-f_{\tilde{p}s})(\xi+\tilde{q}_s-1)} \tag{2.26}$$

In Equation 2.25, $FS(0)$ is the factor of safety for zero cavity crown pressure, also expressed in terms of the ratio $f_{\tilde{p}s}$ introduced in Equation 2.24. Therefore, making similar replacements as described above for the denominator of Equation 2.25, $FS(0)$ results in

$$FS(0) = \frac{2\tilde{c}k\ln\xi}{\xi+\tilde{q}_s-1} \tag{2.27}$$

Replacing Equations 2.26 and 2.27 into Equation 2.25, the ratio $f_{FS}^{\tilde{p}s}$ becomes

$$f_{FS}^{\tilde{p}s} = \frac{1}{1-f_{\tilde{p}s}} \tag{2.28}$$

Equation 2.28 clearly shows that the ratio $f_{FS}^{\tilde{p}s}$, as defined by Equation 2.25, depends only on the variable $f_{\tilde{p}s}$ and therefore is valid for both cylindrical and spherical cavities, for any considered scaled depth, ξ, and surcharge load, $\tilde{q}_s$.

Figure 2.8 represents the variation of the ratio $f_{FS}^{\tilde{p}s}$ (vertical axis) with the ratio $f_{\tilde{p}s}$ (horizontal axis). As expected, the ratio $f_{FS}^{\tilde{p}s}$ is one when $f_{\tilde{p}s} = 0$ and tends to infinity as $f_{\tilde{p}s}$ tends to one.

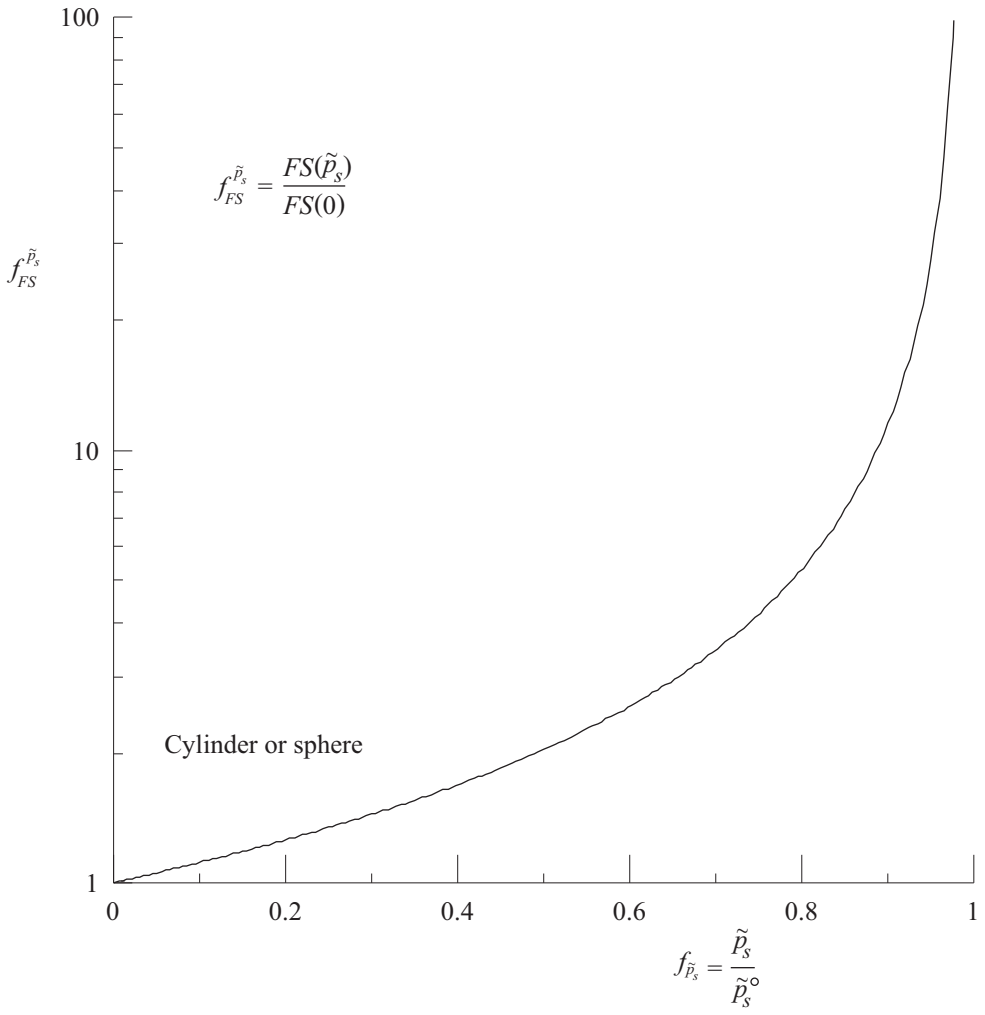

Figure 2.8: Relationship between scaled factor of safety and scaled internal pressure for cylindrical and spherical cavities

2.4.3 Influence of ground surcharge load

To investigate the influence of the ground surcharge load, an analysis similar to the one done for the influence of the cavity crown pressure in Section 2.4.2 is presented below.

First, for a cavity located at a scaled depth, ξ, a *reference* scaled ground surcharge load, $\tilde{q}_s^R$, is introduced. This reference ground surcharge load is (arbitrarily) taken to be equal to the scaled lithostatic pressure associated with the weight of the overburden ground above the crown of the cavity. In this way, the unscaled reference surcharge load is computed as $\gamma(h-a)$, and the scaled reference surcharge load becomes

$$\tilde{q}_s^R = \xi - 1 \tag{2.29}$$

Next, a ratio, $f_{\tilde{q}s}$, of arbitrary scaled ground surcharge load, $\tilde{q}_s$, and scaled reference surcharge load, $\tilde{q}_s^R$, is introduced

$$f_{\tilde{q}s} = \frac{\tilde{q}_s}{\tilde{q}_s^R} \tag{2.30}$$

Note that the ratio $f_{\tilde{q}s}$ is equal to zero if no ground surcharge load is considered, and equal to one if the scaled ground surcharge load is equal to the scaled reference surcharge load.

Figure 2.9 represents the relationship between factor of safety, *FS*, (vertical axis) and scaled cohesion, $\tilde{c}$, (horizontal axis) as a function of the ground surcharge load expressed in terms of the ratio $f_{\tilde{q}s}$ introduced above for a cylindrical cavity at a scaled depth $\xi = 2.5$, and zero cavity crown pressure ($\tilde{p}_s = 0$). Cases of ground surcharge load, $f_{\tilde{q}s}$, equal to 0 (no surcharge load), 0.5, 1, 2, 3, and 10 (the last value taken as as an arbitrary large value to inspect the trend of results) are presented in Figure 2.9 as different parallel lines. Figure 2.9 shows again that as the cohesion of the ground increases (when moving to the right on the horizontal axis), the factor of safety increases. Also, as the ground surcharge load increases ($f_{\tilde{q}s}$ increases from the minimum value zero) the factor of safety decreases.

To obtain a dimensionless representation of how the factor of safety decreases with increased ground surcharge load, valid for both cylindrical and spherical cavities (with zero scaled

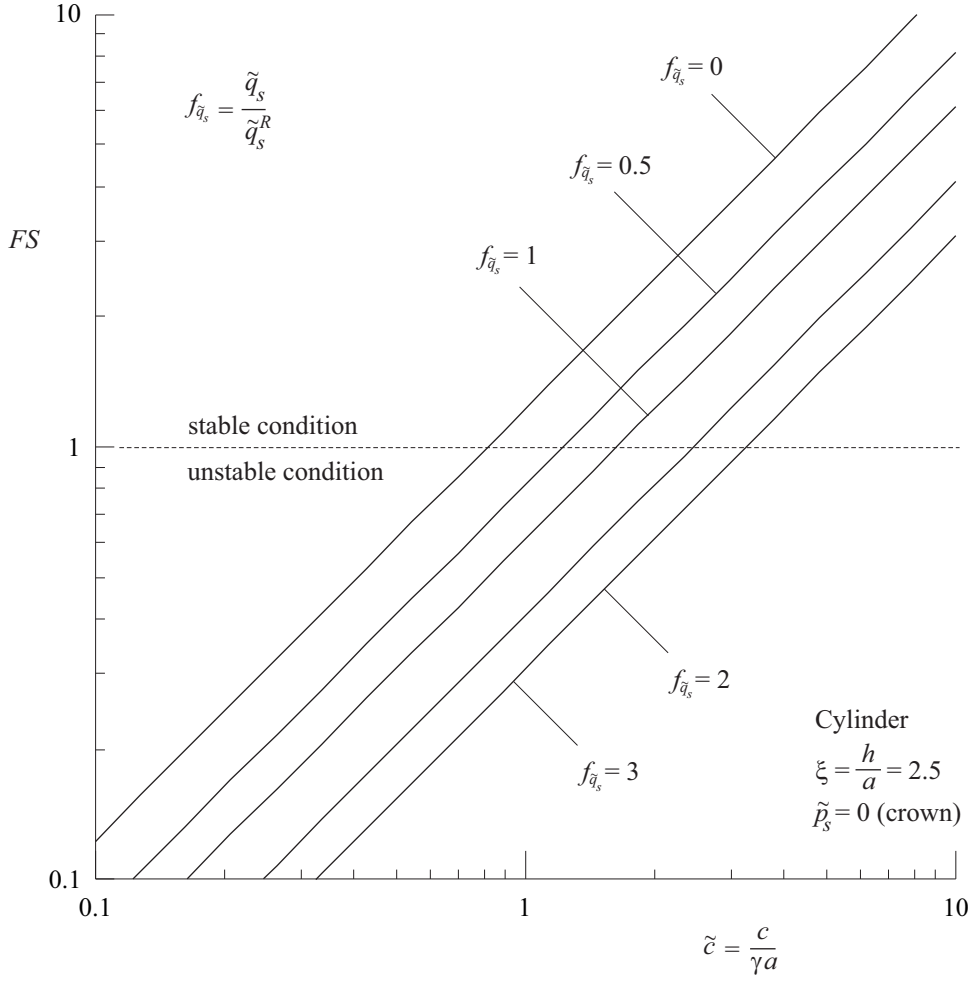

Figure 2.9: Relationship between factor of safety and scaled cohesion as a function of scaled ground surcharge load for cylindrical cavities

cavity crown pressure, $\tilde{p}_s = 0$) and for any scaled depth, ξ, the ratio $f_{FS}^{\tilde{q}s}$ is introduced

$$f_{FS}^{\tilde{q}s} = \frac{FS(\tilde{q}_s)}{FS(\tilde{q}_s^R)} \tag{2.31}$$

In Equation 2.31, $FS(\tilde{q}_s)$ is the factor of safety for an arbitrary value of $\tilde{q}_s$, expressed in terms of the ratio $f_{\tilde{q}s}$ introduced in Equation 2.30. Replacing $\tilde{q}_s$ in Equation 2.20, with the value of $\tilde{q}_s$ in Equation 2.30, and replacing also the value $\tilde{q}_s^R$ in Equation 2.30 with the value of $\tilde{q}_s^R$ given

by Equation 2.29, the numerator in Equation 2.31 results

$$FS(\tilde{q}_s) = \frac{2\tilde{c}k\ln\xi}{(1+f_{\tilde{q}s})(\xi-1)} \tag{2.32}$$

In Equation 2.31, $FS(\tilde{q}_s^R)$ is the factor of safety for ground surcharge load equal to the reference ground surcharge load, also expressed in terms of the ratio $f_{\tilde{q}s}$ introduced in Equation 2.31. Therefore, making similar replacements as described above for the denominator of Equation 2.31, $FS(\tilde{q}_s^R)$ results

$$FS(\tilde{q}_s^R) = \frac{\tilde{c}k\ln\xi}{\xi-1} \tag{2.33}$$

Replacing Equations 2.32 and 2.33 into Equation 2.31, the ratio $f_{FS}^{\tilde{q}s}$ becomes

$$f_{FS}^{\tilde{q}s} = \frac{2}{1+f_{\tilde{q}s}} \tag{2.34}$$

Equation 2.34 shows that the ratio $f_{FS}^{\tilde{q}s}$, as defined by Equation 2.31, depends only on the variable $f_{\tilde{q}s}$ and therefore is valid for both cylindrical and spherical cavities, and for any considered scaled depth, ξ (also, as stated above, the ratio $f_{FS}^{\tilde{q}s}$ is valid for null cavity crown pressure, $\tilde{p}_s = 0$).

Figure 2.10 represents the variation of the ratio $f_{FS}^{\tilde{q}s}$ (vertical axis) with the ratio $f_{\tilde{q}s}$ (horizontal axis). As expected, the ratio is one when $f_{\tilde{q}s} = 0$ and tends to zero as $f_{\tilde{q}s}$ tends to infinity.

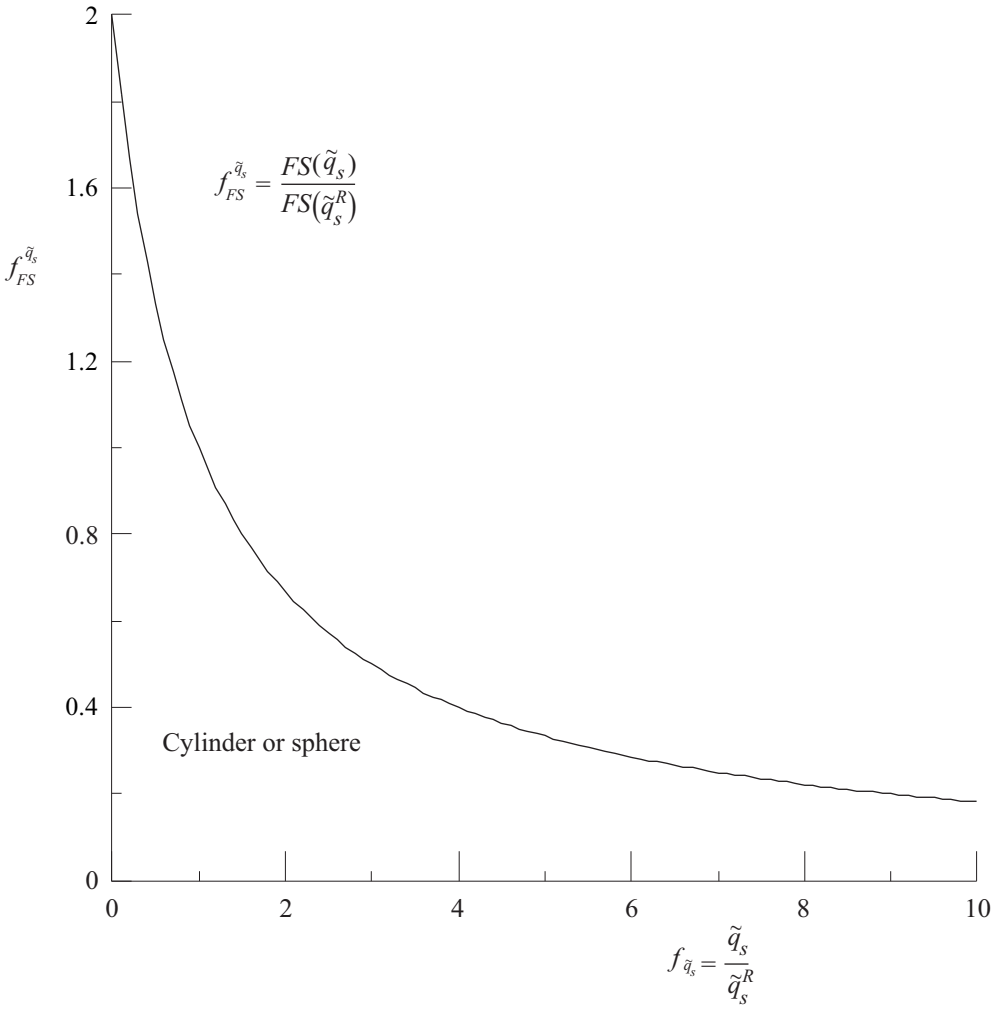

Figure 2.10: Relationship between scaled factor of safety and scaled ground surcharge load for cylindrical and spherical cavities

Chapter 3

Extension of Caquot's solution accounting for water in the ground

3.1 Problem Statement

The extension of Caquot's cavity problem that considers water in the ground is presented in Figure 3.1, for the case of the water surface above the ground surface, and in Figure 3.2, for the case of the water surface below the ground surface.

In Figures 3.1 and 3.2 the ground is considered to be completely saturated below the water level and in Figure 3.2 to be completely dry above the water level. The unit weight of the dry ground and saturated ground are denoted as γ_d and γ_s, respectively. The unit weight of water is denoted by γ_w.

The input variables for the cavities represented in Figures 3.1 and 3.2 are basically the same as for the cavity in dry ground introduced in Section 2.1 (see Figure 2.1) with some minor differences.

A new geometric variable is introduced in Figures 3.1 and 3.2. This variable, h_w, represents the distance between the water surface elevation and the ground surface elevation. As indicated

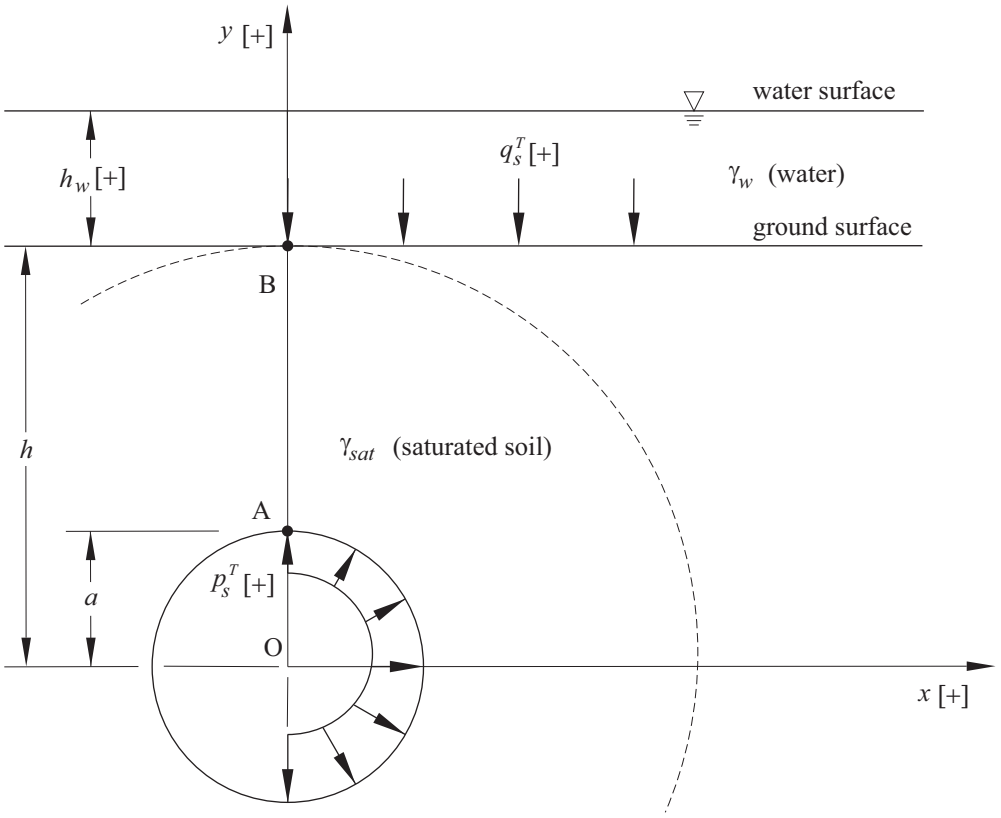

Figure 3.1: Extended Caquot model as applied to the analysis of stability of shallow cavities for the case of a water surface above the ground surface

in Figures 3.1 and 3.2, a water level above the ground surface has a positive value of h_w, and a water level below the ground surface has a negative value of h_w.

For the problem represented in Figure 3.2, the minimum value of h_w to be considered corresponds to the situation in which the water surface coincides with the crown of the cavity (Point A in Figure 3.2). This minimum value, denoted as h_w^{min}, is

$$h_w^{min} = -(h-a) \tag{3.1}$$

Since for the case of saturated ground the factor of safety will be defined in terms of the stress state along the crown-ground segment A-B only, the situation for which $h_w = h_w^{min}$ (or $h_w < h_w^{min}$)

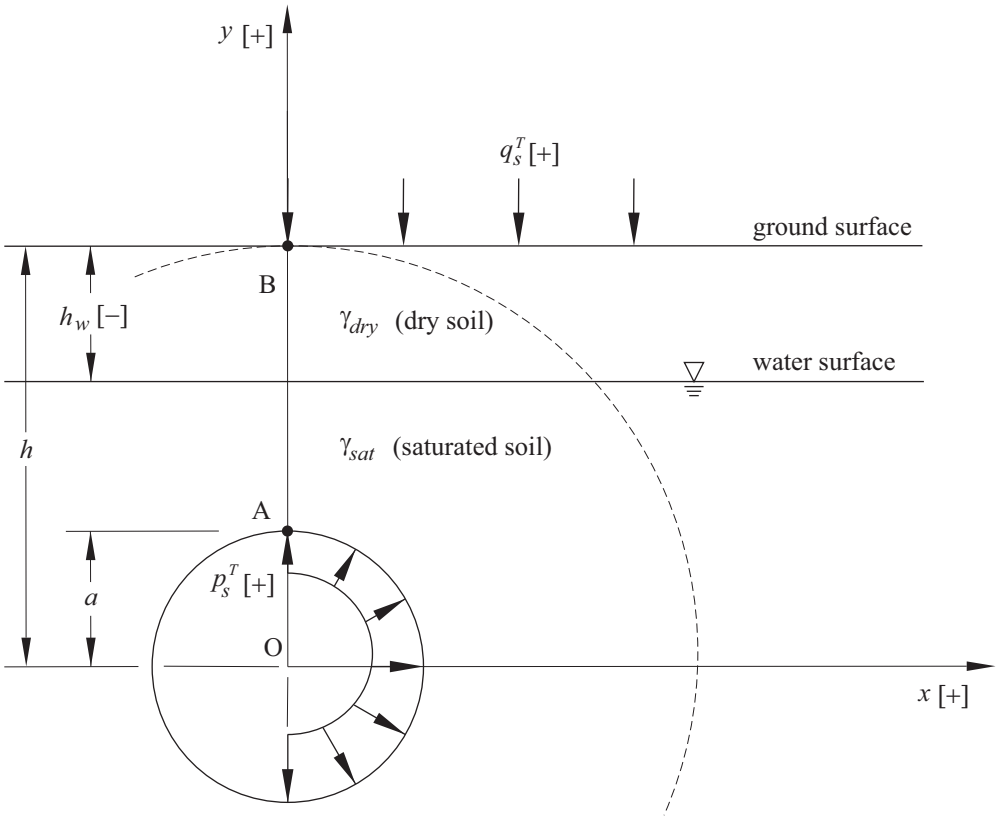

Figure 3.2: Extended Caquot model as applied to the analysis of stability of shallow cavities for the case of a water surface below the ground surface

is considered to be equivalent to the case of a cavity in dry ground, as discussed in Chapter 2.1 (i.e., if $h_w \leq h_w^{min}$, the ground on segment A-B in Figure 3.2 is dry).

To account for the influence of internal water pressure acting at the crown of the cavity and the water pressure acting on the ground surface, the pressure quantities, p_s and q_s, are assumed to be composed of a mechanical part and hydraulic parts.

If the total internal pressure acting on at the crown of the cavity is denoted as p_s^T, and the mechanical and hydraulic parts are denoted as p_s^M and p_s^W, respectively, then the total internal

pressure is

$$p_s^T = p_s^M + p_s^W \tag{3.2}$$

In Equation 3.2, the mechanical component, p_s^M, is equivalent to the internal pressure for dry ground, p_s, introduced in Chapter 2. The hydraulic component, p_s^W, depends on whether the cavity itself is assumed to be *dry* (with the ground surrounding the cavity still having the hydrostatic pressure associated to the water surface), or *flooded*.

For the case of *flooded* cavity, the hydraulic component, p_s^W, is

$$p_s^W = \gamma_w (h + h_w - a) \tag{3.3}$$

while for the case of *dry* cavity, the hydraulic component, p_s^W, is

$$p_s^W = 0 \tag{3.4}$$

Similarly, if the total ground surcharge load is denoted as q_s^T, and the mechanical and hydraulic parts are denoted as q_s^M and q_s^W, respectively, then the total ground surcharge load is

$$q_s^T = q_s^M + q_s^W \tag{3.5}$$

In Equation 3.5, the mechanical component, q_s^M, is equivalent to the ground surcharge load for dry ground, q_s, introduced in Chapter 2. The hydraulic component, q_s^W, depends on whether the water surface is above or below the ground surface. For the case of water surface above the ground surface, the hydraulic component, q_s^W, is

$$q_s^W = \gamma_w h_w \tag{3.6}$$

while for the case of water surface below the ground surface, the hydraulic component, q_s^W, is

$$q_s^W = 0 \tag{3.7}$$

3.2 Scaled form of Caquot's solution

Again, in order to present the solution of the problem introduced in the previous section in a concise and neat manner, the variables associated with existence of water in the ground are scaled in a similar form as done in Section 2.2.

The dimensionless variable ξ_w is the ratio of the distance from the water surface to the ground surface, h_w, and the radius of the cavity, a

$$\xi_w = \frac{h_w}{a} \tag{3.8}$$

In view of Equation 3.8, a dimensionless variable ξ_w^{min} will be associated to the minimum value of water surface elevation, h_w^{min}, defined by Equation 3.1, as follows

$$\xi_w^{min} = -\xi + 1 \tag{3.9}$$

Note that the dimensionless variable ξ_w^{min} is always negative.

Two factors (or ratios) relating unit weights of ground and water are also introduced. The ratio of the saturated unit weight of the ground, γ_s, and dry unit weight of the ground, γ_d, is denoted as f_{sd},

$$f_{sd} = \frac{\gamma_s}{\gamma_d} \tag{3.10}$$

Similarly, the ratio of unit weight of water, γ_w, and a dry unit weight of the ground, γ_d, is denoted as f_{wd},

$$f_{wd} = \frac{\gamma_w}{\gamma_d} \tag{3.11}$$

Next, the total internal pressure, $\tilde{p}_s^T$, and total ground surcharge load, $\tilde{q}_s^T$, introduced in the previous section (Equations 3.2 and 3.5, respectively) are scaled in a similar way as for the case of dry ground in Section 2.2 (see Equation 2.7)

$$\tilde{p}_s^T = \tilde{p}_s^M + \tilde{p}_s^W \tag{3.12}$$

and

$$\tilde{q}_s^T = \tilde{q}_s^M + \tilde{q}_s^W \tag{3.13}$$

For the case of *flooded* cavity, the scaled hydraulic component, $\tilde{p}_s^W$, is obtained by applying the scaling rules (and factor f_{wd}) introduced above to Equation 3.3, and results

$$\tilde{p}_s^W = f_{wd}\,(\xi + \xi_w - 1) \tag{3.14}$$

while for the case of *dry* cavity, the scaled hydraulic component, $\tilde{p}_s^W$, is still zero (see Equation 3.4)

$$\tilde{p}_s^W = 0 \tag{3.15}$$

Similarly, for the case of water surface above the ground surface, the scaled hydraulic component, $\tilde{q}_s^W$, results (see Equation 3.6)

$$\tilde{q}_s^W = f_{wd}\,\xi_w \tag{3.16}$$

while for the case of water surface below the ground surface, the scaled hydraulic component, $\tilde{q}_s^W$, is still zero (see Equation 3.7)

$$\tilde{q}_s^W = 0 \tag{3.17}$$

Considering that the cavities in Figures 3.1 and 3.2 are at the verge of equilibrium, and analyzing the state of stress along the crown-surface segment A-B, as explained in Section 2.2, the value of scaled total (crown) pressure, $\tilde{p}_s^T$, required to maintain equilibrium results as follows (Appendix B provides the derivation of the equations below).

For the case of water surface *above* the ground surface (see Figure 3.1),

$$\tilde{p}_s^T = \tilde{q}_s^T + f_{sd}\,(\xi - 1) - 2\tilde{c}k\ln\xi \tag{3.18}$$

For the case of water surface *below* the ground surface (see Figure 3.2),

$$\tilde{p}_s^T = \tilde{q}_s^T + f_{sd}\,(\xi + \xi_w - 1) - \xi_w - 2\tilde{c}k\ln\xi \tag{3.19}$$

3.3 Computation of factor of safety for Caquot's solution

Obtaining factors of safety, *FS*, for the cavities in Figures 3.1 and 3.2 involve applying the same procedure explained in Section 2.3, this time using Equations 3.18 and 3.19, respectively, and considering that the total internal pressure and total ground surcharge in these equations are decomposed into mechanical and hydraulic parts (Equations 3.12 through 3.17), and cases of flooded and dry cavities are being considered. The following are the resulting equations for factors of safety.

For the case of water surface *above* the ground surface, and *flooded* cavity,

$$FS = \frac{2\tilde{c}k\ln\xi}{\tilde{q}_s^M - \tilde{p}_s^M + (f_{sd} - f_{wd})(\xi - 1)} \tag{3.20}$$

For the case of water surface *above* the ground surface, and *dry* cavity,

$$FS = \frac{2\tilde{c}k\ln\xi}{\tilde{q}_s^M - \tilde{p}_s^M + f_{wd}\,\xi_w + f_{sd}(\xi - 1)} \tag{3.21}$$

For the case of water surface *below* the ground surface, and *flooded* cavity,

$$FS = \frac{2\tilde{c}k\ln\xi}{\tilde{q}_s^M - \tilde{p}_s^M - \xi_w + (f_{sd} - f_{wd})(\xi + \xi_w - 1)} \tag{3.22}$$

For the case of water surface *below* the ground surface, and *dry* cavity,

$$FS = \frac{2\tilde{c}k\ln\xi}{\tilde{q}_s^M - \tilde{p}_s^M - \xi_w + f_{sd}(\xi + \xi_w - 1)} \tag{3.23}$$

A first observation to be made is the same as in Section 2.4 for the case of cavities in dry ground. In all the equations to compute factor of safety for water in the ground (Equations 3.20 through 3.23) the parameter k, which dictates whether the cavity is cylindrical or spherical, acts as a multiplier in the numerator of the equations. Therefore, the factor of safety for a spherical cavity (considering $k = 2$ in the equations above) will always be two times the value of factor of safety for a cylindrical cavity (considering $k = 1$ the equations above), certainly, with all other input parameters being the same.

A second observation to be made is that the equations for factor of safety presented above, that apply for the case where there is water in the ground, recover the equation for factor of safety for dry ground (Equation 2.20) when no water is assumed to exist in the ground. Indeed, if the factors $f_{sd} = 1$ (unit weight of the saturated ground is equal to unit weight of the dry ground) and $f_{wd} = 0$ (unit weight of the water is zero, i.e., there is no water present) are replaced in Equations 3.20 through 3.23, all four equations become

$$FS = \frac{2\tilde{c}k\ln\xi}{\tilde{q}_s^M - \tilde{p}_s^M + \xi - 1} \tag{3.24}$$

which is the same Equation 2.20 obtained for dry ground in Chapter 2.

A third observation related to the second observation above is that the equations for water surface *below* the ground surface (Equations 3.22 and 3.23) also recover the equation for factor of safety for dry ground (Equation 2.20) when the scaled elevation of the water surface is taken to coincide with the crown of the cavity. This can be easily confirmed replacing ξ_w in Equations 3.22 and 3.23, by ξ_w^{min} as in Equation 3.9. With this replacement both Equations 3.22 and 3.23 become 3.24 corresponding to cavities in dry ground.

A fourth observation to be made is that the equations for water surface *above* the ground surface (Equations 3.20 and 3.21) and *below* the ground surface (Equations 3.22 and 3.23) become the same when the water level is assumed to coincide with the ground surface ($h_w = 0$ in Figures 3.1 and 3.2). Indeed, making $\xi_w = 0$ in Equations 3.20 through 3.23, the factor of safety for cases in which the water surface coincides with the ground surface become as follows.

For the case of *flooded* cavity,

$$FS = \frac{2\tilde{c}k\ln\xi}{\tilde{q}_s^M - \tilde{p}_s^M + (f_{sd} - f_{wd})(\xi - 1)} \tag{3.25}$$

For the case of *dry* cavity,

$$FS = \frac{2\tilde{c}k\ln\xi}{\tilde{q}_s^M - \tilde{p}_s^M + f_{sd}(\xi - 1)} \tag{3.26}$$

Another consideration to be made is with regard to the solution of factor of safety for *dry* cavities (Equations 3.21, 3.23 and 3.26). The solution for a dry cavity assumes that the hydraulic pressure in the ground surrounding the cavity is hydrostatic and associated to the water surface position, and that the water pressure on the periphery of the cavity is zero. To facilitate the discussion, the case in which there is no mechanical support pressure inside the cavity is considered. Under such condition, the total radial stress on the periphery of the cavity (just inside the ground) is zero, while the water pressure is different from zero. Besides the existence of an infinite hydraulic gradient (that will result in water rapidly flowing into the cavity), the effective radial stress on the periphery of the cavity (just inside the ground) will be negative (i.e., it will be tensile). If the ground has a tensile strength that is lower than the resulting effective (tensile) stress, the tensile effective stress will produce a progressive (and expanding) tensile failure region around the cavity that will eventually produce the collapse of the cavity. Therefore, the expressions for computing factors of safety for assumed dry cavities, Equations 3.21, 3.23 and 3.26, also consider that no tensile failure of the ground occurs (e.g., the ground has enough tensile strength to overcome the type of failure just explained) and that the infinite hydraulic gradient is maintained. With regard to this infinite hydraulic gradient, the solution for factor of safety for dry cavities could be regarded as a hypothetical limiting 'instantaneous' condition after excavation in a relatively impermeable ground, just before water starts flowing into the cavity and the water pressure in the ground surrounding the cavity has not started to dissipate yet.

3.4 Comparison with cavity in dry ground

This section investigates how the presence of water in the ground affects the stability of cylindrical or spherical cavities. The solution of factor of safety for different hydraulic conditions obtained in the previous section are compared with the solution of factor of safety for dry

ground, presented already in Chapter 2. The cases of water surface coinciding with the ground surface and water surface above and below the ground surface are discussed separately.

3.4.1 Case of water surface coinciding with ground surface

Figure 3.3 represents the relationship between factor of safety, *FS*, (vertical axis) and scaled cohesion, $\tilde{c}$, (horizontal axis) as a function of hydraulic conditions assumed for a cylindrical cavity when the water surface coincides with the ground surface. Factors of safety corresponding to a flooded cavity (computed with Equation 3.25), dry cavity (computed with Equation 3.26) and cavity in dry ground (computed with Equation 3.24) are represented. Figure 3.3 considers that the cylindrical cavity is located at a scaled depth $\xi = 2.5$ below the ground surface and that the mechanical component of both, cavity crown pressure and ground surcharge load, are zero ($\tilde{p}_s^M = 0$ and $\tilde{q}_s^M = 0$, respectively). Figure 3.3 also considers that the factors f_{sd} and f_{wd} (defined in Equations 3.10 and 3.11, respectively) are equal to 1.125 and 0.625, respectively (these values have been obtained considering arbitrary but commonly found values of saturated unit weight of ground equal to 18 kN/m^3, dry unit weight of ground equal to 16 kN/m^3, and unit weight of water equal to 10 kN/m^3). As for the case of cavities in dry ground, Figure 3.3 shows that as the cohesion of the ground increases (when moving to the right on the horizontal axis), the factor of safety increases. Also, Figure 3.3 shows that the factor of safety for a flooded cavity is larger than for a cavity in dry ground, and that the factor of safety for a cavity in dry ground is larger than for a dry cavity in saturated ground.

Sections 3.4.2 and 3.4.3 below present a dimensionless representation of the difference in magnitude of factor of safety for cases of flooded and dry cavities with the case of cavity in dry ground, for both cases of water surface *above* and *below* the ground surface, respectively. The limiting case of water surface coinciding with the ground surface, as represented in Figure 3.3, will be discussed further in the sections below.

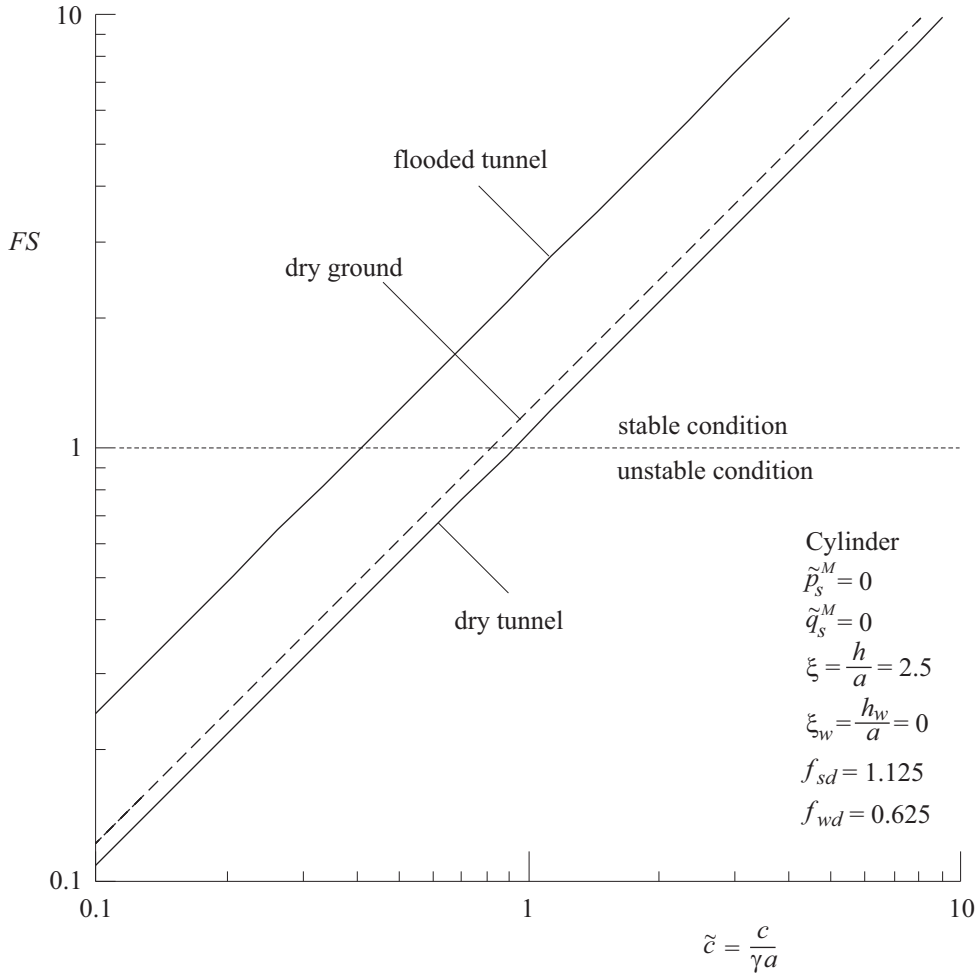

Figure 3.3: Relationship between factor of safety and scaled cohesion for the case of water surface coinciding with the ground surface, and cases of flooded and dry cavities. The case of dry ground is also represented for comparison

3.4.2 Case of water surface above ground surface

Figure 3.4 shows a similar representation as in Figure 3.3, this time considering that the water surface is above the ground surface, with $\xi_w = 1$ (all other variables, including ξ, $\tilde{p}_s^M$, $\tilde{q}_s^M$, f_{sd} and f_{wd} are considered the same as in Figure 3.3). Comparing the relative position of the lines corresponding to flooded and dry cavity, and cavities in dry ground in Figures 3.4 and 3.3, the only change is in the position of the line corresponding dry cavity, which now predicts a factor of safety that is lower to the one corresponding to cavity in dry ground. In other words, as the level of the water surface rises above the ground level, the factor of safety for dry cavity decreases, with the one for flooded cavity remaining the same.

The fact that the factor of safety for the case of flooded cavity does not depend on the elevation of the water surface above the ground surface is an expected result, since it is a well known principle of soil mechanics that the effective stress below a submerged surface does not change with the elevation of the water that floods the surface (Coduto et al., 2011).

To obtain a unique dimensionless representation that allows to quantify how the factor of safety for flooded and dry cavities vary with the elevation of the water surface, ξ_w, and that is valid for both cylindrical and spherical cavities for any considered scaled depth ξ (and for the values of $\tilde{p}_s^M$, $\tilde{q}_s^M$, f_{sd} and f_{wd} considered in Figures 3.3 and 3.4), the ratio $f_{FS}^{W\text{-}D}$ is defined as follows

$$f_{FS}^{W\text{-}D} = \frac{FS\ [\text{Water in ground}]}{FS\ [\text{Dry ground}]} \tag{3.27}$$

The numerator in Equation 3.27 represents the factor of safety obtained for flooded or dry cavities for arbitrary values of ξ_w (obtained with Equations 3.20 or 3.21, respectively), while the denominator in Equation 3.27 represents the factor of safety obtained for cavities in dry ground (obtained with Equation 3.24).

To make the mentioned dimensionless representation valid for any value of scaled water surface elevation, ξ_w, whether above or below the ground surface, and for any scaled depth of

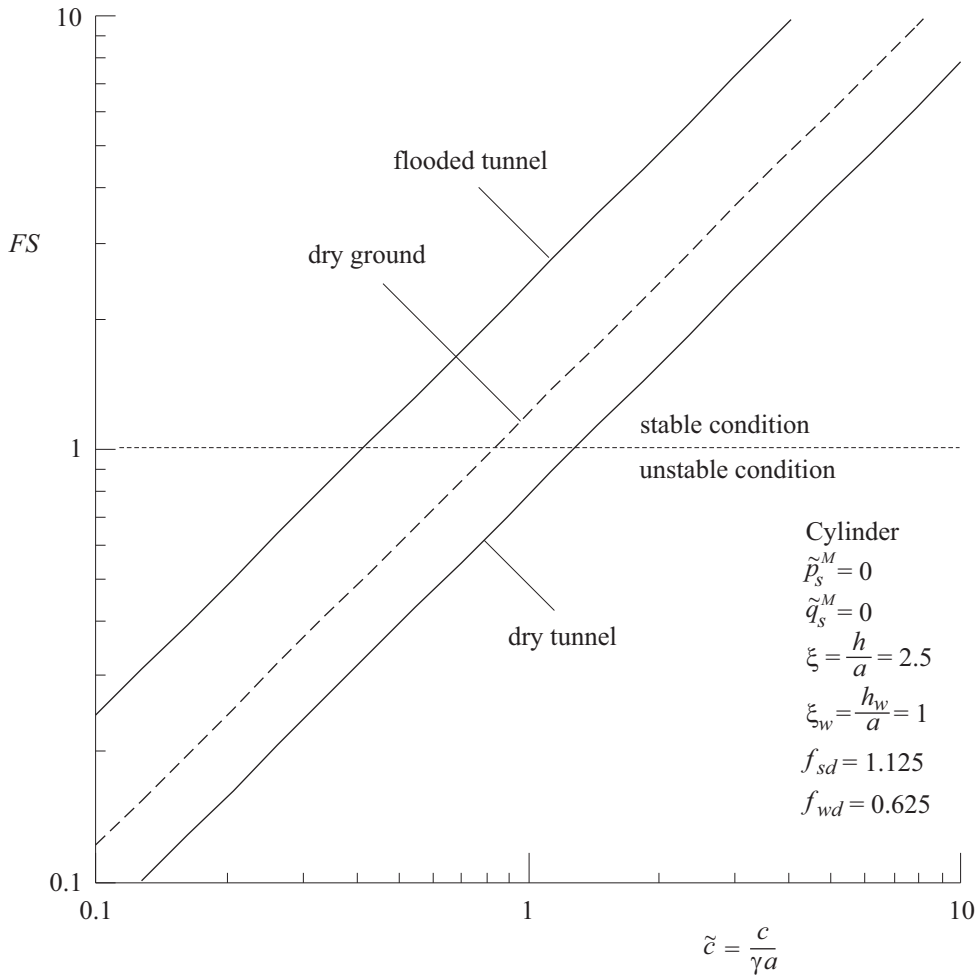

Figure 3.4: Relationship between factor of safety and scaled cohesion for the case of water surface above the ground surface, and cases of flooded and dry cavities. The case of dry ground is also represented for comparison

cavity, ξ, the ratio f_{ξ_w} is defined as follows

$$f_{\xi_w} = \frac{\xi_w}{\xi_w^{min}} \tag{3.28}$$

where ξ_w^{min} (which is always negative) is given by Equation 3.9.

Note that the ratio f_{ξ_w} defined in Equation 3.28 can take any value smaller than zero (a negative value) to represent any position of a water surface above ground surface. Also the ratio f_{ξ_w} takes the value zero when the water surface coincides with the ground surface, and takes a value larger than zero to represent any position of water surface below ground surface. The maximum value for the ratio f_{ξ_w} is one, in such case, the water surface coincides with the crown surface as explained in Section 3.1 (see paragraph that follows Equation 3.1).

Expressing the equations that define the factor of safety for the numerator and denominator of Equation 3.27 (Equations 3.20 or 3.21, and Equation 3.24, respectively) in terms of the ratio f_{ξ_w} given by Equation 3.28, yields (after some algebra manipulation) the following equations for $f_{FS}^{W\text{-}D}$.

For the case of *flooded* cavity

$$f_{FS}^{W\text{-}D} = \frac{1}{f_{sd} - f_{wd}} \tag{3.29}$$

For the case of *dry* cavity

$$f_{FS}^{W\text{-}D} = \frac{1}{f_{sd} - f_{wd}\, f_{\xi_w}} \tag{3.30}$$

Also, for the case of dry cavity when $f_{\xi_w} = 0$ (the case for which the water surface coincides with the ground surface), Equation 3.30 gives

$$f_{FS}^{W\text{-}D} = \frac{1}{f_{sd}} \tag{3.31}$$

Equations 3.29 and 3.30 show that the ratio $f_{FS}^{W\text{-}D}$, as defined by Equation 3.27, depends only on the variables f_{ξ_w}, f_{sd} and f_{wd}, and therefore is valid for both cylindrical and spherical cavities, and for any considered scaled cavity depth, ξ (also, and as stated above, the ratio $f_{FS}^{W\text{-}D}$ is

valid for zero values of scaled mechanical cavity crown pressure and scaled mechanical ground surcharge, $\tilde{p}_s^M = 0$ and $\tilde{q}_s^M = 0$, respectively).

Figure 3.5 represents the ratio $f_{FS}^{W\text{-}D}$ (vertical axis) as a function of the ratio $f_{\xi w}$ (horizontal axis) corresponding to flooded and dry cavities (computed with Equations 3.29 and 3.30, respectively), for the same values of parameters f_{sd} and f_{wd} considered in Figures 3.3 and 3.4. The diagram in Figure 3.5 includes also the horizontal line of ordinate equal to one representing cavities in dry ground. The diagram indicates that for the given values of parameters f_{sd} and f_{wd} (corresponding to arbitrary but common values of saturated and dry unit weight of ground and unit weight of water), the factor of safety of a flooded cavity is exactly two times the factor of safety for the same cavity in dry ground, independently of how high the water surface is above the ground surface. Also, the diagram indicates that the factor of safety for a dry cavity decreases as the water surface level increases, and becomes equal to 0.89 times the factor of safety for a cavity in dry ground, when the water surface coincides with the ground surface (the value 0.89 is obtained by replacing $f_{sd} = 1.125$ into Equation 3.31).

The fact that the factor of safety for a flooded cavity in saturated ground is two times the factor of safety for the same cavity in dry ground (for typical values of saturated and dry unit weights for the ground), is a familiar result in the analysis of slope stability. Indeed, it is another well known results in soil mechanics that the factor of safety for an infinite slope in dry ground is typically two times larger than the factor of safety for the same infinite slope when an inclined phreatic surface is considered to coincide with the inclined slope face (Coduto et al., 2011).

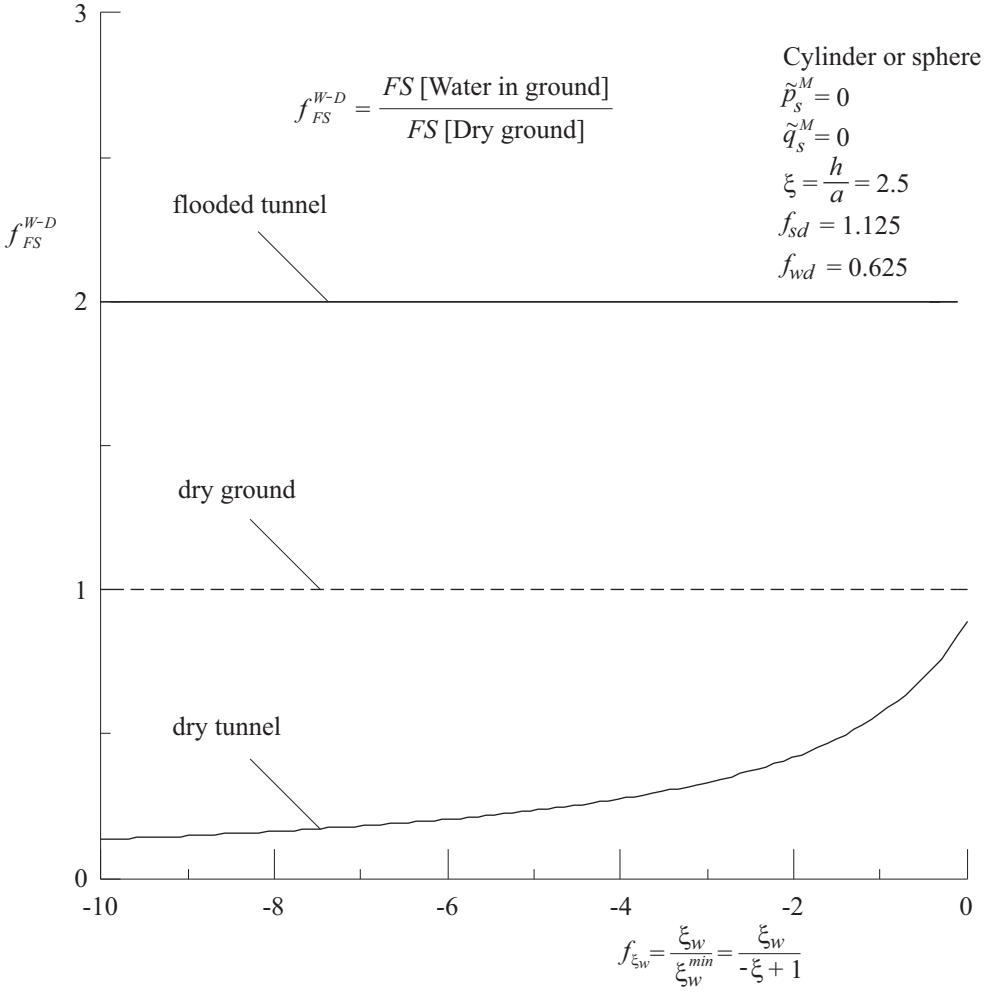

Figure 3.5: Relationship between scaled factor of safety and scaled water surface elevation considered to be above the ground surface, for the cases of flooded and dry cavities. The case of dry ground is also represented for comparison

3.4.3 Case of water surface below ground surface

This section presents a similar analysis to the one presented in the previous section, but for water surface above the ground surface.

Figures 3.6 and 3.7 show equivalent representations as in Figure 3.4 considering that the water surface is below the ground surface, with values $\xi_w = -0.5$ and $\xi_w = \xi_w^{min} = -1.5$, respectively (all other variables, including ξ, $\tilde{p}_s^M$, $\tilde{q}_s^M$, f_{sd} and f_{wd} are considered the same as in Figure 3.4). Comparing the relative position of the lines corresponding to flooded and dry cavities and cavities in dry ground in Figures 3.3, 3.6 and 3.7, it is noticed that as the level of the water surface drops below the ground surface, the differences between factors of safety for flooded and dry cavities with respect to the factor of safety for dry ground decreases. In the limiting case in which the level of the water surface coincides with the level of the crown of the cavity, as expected, all three lines merge into the single line corresponding to the cavity in dry ground (see third observation in the paragraph following Equation 3.24 in Section 3.3).

To quantify the difference between factors of safety for flooded and dry cavities and cavities in dry ground, the same factors $f_{FS}^{W\text{-}D}$ and f_{ξ_w} defined by Equations 3.27 and 3.28, respectively, will be used here for the case of water surface below the ground surface.

For the case of a *flooded* cavity, expressing the equations that define the factor of safety for the numerator and denominator of Equation 3.27 (Equations 3.22 and Equation 3.24, respectively) in terms of the ratio f_{ξ_w} given by Equation 3.28, yields (after some algebra manipulation) the following equation for $f_{FS}^{W\text{-}D}$

$$f_{FS}^{W\text{-}D} = \frac{1}{f_{\xi_w} - (f_{sd} - f_{wd})\left(f_{\xi_w} - 1\right)} \tag{3.32}$$

For the case of *flooded* cavity and when $f_{\xi_w} = 0$ (the case for which the water surface coincides with the ground surface), Equation 3.32 gives

$$f_{FS}^{W\text{-}D} = \frac{1}{f_{sd} - f_{wd}} \tag{3.33}$$

which is the same Equation 3.29 obtained earlier on.

For the case of *flooded* cavity when $f_{\xi w} = 1$ (the case for which the water surface coincides with the cavity crown), Equation 3.32 gives

$$f_{FS}^{W\text{-}D} = 1 \tag{3.34}$$

which means the factor of safety becomes the one corresponding to a cavity in dry ground.

For the case of *dry* cavity, expressing the equations that define the factor of safety for the numerator and denominator of Equation 3.27 (Equations 3.23 and Equation 3.24, respectively) in terms of the ratio $f_{\xi w}$ given by Equation 3.28, yields (after some algebra manipulation) the following equation for $f_{FS}^{W\text{-}D}$

$$f_{FS}^{W\text{-}D} = \frac{1}{f_{\xi w} - f_{sd}\left(f_{\xi w} - 1\right)} \tag{3.35}$$

For the case of *dry* cavity when $f_{\xi w} = 0$ (the case for which the water surface coincides with the ground surface), Equation 3.35 gives

$$f_{FS}^{W\text{-}D} = \frac{1}{f_{sd}} \tag{3.36}$$

which is the same Equation 3.31 obtained earlier on.

For the case of *dry* cavity when $f_{\xi w} = 1$ (the case for which the water surface coincides with the cavity crown), Equation 3.35 gives

$$f_{FS}^{W\text{-}D} = 1 \tag{3.37}$$

which means the factor of safety becomes the one corresponding to a cavity in dry ground.

Figure 3.8 represents the ratio $f_{FS}^{W\text{-}D}$ (vertical axis) as a function of the ratio $f_{\xi w}$ (horizontal axis) corresponding to flooded and dry cavities (computed with Equations 3.32 and 3.35, respectively), for the same values of parameters f_{sd} and f_{wd} considered in Figures 3.6 and 3.7. The diagram in Figure 3.8 includes also the horizontal line of ordinate equal to 1 representing cavities in dry ground. The diagram indicates that for the given values of parameters f_{sd} and f_{wd} (corresponding to arbitrary but commonly found values of saturated and dry unit weight of

ground and unit weight of water), the ratio of factor of safety of a flooded cavity with respect to the corresponding factor of safety for a cavity in dry ground decreases from the value 2 (see explanation of this value in Section 3.4.2), to the value of 1, as the elevation of the water surface drops from the elevation of the ground surface, to the elevation of the crown of the cavity, respectively. Similarly, the ratio of factor of safety of a dry cavity with respect to the corresponding factor of safety for a cavity in dry ground increases from the value 0.89 (see explanation of this value in Section 3.4.2), to the value 1, as the elevation of the water surface drops from the elevation of the ground surface, to the elevation of the crown of the cavity, respectively.

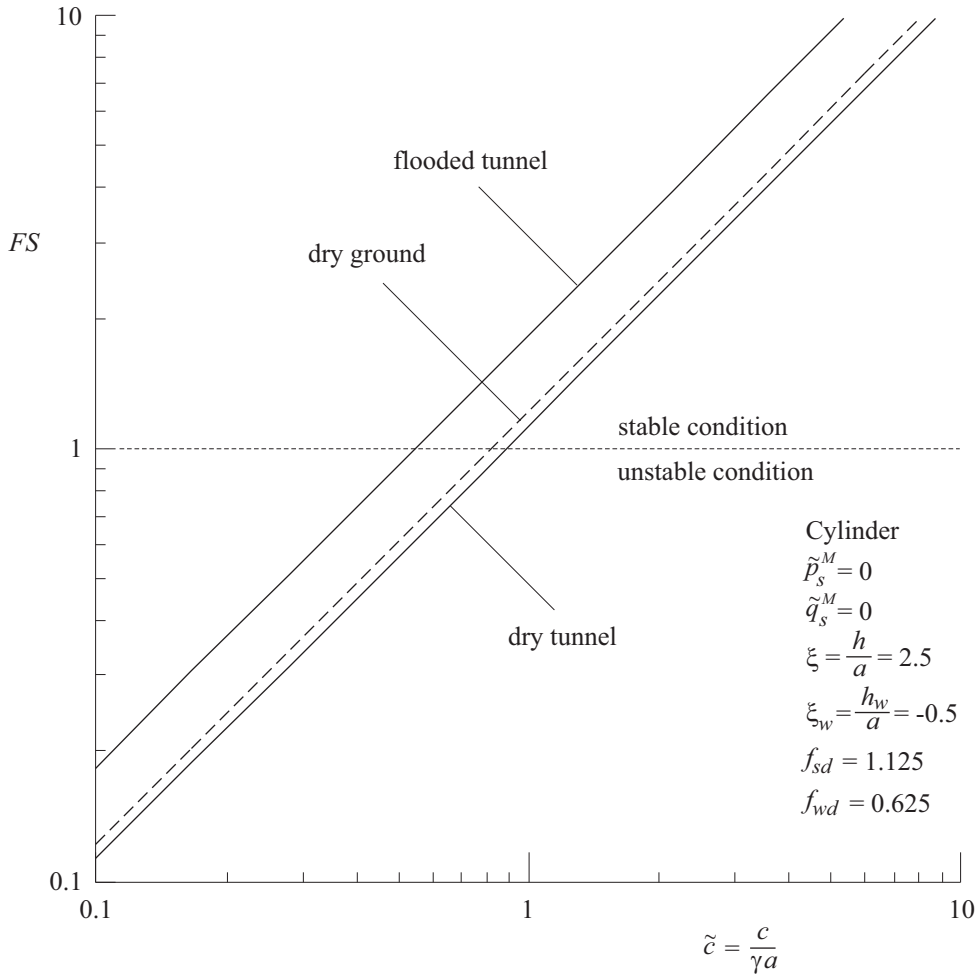

Figure 3.6: Relationship between factor of safety and scaled cohesion for the case of water surface below the ground surface, and cases of flooded and dry cavities. The case of dry ground is also represented for comparison

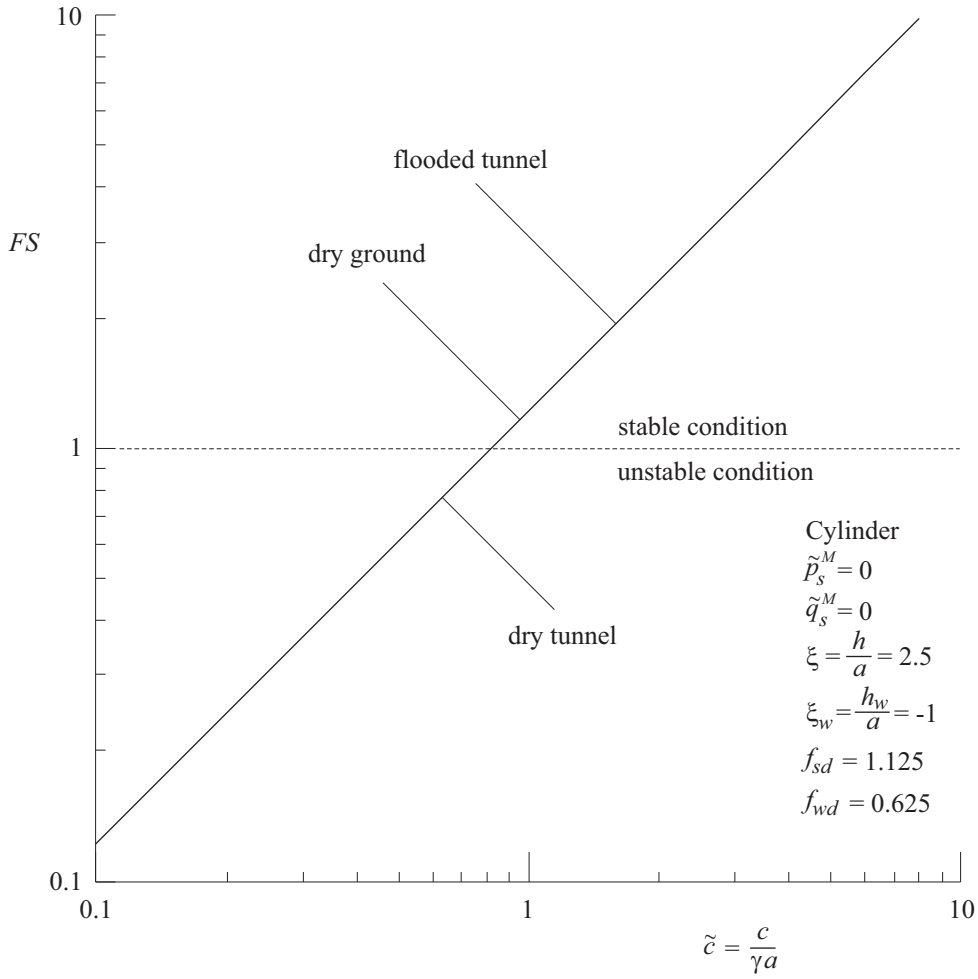

Figure 3.7: Relationship between factor of safety and scaled cohesion for the case of water surface at the lowest elevation, and cases of flooded and dry cavities. The case of dry ground is also represented for comparison

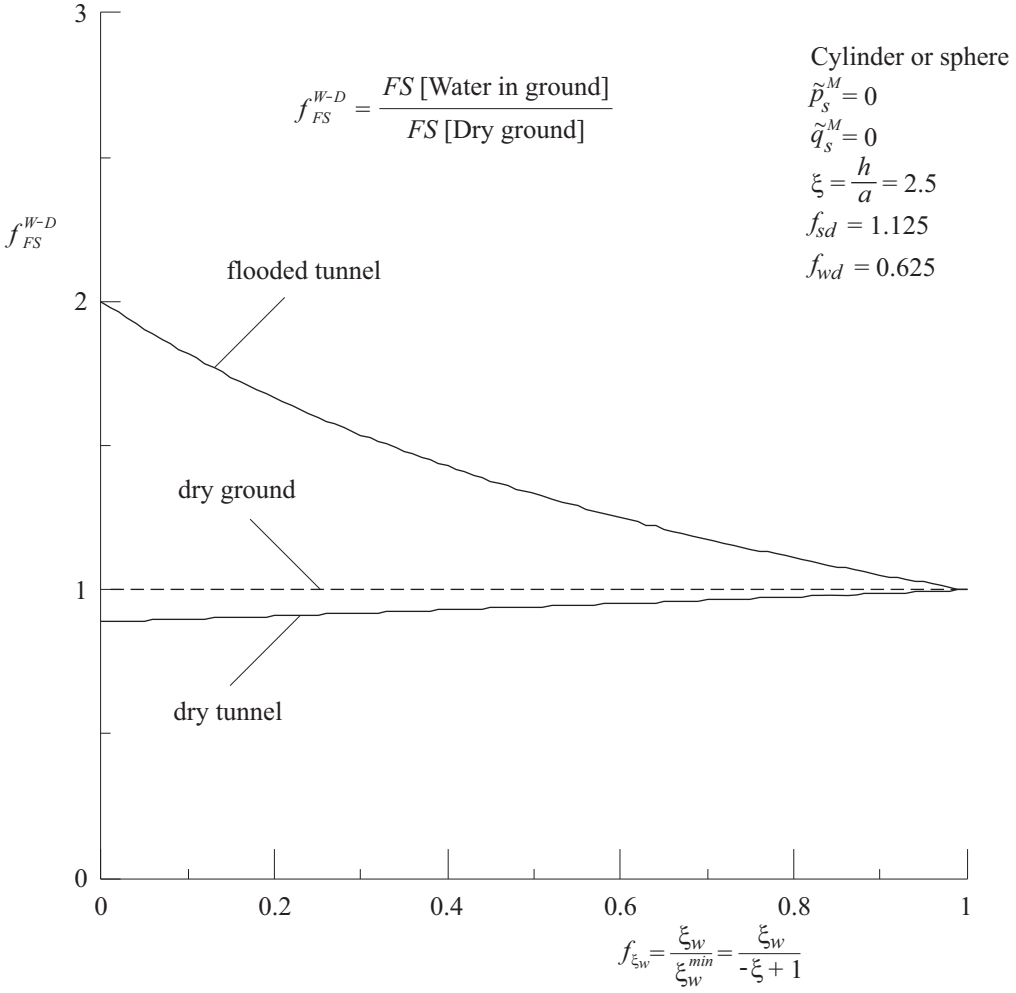

Figure 3.8: Relationship between factor of safety and scaled cohesion for the case of water surface below the ground surface, and cases of flooded and dry cavities. The case of dry ground is also represented for comparison

Chapter 4

Comparison of Caquot's solution with numerical models

4.1 FLAC® models

FLAC® stands for *Fast Lagrangian Analysis of Continua*. This software, developed and commercialized by Itasca Inc. in Minneapolis, Minnesota, uses the *finite difference method* to simulate complex behaviors of materials such as rock and soil (Itasca, 2011). FLAC® has been used in this thesis to model the problem of stability of shallow circular cavities and determining factors of safety as it will be explained next.

Figure 4.1 shows a typical model of a shallow cavity used in this study. The notation for geometry and load variables in Figure 4.1 corresponds to the same notation in the Figure 2.1 in Chapter 2, and Figures 3.1 and 3.2 in Chapter 3. The mesh represented in Figure 4.1 allows to compute the redistribution of stresses and displacements after excavation of cylindrical cavities under plane strain conditions, or a spherical cavities using the axi-symmetry feature of the software.

The circular cavity represented in Figure 4.1 corresponds to a cavity at a scaled depth $\xi =$

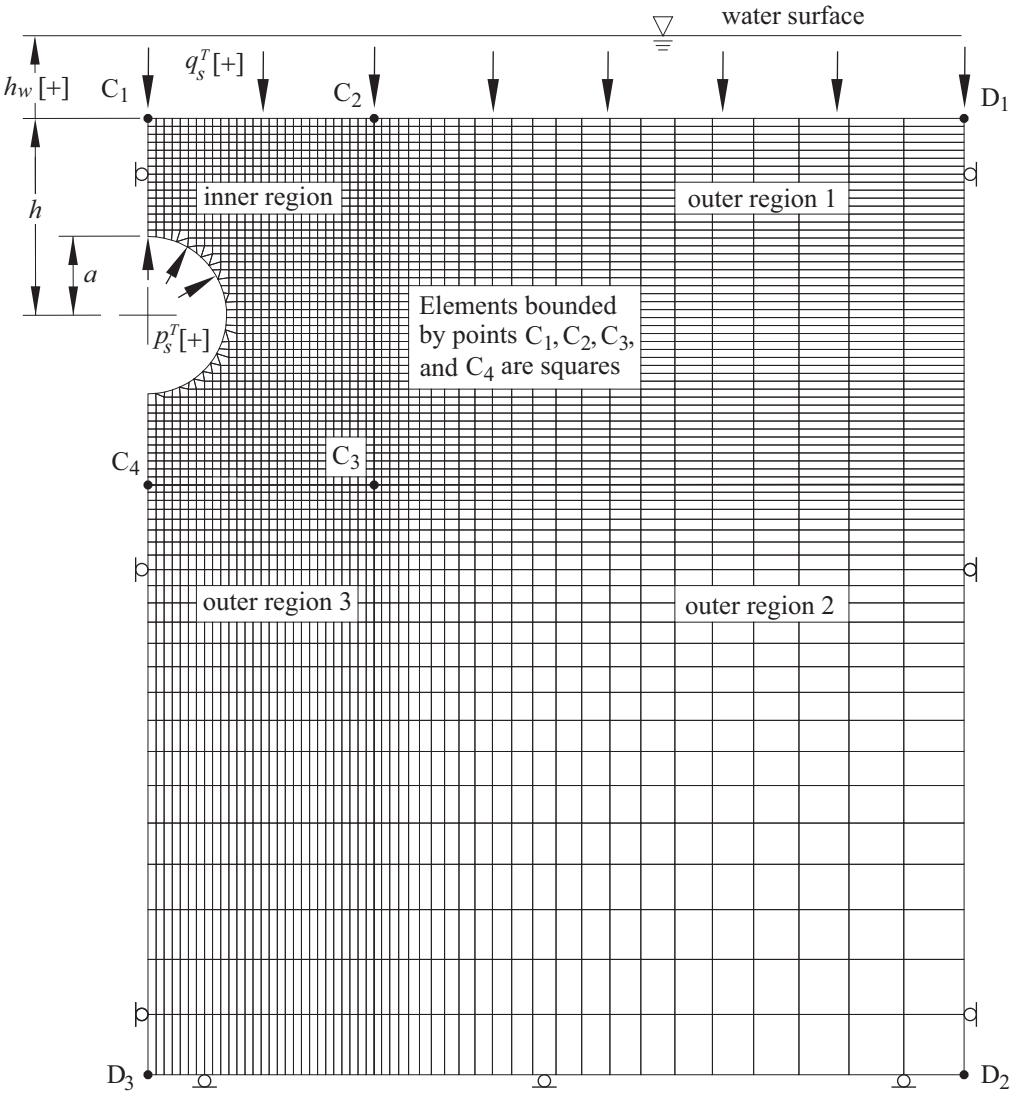

Figure 4.1: Example of FLAC® model used to perform the numerical analysis component of this research

$h/a = 2.5$. Note that due to symmetry, only half of the cavity problem needs to be modelled. Indeed, the left boundary of the model in Figure 4.1 represents a symmetry plane in the case of the cylindrical tunnel and the axi-symmetry line in the case of the spherical cavity. The mesh represented in Figure 4.1 consists of five different regions. These regions are the "cavity region" (which is modelled as null material), the "inner region" for which elements are mostly square, and three "outer regions" that extend to the represent the far boundaries of the models (for the latter regions, the side lengths of elements progressively increase as the elements become closer to the external boundaries of the models). Note that for the "inner region" represented in Figure 4.1, the side lengths of the (mostly) square elements are 0.1 times the radius of the cavity, a.

In FLAC® (as in any other finite difference method or finite element method software), solution of excavation problems in assumed plastic (or elasto-plastic) material with given strength properties involves an iterative process, that has the objective of finding redistributed stress and displacement field quantities that satisfy force equilibrium equations, compatibility of deformations equations, material constitutive equations and boundary conditions (see, for example, Potts & Zdravkovic, 1999). If the iterative process converges, it means that a static solution that satisfies all governing equations has been found. If the iterative process does not converge, it means that no static solution has been found, and this is interpreted as if the model (in this case the cavity) collapses for the given strength properties.

FLAC® has been used to calculate the factor of safety, *FS*, for different cavity configurations by application of the *strength reduction technique* (see, for example, Dawnson, Roth, & Drescher, 1999). When applying the strength reduction technique to a shallow cavity in Tresca material, two cases have to be distinguished.

The first case, represented in Figure 4.2, considers that for the given value of cohesion, c, a static solution for the stress and displacement fields is possible, and the cavity reaches equilibrium after excavation (note that the diagram in Figure 4.2 represents the Tresca failure envelope

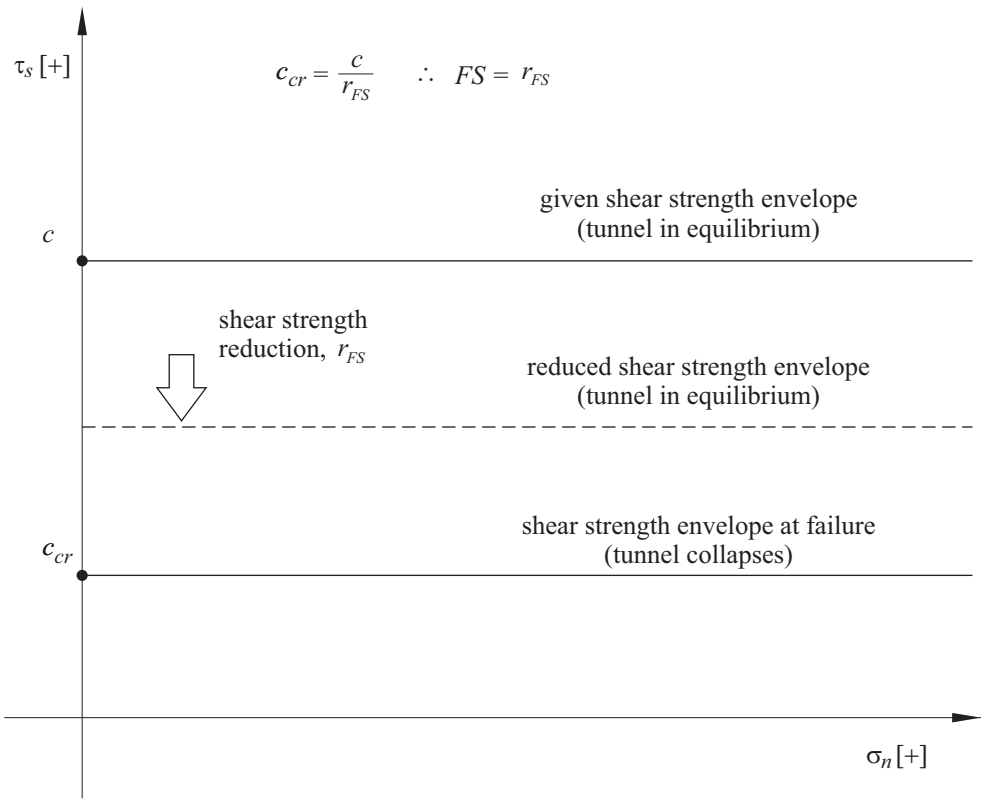

Figure 4.2: Strength reduction technique for the case when the given ground strength leads to a stable shallow excavation

in the 2D space of shear and normal stresses, see Figure 2.3). In such case, the strength reduction technique consists in solving the same cavity problem several times, each time considering a decreased value of cohesion obtained by multiplying the given value of cohesion, c, by a factor r_{FS}, where $r_{FS} < 1$ (see Figure 4.2). The problem is solved until a critical value of cohesion, c_{cr}, is found, for which the iterative process done by the software does not converge anymore, indicating that the cavity is collapsing. Then, for the values of c and c_{cr} (or $\tilde{c}$ and $\tilde{c}_{cr}$), the factor of safety for the cavity is computed using the same Equation 2.18 discussed in Section 2.3 of Chapter 2.

The second case that the strength reduction technique distinguishes is represented in Figure

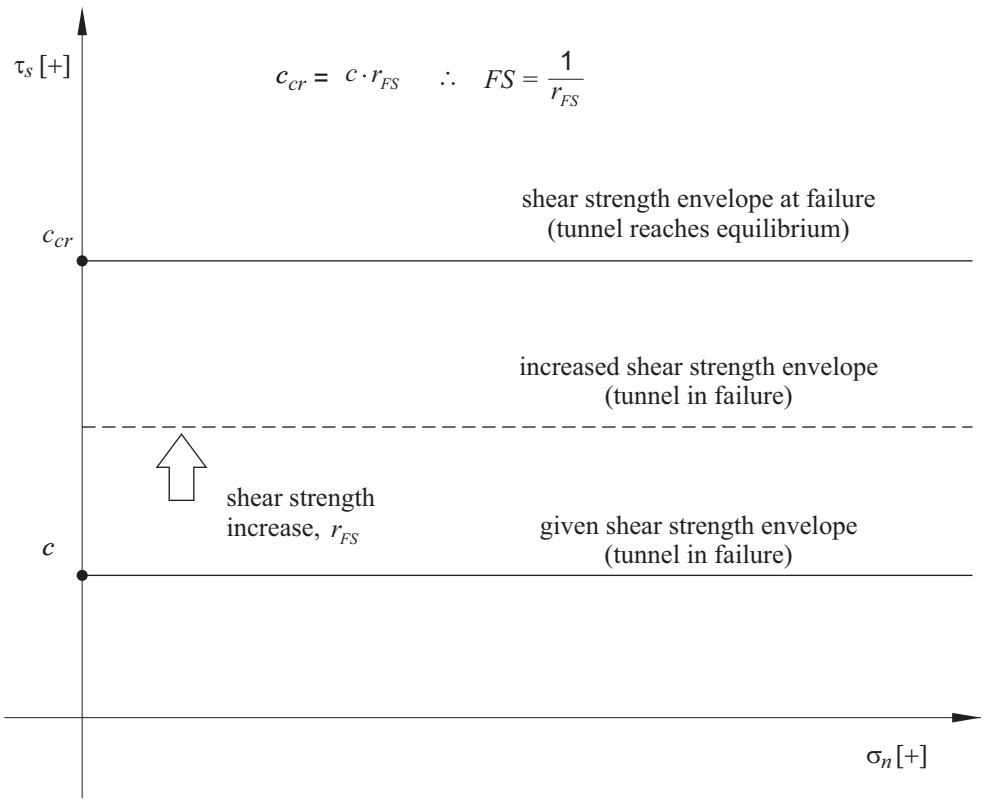

Figure 4.3: Strength reduction technique for the case when the given ground strength leads to an unstable shallow excavation

4.3. This case considers that for the given value of cohesion, c, a solution for the stress and displacement fields is not possible, and the cavity collapses after excavation. In such case, the strength reduction technique consists in solving the same cavity problem several times, each time considering an increased value of cohesion obtained by multiplying the given value of cohesion, c, by a factor r_{FS}, where $r_{FS} > 1$ (see Figure 4.3). The problem is solved until a critical value of cohesion, c_{cr}, is found, for which the iterative process done by the software converges, indicating that the cavity reaches the static equilibrium. Then, the factor of safety for the cavity is computed using the same Equation 2.18 (Chapter 2).

Figure 4.4 represents a sequence of application of the strength reduction technique in FLAC®,

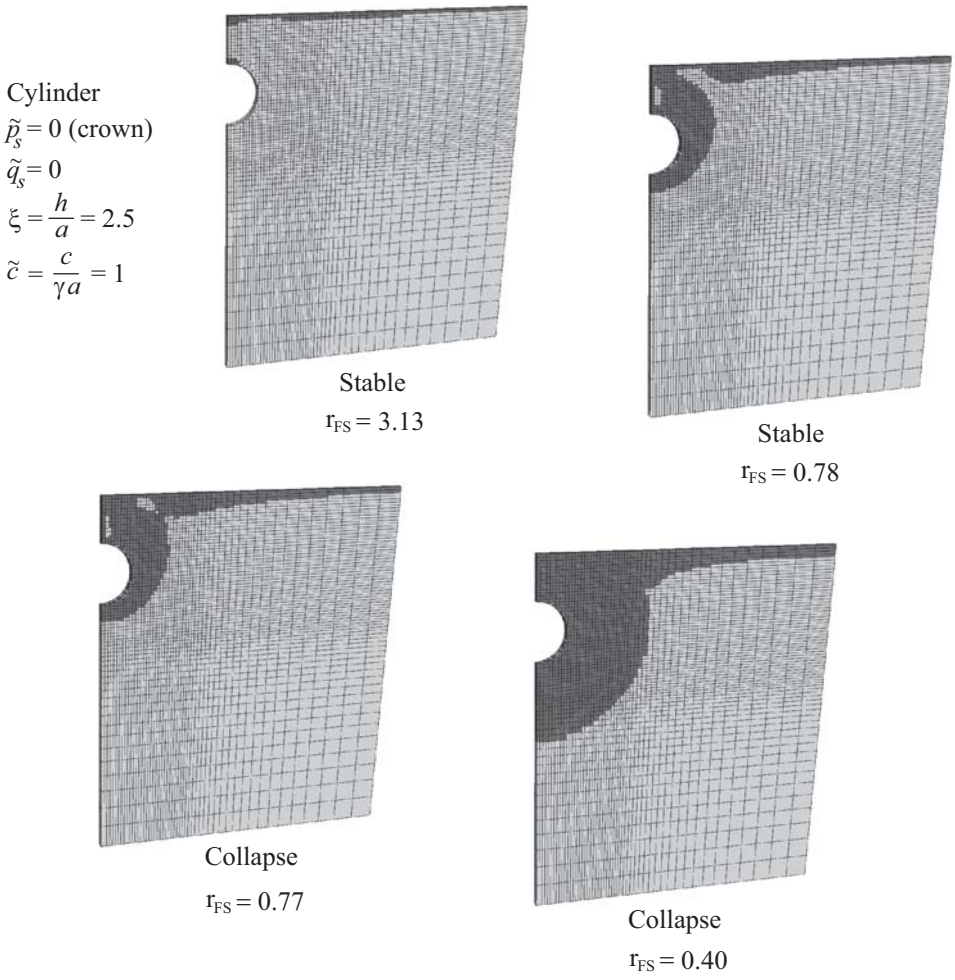

Figure 4.4: Application of the strength reduction technique to the FLAC® models. The different plots show a sequence of reduction of ground strength. Shaded regions indicate elements behaving plastically

for shallow cavities with scaled depth $\xi = 2$. The model on top corresponds to a cavity that reaches static equilibrium for a given value of cohesion (the case of Figure 4.2). The models below the top one, correspond to a sequence of cases of the same model with decreasing values of cohesion, obtained by considering different values of the factor r_{FS} (input variables are indicated in Figure 4.4). In Figure 4.4, the shaded regions around the cavities indicate elements failing plastically; note that the extent of the plastic zones increases as the cohesion is decreased further. In Figure 4.4, the lowermost model, corresponds to the case in which the static equilibrium is not found by the software. This model defines the factor of safety for the cavity, as explained earlier on.

4.2 Comparison of factors of safety obtained with analytical and numerical models

This section presents a comparison of factor of safety results obtained using the strength reduction technique in FLAC® with the corresponding extended Caquot's solution for dry ground (as presented in Chapter 2). As discussed in Section 1.3 (Chapter 1), when the size of the elements in the mesh is small enough, the numerical FLAC® results can be reasonably assumed to be close to the 'true' results for factor of safety. This is in view that numerical solutions satisfy all governing equations for the elasto-plastic problem.

In this section, the comparison of analytical and numerical results will center in particular selected variables that control the resulting factors of safety. In this regard, although many additional variables could have been selected for investigation, for the sake of limiting the scope and length of this thesis work, only some variables have been selected for analysis. The variables to be investigated are the cavity depth, the cavity type (wether cylindrical or spherical), the type of internal pressure distribution acting on the cavity wall, and the density of the mesh (or size of elements) considered in the FLAC® models. These are discussed separately in the sections

that follow.

4.2.1 Cavity depth

The influence of the cavity depth on the factor of safety computed with the extended Caquot's model for a cylindrical cavity in a Tresca material has been discussed in Section 2.4.1 (see Figure 2.4). Figure 4.5 shows a similar representation as in Figure 2.4 this time including symbols that represent factors of safety obtained numerically (with FLAC®) for different scaled cavities depths (the results are for cases of zero ground surcharge load and zero support pressure at the crown of the cavity, $\tilde{q}_s = 0$ and $\tilde{p}_s = 0$, respectively). To obtain these results, the numerical models consider arbitrary (actually randomly generated) input variables such as cavity radius, cavity depth, unit weight of material and cohesion so that results correspond always to the five distinct cases of scaled cohesion (notice the five different values considered along the horizontal axis in Figure 4.5, these corresponds to values of $\tilde{c}$ equal to 0.2, 0.5, 1, 2 and 5) and the four distinct cases of scaled cavity depth (notice the four different lines considered in Figure 4.5, these corresponds to values of ξ equal to 1.5, 2, 3, and 4).

In Figure 4.5, the symbols representing the numerical (FLAC®) results are shown to be located always just above the corresponding lines computed with Caquot's solution. This means that Caquot's solution predicts lower factors of safety than FLAC®. This is the expected result, since as discussed in Chapter 2 (and Appendix A), Caquot's solution is a lower bound solution, and therefore a conservative solution compared with the actual solution, that in this case, and as mentioned earlier on, is assumed to be the one given by FLAC® (see also the discussion about Lower and Upper bound solutions in Section 1.2.1 in the 'Introduction' chapter in this thesis).

To quantify the difference in results, the ratio of factors of safety corresponding to the numerical (FLAC®) models and the analytical (Caquot's) models will be denoted as $f_{FS}^{N\text{-}A}$

$$f_{FS}^{N\text{-}A} = \frac{FS\ [\text{Numerical – FLAC}^{®}]}{FS\ [\text{Analytical – Caquot}]} \tag{4.1}$$

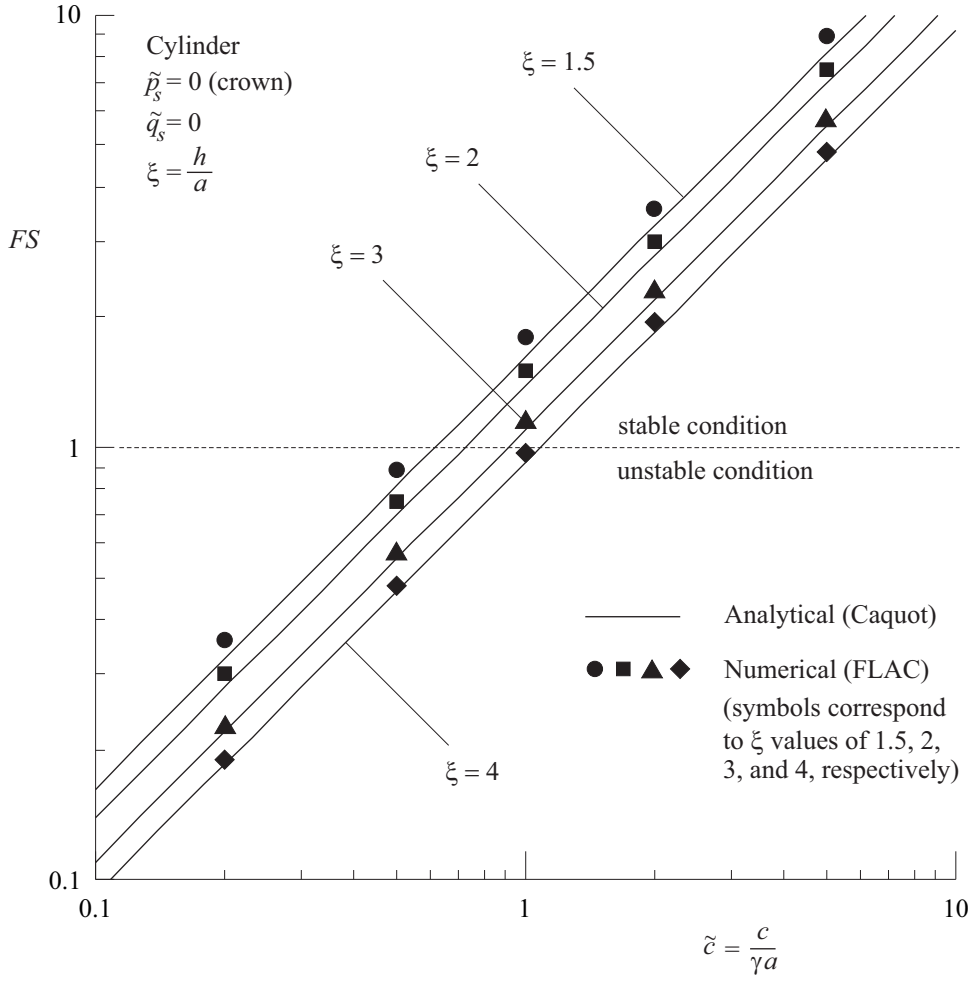

Figure 4.5: Comparison of numerical and analytical results for cylindrical cavities, using a similar representation as in Figure 2.4

Figure 4.6 graphically represents the relationship between the ratio $f_{FS}^{N\text{-}A}$ (vertical axis) and the scaled cohesion, $\tilde{c}$, (horizontal axis) for the same cases included in Figure 4.5. Figure 4.6 indicates that the ratio $f_{FS}^{N\text{-}A}$ is bounded in the approximate range 1 to 1.15 but increases with scaled cavity depth, remaining more or less constant and independent of the value of scaled cohesion, $\tilde{c}$. The reason of the increased differences between numerical and analytical results

is suspected to be in part due to the decreased accuracy of the FLAC® models when cavities with increasing depth are considered, maintaining the same size of elements in the mesh. The reason of these increased differences may also be of a more fundamental nature (e.g., Caquot's solution may be losing accuracy as cases of deeper cavities are considered). In any case, this is a finding that would require further investigation, and that for reasons of limiting the scope of this research work, it is left as a possible independent topic for future research.

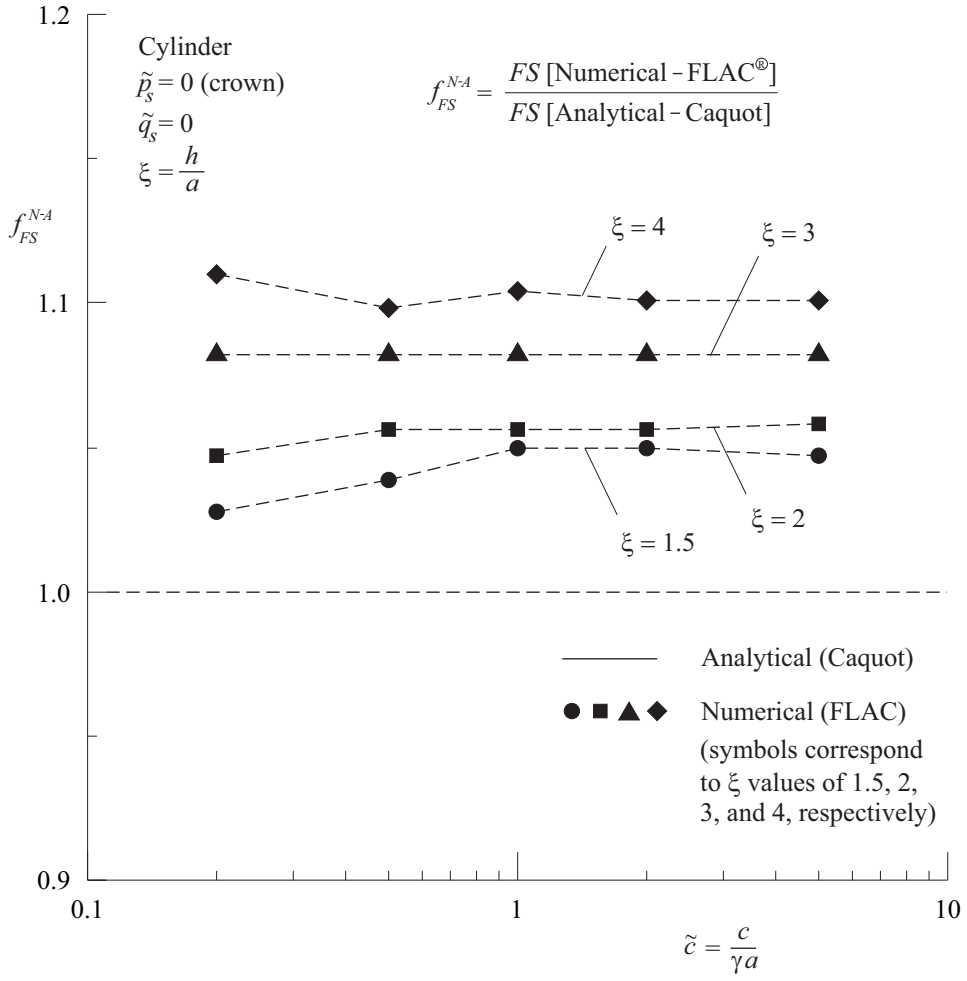

Figure 4.6: Ratio of factors of safety obtained with numerical and analytical models, as represented in Figure 4.5

4.2.2 Cavity type. Cylindrical and spherical cavities

The previous section presented a comparison of numerical and analytical results for the case of cylindrical cavities. In this section, the comparison is extended to the case of spherical cavities.

Figure 4.7 is equivalent to Figure 4.5 but represents factor of safety results for both cylindrical and spherical cavities with scaled depths $\xi = 2.5$ (and $\tilde{q}_s = 0$ and $\tilde{p}_s = 0$, as in the case of Figure 4.5). The symbols represent the results obtained with FLAC®, while the lines represent the results obtained with Caquot's solution. Again, and as expected, the symbols representing the numerical results are shown to be located always just above the corresponding lines computed with Caquot's solution.

Figure 4.8 represents the relationship between the ratio $f_{FS}^{N\text{-}A}$, given by Equation 4.1, (vertical axis) and the scaled cohesion, $\tilde{c}$, (horizontal axis) for the results represented in Figure 4.7. Figure 4.6 indicates that the ratio $f_{FS}^{N\text{-}A}$ corresponding to spherical cavity is larger than the ratio corresponding to cylindrical cavities. The reason of the difference is suspected to be due to the accuracy of the FLAC® models when the axi-symmetric option for spherical cavities is used (compared with the default plane-strain option used for cylindrical cavities). This is another finding that would require further investigation, and that for reasons of limiting the scope of this thesis work, it is left as a possible independent topic for future research.

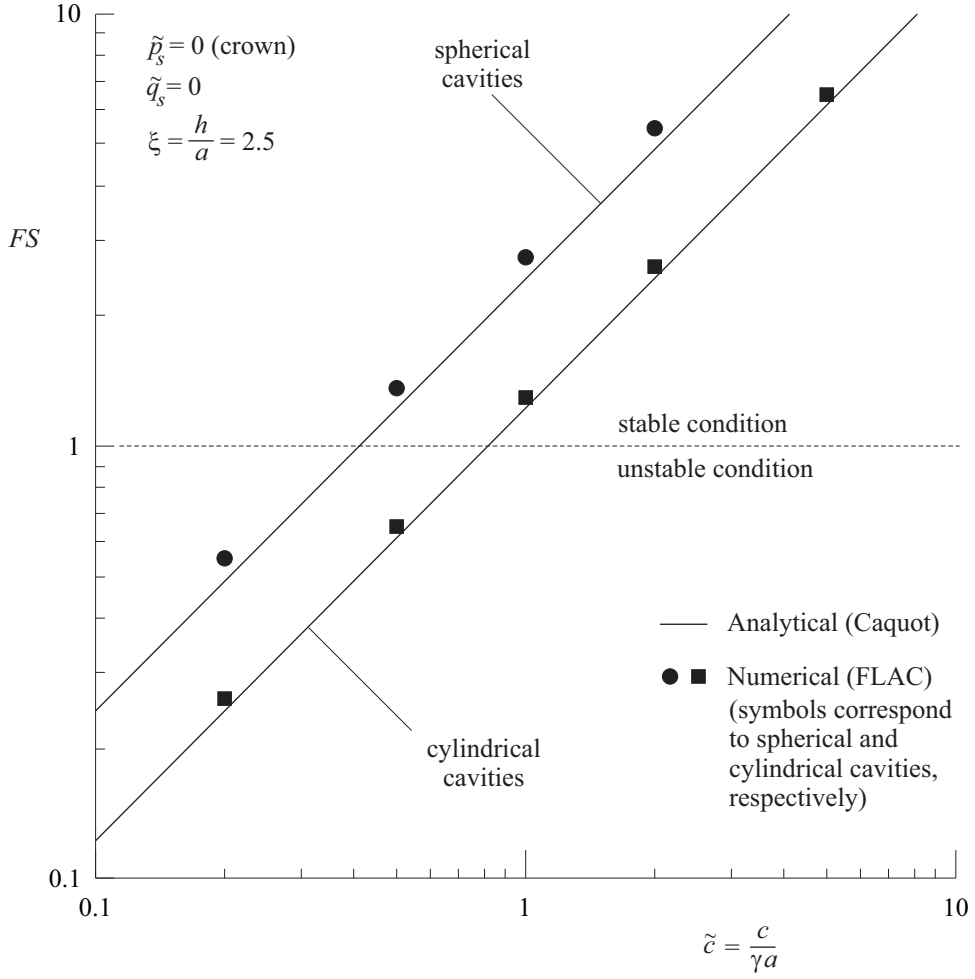

Figure 4.7: Comparison of numerical and analytical results for cylindrical and spherical cavities, using a similar representation as in Figures 2.4 and 2.5

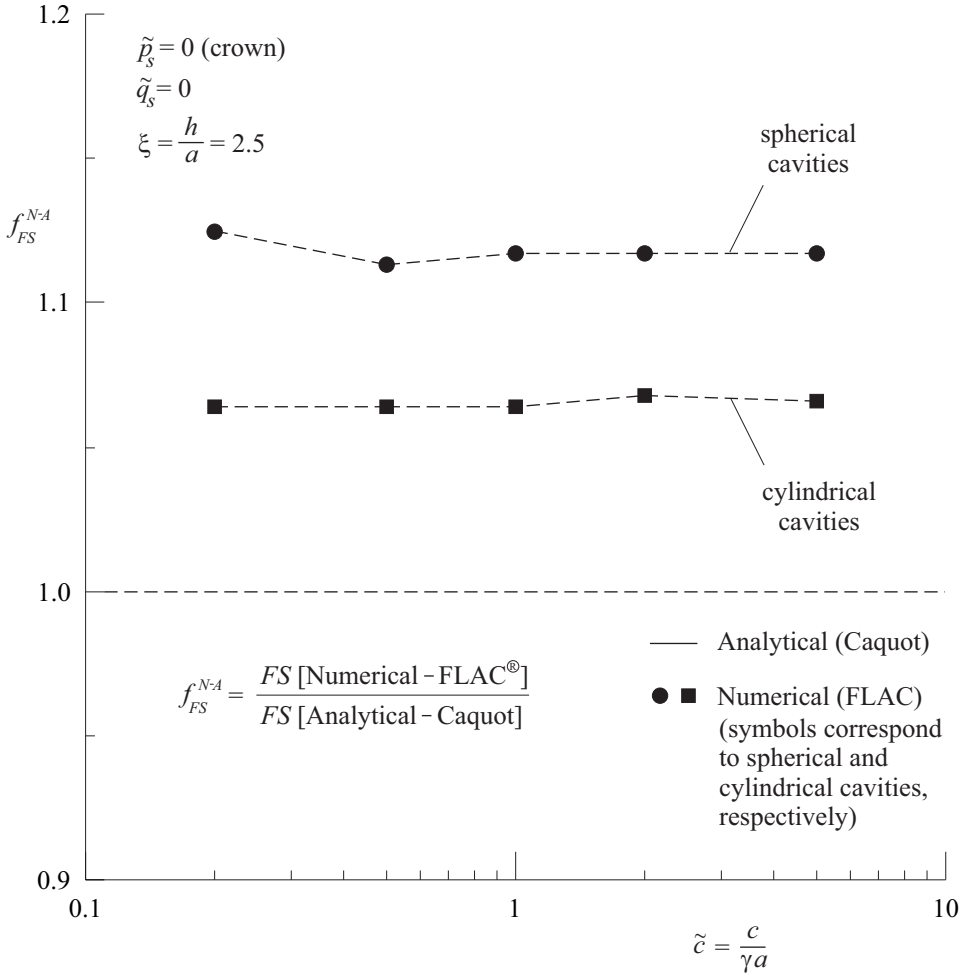

Figure 4.8: Ratio of factors of safety obtained with numerical and analytical models for cylindrical and spherical cavities, as represented in Figure 4.7

4.2.3 Uniform vs. Caquot's internal pressure distribution

The extended Caquot's solution presented in Chapter 2.2 indicated that the support pressure varies hydrostatically from the crown of the cavity to the invert of the cavity, as if the support pressure was provided by an imaginary fluid that has the same unit weight as the material surrounding the cavity. The effect of considering a *uniform* distribution of cavity support pressure in FLAC® models, as compared with the *hydrostatic* distribution assumed in Caquot's model is investigated below.

Figure 4.9 represents three cases of support pressure distributions to be considered, namely, Case PD#1, Case PD#2 and Case PD#3.

Case PD#1 corresponds to Caquot's hydrostatic internal pressure distribution (compare Figure 4.9 with Figure 2.1 in Chapter 2). If the support pressure at the crown of the cavity is denoted as $p_s^{A\#1}$, then the support pressure at the spring line of the cavity is

$$p_s^{C\#1} = p_s^{A\#1} + \gamma a \tag{4.2}$$

and the support pressure at the invert of the cavity is

$$p_s^{D\#1} = p_s^{A\#1} + 2\gamma a \tag{4.3}$$

Case PD#2 corresponds to a uniform support pressure distribution (see Figure 4.9). If the support pressure at the crown of the cavity is denoted as $p_s^{A\#2}$ and is considered to be equal to the support pressure at the crown for Case PD#1 (i.e., $p_s^{A\#2} = p_s^{A\#1}$), then the support pressure at the spring line and at the invert of the cavity are all equal to $p_s^{A\#2}$

$$p_s^{C\#2} = p_s^{D\#2} = p_s^{A\#2} = p_s^{A\#1} \tag{4.4}$$

Case PD#3 corresponds also to a uniform support pressure distribution (see Figure 4.9), but this time the support pressure at the crown of the cavity, denoted as $p_s^{A\#3}$, is considered to be equal to the support pressure at the spring line for Case PD#1 (i.e., $p_s^{A\#3} = p_s^{C\#1}$). Therefore, in

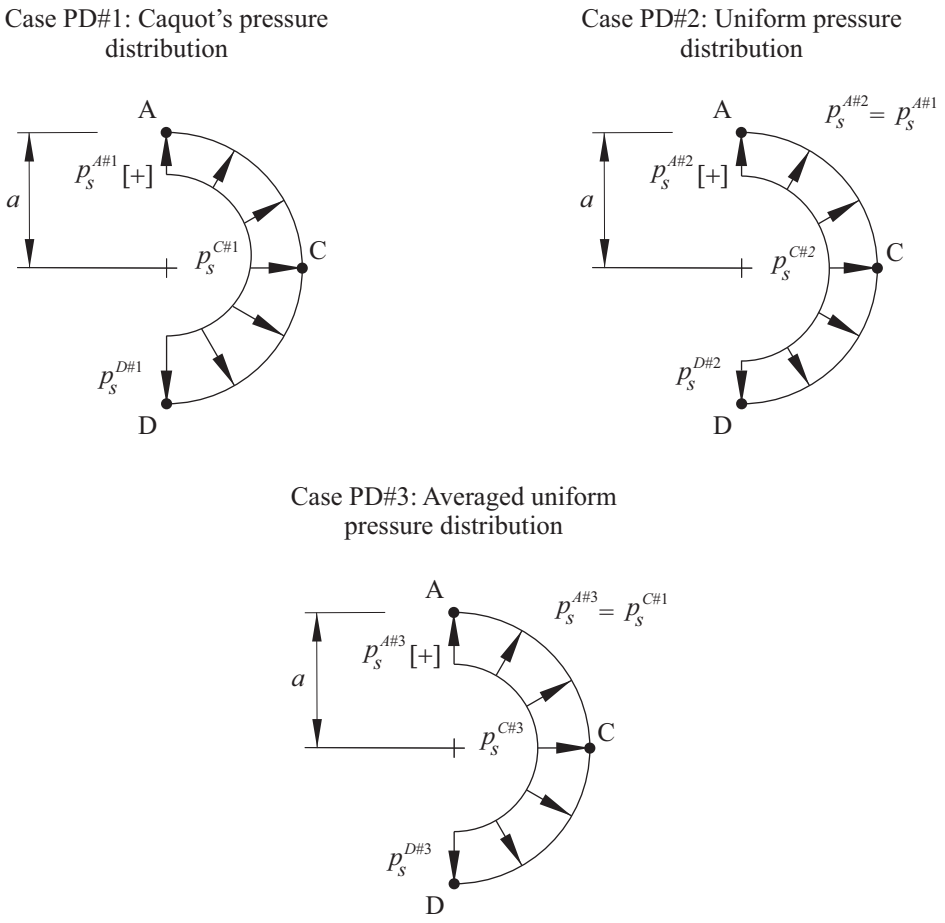

Figure 4.9: Graphical representation of three cases of internal pressure considered for the numerical models. Case PD#1: Caquot's pressure distribution; Case PD#2: uniform pressure distribution; and Case PD#3: averaged uniform pressure distribution

Case PD#3, the support pressure at the spring line and at the invert of the cavity are all equal to $p_s^{A\#3}$

$$p_s^{C\#3} = p_s^{D\#3} = p_s^{A\#3} = p_s^{C\#1} \tag{4.5}$$

Figure 4.10 is equivalent to Figure 4.7 and applies to cylindrical cavities at scaled depth $\xi = 2.5$, with zero ground surcharge load ($\tilde{q}_s = 0$). The three cases of support pressure distribution in Figure 4.9 have been solved with FLAC® and these results are represented with symbols in Figure 4.10 (the discontinuum lines linking the symbols are included for reference only). The results represented in Figure 4.10 correspond to the case in which the support pressure at the crown of the cavity for Caquot's distribution (Case PD#1 in Figure 4.9, is equal to zero, $p_s^{A\#1} = 0$). Consequently, the results in Figure 4.10 consider that for Case PD#2 (in Figure 4.9) there is no support pressure (as per Equation 4.4, $p_s^{A\#2} = p_s^{A\#1}$) in the cavity, and that for case Case PD#3 (in Figure 4.9), the support pressure is uniform, and equal to $p_s^{C\#1}$ (see Equation 4.5), and therefore is equal to γa (see Equation 4.2).

Referring to Figure 4.10, comparing the relative position of the symbols representing the FLAC® results for the Cases PD#1, PD#2 and PD#3, with the full line representing analytical results, the following observations are made.

With regard to Case PD#1 in Figure 4.9, Caquot's analytical solution predicts factors of safety that are conservative, or on the safe side, as discussed already in Sections 4.2.1 and 4.2.2.

With regard to Case PD#2 in Figure 4.9, Caquot's analytical solution predicts factors of safety that are unconservative, or on the unsafe side (note that the symbols for Case PD#2 in Figure 4.10 are located below the line representing Caquot's solution).

With regard to Case PD#3 in Figure 4.9, Caquot's analytical solution predicts factors of safety that are even more conservative, or more on the safe side than for Case PD#1 (note that the symbols for Case PD#3 in Figure 4.10 are located above the symbols corresponding to Case PD#1).

Figure 4.11, which is equivalent to Figures 4.6 and 4.8 discussed earlier on, represents

the relationship between the ratio $f_{FS}^{N\text{-}A}$, given by Equation 4.1, (vertical axis) and the scaled cohesion, $\tilde{c}$, (horizontal axis) for the results represented in Figure 4.10.

Figures 4.10 and 4.11, suggest that if the extended Caquot's solution will be applied to solve the case of a cavity that has uniform support pressure (and not the hydrostatic support pressure considered by Caquot's model), then the value of uniform pressure to consider is that corresponding to the value of Caquot's support pressure at the spring line of the cavity (Case PD#3 in Figure 4.9) and not the value of Caquot's support pressure at the crown of the cavity (Case PD#2 in Figure 4.9).

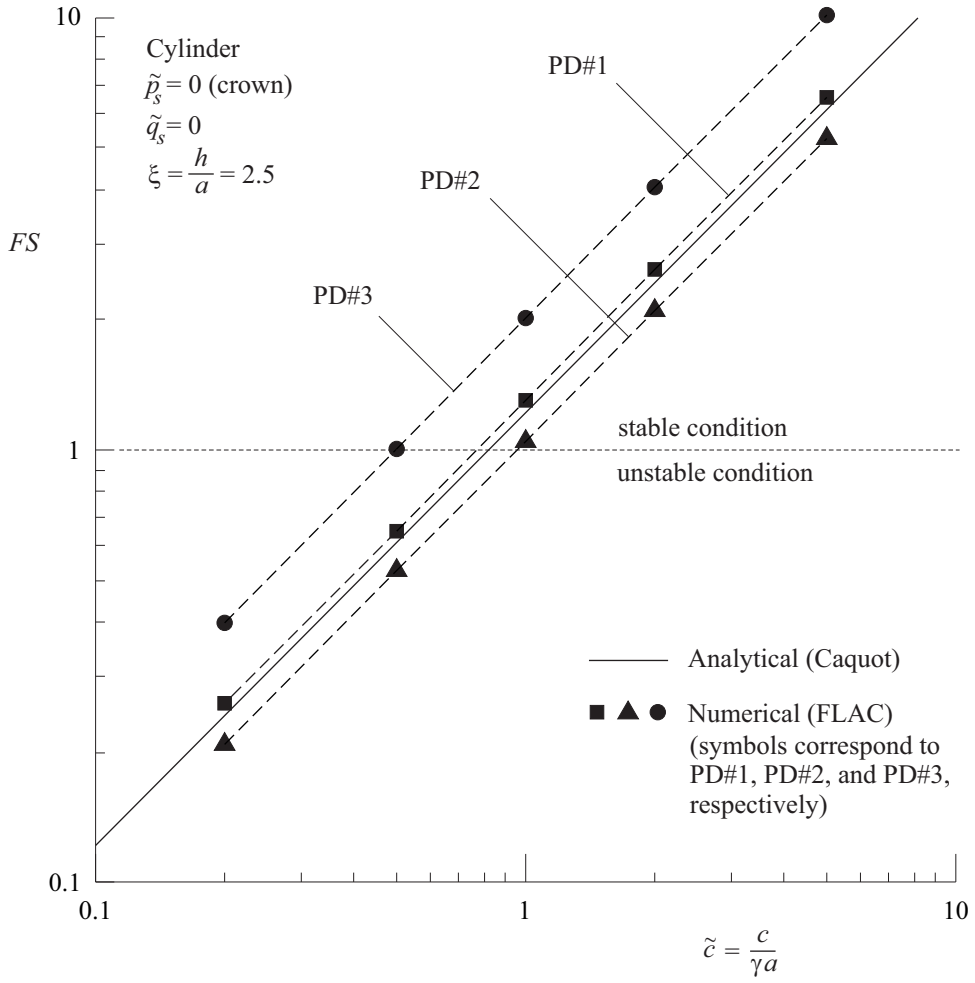

Figure 4.10: Comparison of numerical and analytical results for the different cases of internal pressure distribution represented in Figure 4.9

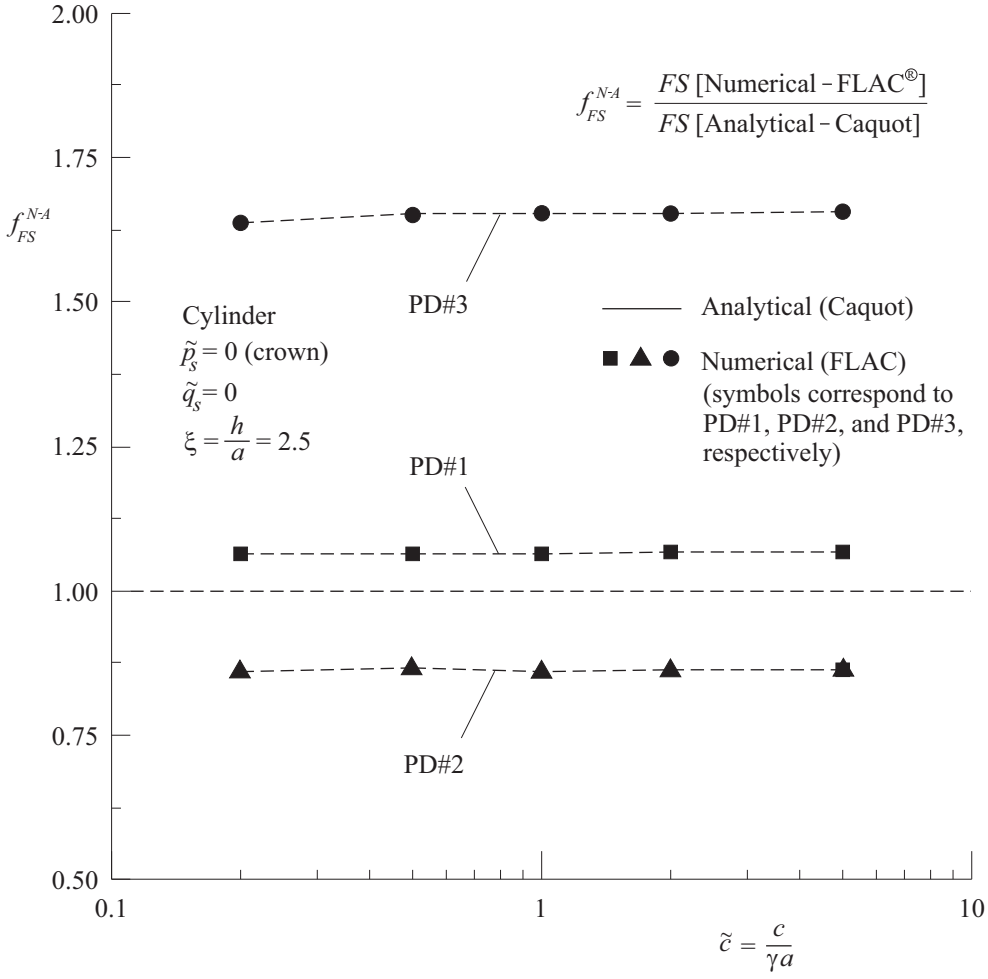

Figure 4.11: Ratio of factors of safety obtained with numerical and analytical models, as represented in Figure 4.10

4.2.4 Density of the mesh in the numerical model

As discussed in Section 1.2.2 in Chapter 1, it is well known that the quality of discretization in a finite difference or finite element numerical model has an effect on the quality of results, and that the smaller the size of elements in the mesh, the more accurate the results become.

First, it must be noted that the sizes of elements considered in the FLAC® models discussed in previous sections, correspond to the sizes of elements shown in Figure 4.1. In particular, the ratio of length of elements in the "Inner region" (in which the elements are square) divided by the radius of the cavity, a, were considered to be always equal to 0.1 (this value 0.1 will be referred to below as the 'reference' scaled element size).

To assess the effect of changing the element size in the mesh of the models on the resulting factors of safety, the same case of a cylindrical cavity at a scaled depth, $\xi = 2.5$, discussed in Section 4.2.2 is considered. A particular value of scaled cohesion, $\tilde{c}$, is selected to be 1 (this value lies in the middle value in the horizontal axis of Figure 4.7). Also, zero values of scaled ground surcharge load and support pressure at the cavity crown are considered ($\tilde{q}_s = 0$ and $\tilde{p}_s = 0$, respectively).

Different scaled element sizes for the FLAC® models, values smaller and larger than the reference scaled size value 0.1 mentioned above, are considered. These values are 0.025, 0.25 and 0.5.

Figure 4.12 represents the relationship between the ratio $f_{FS}^{N\text{-}A}$, given by Equation 4.1, (vertical axis) and the scaled values of element size in the numerical models. The dot labeled as 'reference' element size corresponds to the value 0.1. Figure 4.12 indicates that the factor of safety obtained with the numerical models improve and become asymptotic to the values predicted by the extended Caquot's solution, as smaller element sizes in the mesh are considered. The results in Figure 4.12 suggest that the 'reference' scaled element size that was used in most of the modelling work done in this thesis (and which was chosen based on experience) can be expected to produce reasonable results.

Although further investigation on the effect of mesh size for other cavity conditions (such as different values of depth, support pressure, surcharge, and others) is needed to determine the optimum element size to use (even perhaps a size smaller than the ‘reference’ element size used in most of the modelling work in this thesis), for reasons of limiting the scope of this research work, this topic is left as another possible independent topic for future research.

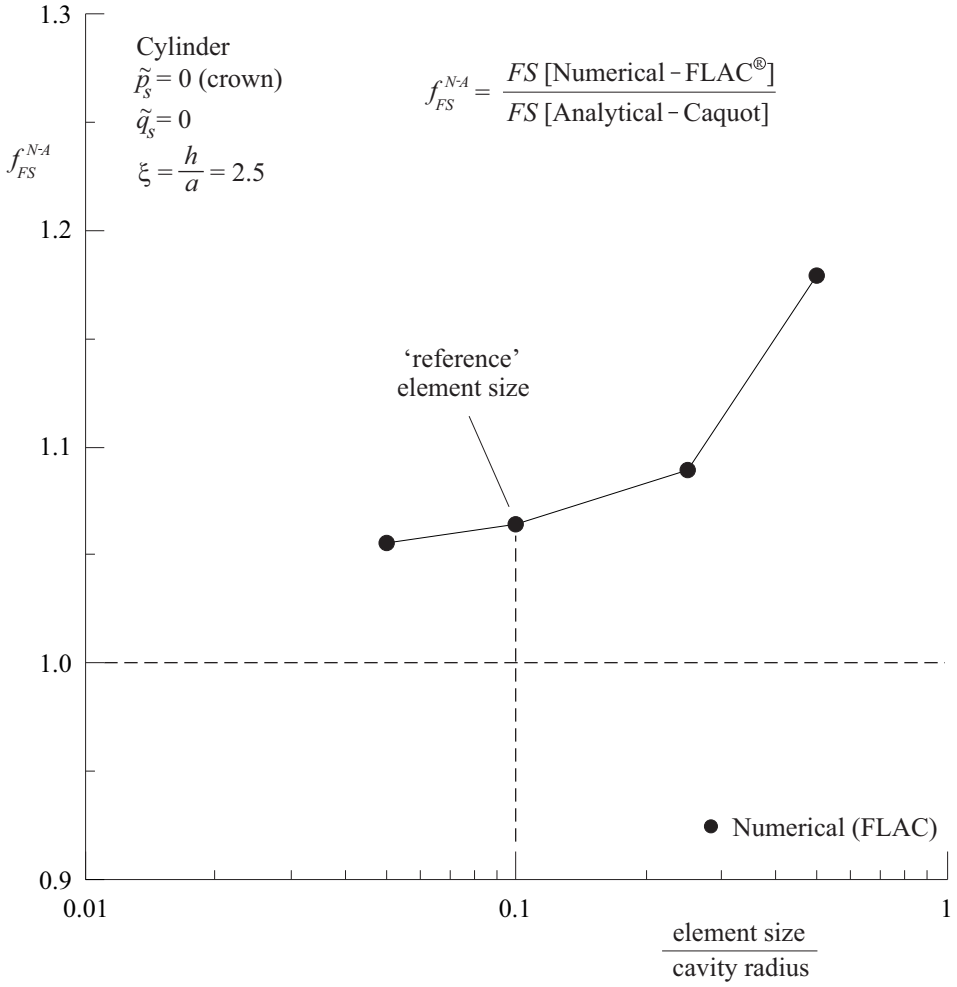

Figure 4.12: Ratio of factors of safety obtained with numerical and analytical models as a function of the element size considered in the numerical model mesh. 'Element size' refers to the side-length of the square elements in the 'inner region' of the mesh in Figure 4.1

Chapter 5

Conclusions

In the preceding chapters, all objectives stated in Section 1.3 in the 'Introduction' chapter of this thesis have been addressed. The most relevant findings of this research are outlined below.

The closed form solutions for factor of safety for cavities in dry ground and ground with water presented in Chapters 2 and 3, showed that the value of factor of safety for spherical cavities is always twice the value of factor of safety for cylindrical cavities (certainly, when all other input variables such as ground cohesion, cavity internal pressure, ground surface surcharge load, elevation of ground surface, etc., are the same).

Chapters 2 and 3 showed that the factor of safety for a shallow cavity decreases as the depth of the cavity increases. This somehow counterintuitive observation can be explained by the fact that as the cavity depth increases, the magnitude of loading around the cavity increases, and therefore the 'ease' for a plastic zone to develop and extend to the ground surface to produce instability also increases.

Chapter 2 revealed that there exists a theoretical minimum scaled depth for an unsupported cavity with no ground surcharge load for which the factor of safety is bounded and is a maximum. This theoretical minimum corresponds to the hypothetical situation in which the crown of the circular cavity has zero thickness. Unsupported cavities at larger scaled depths will all

have factors of safety below this absolute maximum.

Chapter 2 also revealed the dependence of the factor of safety with considered mechanical internal pressure for the cavity. When the internal pressure equals the pressure associated with the original in-situ stresses, the factor of safety tends to infinity (such case is equivalent to excavating the cavity, but immediately reinstalling the original stresses before excavation as if no excavation has taken place). Cavities with lower internal pressure will all have lower factors of safety.

Appendix A, which was included to provide a derivation for the solution presented in Chapter 2 also provided some relevant findings. For the case in which the lateral earth coefficient is equal to one (i.e., when the in-situ vertical stresses are equal to the in-situ horizontal stresses), there exists continuity of stresses at the boundary of the integration circle. This means that the extended Caquot's solution is actually a statically admissible solution and therefore a lower bound solution of limit analysis (see discussion about *field stress* and *limit analysis* solutions in Section 1.2.1).

Chapter 3 revealed that the factor of safety for a *flooded* cavity, whether the water surface is above or below the ground surface, always leads to a higher factor of safety than for a cavity in dry ground (again, all the other input variables being the same). Flooded cavities for which the water surface is above the ground surface, yield a factor of safety that is typically two times higher than the factor of safety for the corresponding cavity in dry ground, independently of how high above the ground surface the water surface is. This finding is comparable with the one found in soil mechanics literature for the classic problem of infinite slopes, which states that the factor of safety for an infinite slope in dry ground is typically two times larger than the factor of safety for the same infinite slope when an inclined phreatic surface is considered to coincide with the inclined slope face (Coduto et al., 2011).

Also, provided the ground has infinite tensile strength to avoid the expected failure due to tensile 'pulling' of radial effective stresses on the cavity wall, the factor of safety for a *dry* cavity

(again, whether the water surface is above or below the ground surface) always leads to a lower factor of safety than for a cavity in dry ground (again, all the other input variables being the same).

Chapter 4 confirmed that the extended Caquot's solution is a lower bound solution. Factors of safety obtained numerically with the finite difference software FLAC® and the strength reduction technique, which as explained in Section 1.3 could be regarded as being closer to the 'actual' factor of safety (when the size of elements in the mesh is small enough), were always slightly larger than (within approximately 10%) the ones obtained with the extended Caquot's solution.

In summary, this theoretical investigation and development of the extended version of Caquot's solution for the stability of shallow cavities produced several relevant findings that could assist in the understanding and prevention of collapses of shallow cavities, a motivation of this thesis work, as it was discussed in Section 1.1 in the 'Introduction' chapter.

Certainly, the work presented in this thesis is not complete and leaves room for further research. For example, in Chapter 4, several issues related to application of numerical models to assess the factor of safety of shallow cavities were identified as requiring further investigation. With regard to the theoretical developments in Chapters 2 and 3, the analysis could be extended to other constitutive models applicable to the design of shallow cavities, such as the case in which the ground is assumed to obey the general Mohr-Coulomb model or the Hoek-Brown model (as discussed in Section 1.2.1, in Chapter 1, the former is a commonly used failure criterion for soils, while the second is a commonly used criterion for intact rock and rock masses).

The developments in this thesis also set the stage for further research into more practical oriented research, involving the application of the extended Caquot's solution for the design of shallow cavities utilizing a factor of safety as the main indicator for stability. The approach could be potentially applicable to design of tunnel support when using mechanized systems such as the *Earth Pressure Balance* and *Slurry Shield* methods discussed in Section 1.1 (Chapter 1).

Also, the incorporation of a factor of safety as a primary parameter dictating stability of shallow underground cavities, allows incorporation of probabilistic techniques such as at the commonly used *Monte-Carlo* method in the practical design of support systems for shallow cavities to account for uncertainty and variability of input properties of the ground.

References

Abramson, L.W., Thomas, S. L., Sharma, S. & Boyce, G.M. 2002. *Slope Stability and Stabilization Methods* (Second ed.). John Wiley & Sons.

Anagnostou, G. & Kovari, K. 1996. Face stability conditions with earth-pressure-balanced shields. *Tunnelling and Underground Space Technology 11*(2), 165–173.

Atkinson, J. H. & Potts, D. 1977. Stability of a shallow circular tunnel in cohesionless soil. *Geotechnique 27*(2), 203–215.

Brady, B. H. G. & Brown, E. T. 2004. *Rock Mechanics for Underground Mining*. Dordrecht/Boston/London: Kluwer Academic Publishers.

Caquot, A. 1934. *Équilibre des massifs a frottement interne*. Paris: Gaunthier-Villars.

Carranza-Torres, C. 1998. *Self-Similarity Analysis of the Elasto-Plastic Response of Underground Openings in Rock and Effects of Practical Variables.* Ph. D. thesis, University of Minnesota.

Carranza-Torres, C. 2004. Report to Geodata S.p.A., Turin, Italy: Computation of factor of safety for shallow tunnels using caquot's lower bound solution. Technical report, Itasca Consulting Group, Minneapolis.

Carranza-Torres, C., Reich, T. & Saftner, D. 2013. Stability of shallow circular tunnels in soils

using analytical and numerical models. In J. Labuz & J. Bentler (Eds.), *Proceedings of the 61st Anunual Geotechnical Engineering Conference*, Minnesota.

Clay, R. B. & Takacs, A. P. 1997. Anticipating the unexpected - flood, fire overbreak, inrush, collaspe. In *Proceedings of the International Conference on Tunnelling under Difficult Ground and Rock Mass Conditions*, Basel, Switzerland, pp. 223–242.

Coduto, D. P., Yeung, M. C. & Kitch, W. A. 2011. *Geotechnical Engineering: Principles and Practices. Second Edition.* Pearson.

Davis, E. H., Gunn, M. J., Mair, R. J. & Seneviratne, H. N. 1980. The stability of shallow tunnels and underground openings in cohesive material. *Geotechnique 30*(4), 397–416.

Davis, R. O. & Selvadurai, A. P. S. 2002. *Plasticity and Geomechanics*. Cambridge University Press.

Dawnson, E., Roth, W. & Drescher, A. 1999. Slope stability analysis by strength reduction. *Geotechnique 49*(6), 835–840.

Fairhurst, C. & Carranza-Torres, C. 2002. Closing the circle. In J. Labuz & J. Bentler (Eds.), *Proceedings of the 50th Anunual Geotechnical Engineering Conference*, Minnesota. (Available for downloading at 'Fairhurst Files', www.itascacg.com).

Guglielmetti, V., Grasso, P., Mahtab, A. & Xu, S. 2008. *Mechanized Tunnelling in Urban Areas: Design Mecthodology and Construction Control*. London.

Hoek, E. & Brown, E. T. 1980. Empirical strength criterion for rock masses. *ASCE J. Geotech. Eng. Div. 106*(GT9), 1013–1035.

Hoek, E. & Brown, E. T. 1997. Practical estimates of rock mass strength. *International Journal of Rock Mechanics and Mining Sciences 34*(8), 1165–1186.

Itasca, I. 2011. *FLAC (Fast Lagrangian Analysis of Continua) Version 7.0*. Minneapolis, Minnesota: Itasca Consulting Group, Inc.

Jaeger, J. C. & Cook, N. G. W. 1979. *Fundamentals of Rock Mechanics* (Third ed.). London: John Wiley & Sons.

Jaeger, J. C., Cook, N. G. W. & Zimmerman, R. 2007. *Fundamentals of Rock Mechanics* (Fourth ed.). Blackwell Publishing.

Kirsch, E. G. 1898. Die theorie der elastizität und bedürfnisse der festigkeitslehre. *Zeitschrift des Vereines Ddeutscher Ingenieure 42*, 797–807.

Lamé, G. 1852. *Lecǫns sur la théorie de l´elasticité*. Paris: Gaunthier-Villars.

Oden, J. T. 1990. *A History of Scientific Computing*. Association for Computing Machinery, Inc.

Potts, D. M. & Zdravkovic, L. 1999. *Finite Element Analysis in Geotechnical Engineering. Theory*. London: Thomas Telford.

Terzaghi, K. 1943. *Throretical Soil Mechanics*. New York: John Wiley & Sons, Inc.

Terzaghi, K. 1946. *Rock defects and loads on tunnel supports, Rock tunneling with steel supports*. Youngstown, Ohio: Commercial Shearing and Stamping Co.

Terzaghi, K., Peck, R. & Mesri, G. 1996. *Soil Mechanics in Engineering Practice*. New York: John Wiley & Sons, Inc.

Vermeer, P.A., Ruse, N. & Marcher, T. 2002. Tunnel heading stability in drained ground. *Felsbau 20*(6), 8–18.

Appendix A

Derivation of Caquot's solution for dry ground

The objective of this appendix is to present the derivation of the equations conforming the extended Caquot's solution for dry ground, as presented in Section 2.2 in Chapter 2.

Caquot's solution is obtained by integrating force equilibrium equations (including self-weight of the material) for the radial and tangential directions, throughout the integration circle around the cavity in Figure 2.1. As discussed in Section 2.1 (Chapter 2), the cavity represented in Figure 2.1 accounts for either the case of a cylindrical cavity under plane-strain conditions, for which the out-of-plane stress is an intermediate principal stress, or a spherical cavity under spherical symmetry, for which the out-of-plane stress is equal to the on-plane hoop stress. The partial differential equations representing equilibrium of forces in the radial and tangential directions in terms of the scaled normal stresses (when the shear stresses are disregarded, as discussed when referring to Figure 2.1 in Section 2.1) and the scaled radial distance introduced in Section 2.2 are written as (Jaeger & Cook, 1979)

$$\frac{\partial \tilde{\sigma}_r}{\partial \rho} + k\,\frac{\tilde{\sigma}_r - \tilde{\sigma}_\theta}{\rho} + \sin\theta = 0 \tag{A.1}$$

and

$$\frac{1}{\rho}\frac{\partial \tilde{\sigma}_\theta}{\partial \theta} + \cos\theta = 0 \tag{A.2}$$

In Equation A.1, the variable k takes a value of 1 for the case of cylindrical cavities and the value 2 for the case of spherical cavities.

A.1 Solution of stresses along cavity crown-surface segment

This section presents the solution of radial and hoop stresses for the crown-surface segment A-B (see Figure A.1). In what follows, stress quantities with the superscript 'AB' will denote stresses evaluated at the crown-surface segment A-B.

A first assumption to be made is that the scaled radial stress, $\tilde{\sigma}_r^{AB}(\rho)$, is a minor principal stress and that the scaled hoop stress, $\tilde{\sigma}_\theta^{AB}(\rho)$, is a major principal stress. Furthermore, the stress state along segment A-B will be assumed to be at plastic failure, so that the Tresca failure criterion applies (see Equations 2.3 and 2.4)

$$\tilde{\sigma}_\theta^{AB} = \tilde{\sigma}_r^{AB} + 2\tilde{c} \tag{A.3}$$

The radial stress along segment A-B is found from integration of Equation A.1 considering $\theta = \pi/2$ (note that with this consideration, Equation A.1 becomes a total differential equation). The integration is done considering Equation A.3 and the following boundary condition

$$\tilde{\sigma}_r^{AB} = \tilde{q}_s \quad \text{at} \quad \rho = \xi \tag{A.4}$$

The following solution for $\tilde{\sigma}_r^{AB}(\rho)$ is obtained

$$\tilde{\sigma}_r^{AB}(\rho) = \tilde{q}_s + \xi - \rho + 2\tilde{c}\,k \ln\frac{\rho}{\xi} \tag{A.5}$$

Also, in view of Equation A.3, the solution for $\tilde{\sigma}_\theta^{AB}(\rho)$ is

$$\tilde{\sigma}_\theta^{AB}(\rho) = \tilde{\sigma}_r^{AB}(\rho) + 2\tilde{c} \tag{A.6}$$

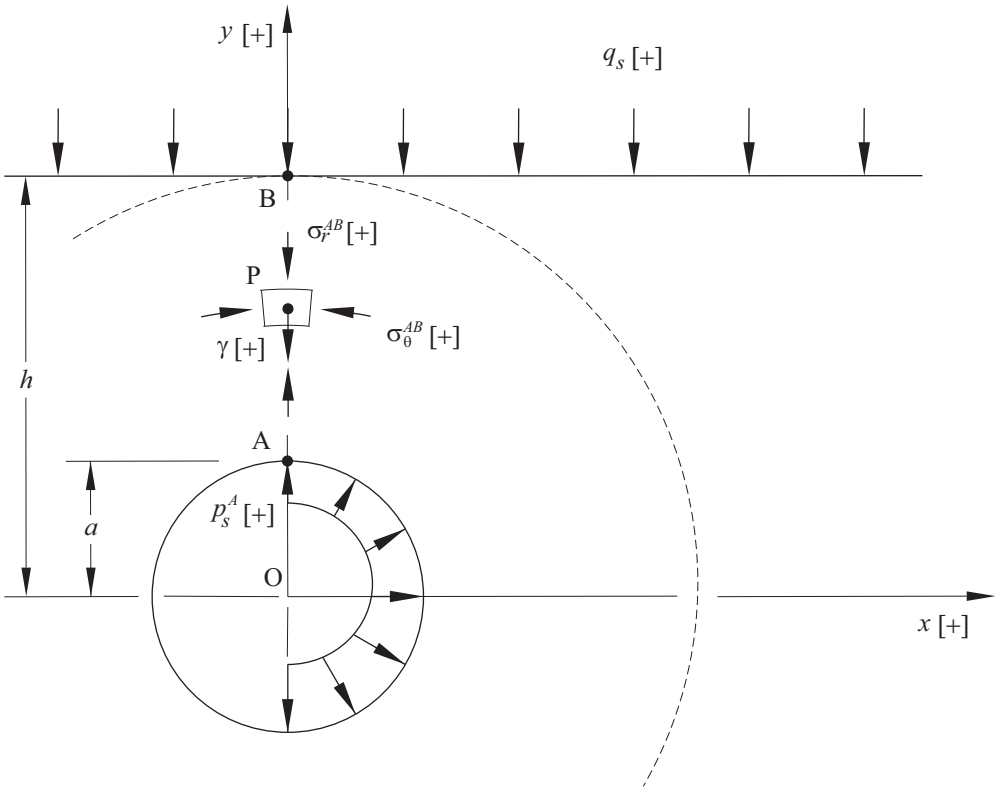

Figure A.1: Extended Caquot's model as applied to the analysis of stability of shallow circular cavities in plastic material, with particular reference to the stresses at the crown-surface segment A-B

The internal pressure at the crown of the cavity required for equilibrium, $\tilde{p}_s^A$, can be obtained from Equation A.5 considering the boundary condition

$$\tilde{\sigma}_r^{AB} = \tilde{p}_s^A \quad \text{at} \quad \rho = 1 \tag{A.7}$$

This gives

$$\tilde{p}_s^A = \tilde{q}_s + \xi - 1 - 2\tilde{c}k \ln \xi \tag{A.8}$$

Equations A.5, A.6 and A.8 are the same Equations 2.12, 2.13 and 2.14 presented in Chapter 2.

A.2 Solution of stresses inside the integration circle

The solution for the scaled hoop stress in the integration circle, $\tilde{\sigma}_\theta(\rho,\theta)$, can be found by integration of the force equilibrium Equation A.2 with respect to θ. This gives

$$\tilde{\sigma}_\theta(\rho,\theta) = -\rho\,\sin\theta + \tilde{C}_1(\rho) \tag{A.9}$$

The solution for the unknown integration function in the equation above, $C_1(\rho)$, is found by considering that Equation A.9 must be equal to Equation A.6 when $\theta = \pi/2$. This gives

$$\tilde{C}_1(\rho) = \rho + \tilde{\sigma}_\theta^{AB}(\rho) \tag{A.10}$$

Substituting Equation A.10 into Equation A.9 results in the following solution for $\tilde{\sigma}_\theta(\rho,\theta)$

$$\tilde{\sigma}_\theta(\rho,\theta) = \tilde{\sigma}_\theta^{AB}(\rho) + \rho\,(1-\sin\theta) \tag{A.11}$$

Note that in Equations A.10 and A.11, $\tilde{\sigma}_\theta^{AB}(\rho)$ is given by Equation A.6.

The solution for the scaled radial stress in the integration circle, $\tilde{\sigma}_r(\rho,\theta)$, can be found by integration of the force equilibrium Equation A.1 with respect to ρ. This gives

$$\tilde{\sigma}_r(\rho,\theta) = \tilde{q}_s + \xi + 2\tilde{c}k\ln\frac{\rho}{\xi} - \rho\,\sin\theta + \rho^{-k}\tilde{C}_2(\theta) \tag{A.12}$$

The solution for the unknown integration function in the equation above, $C_2(\theta)$, is found by considering that Equation A.12 must be equal to Equation A.5 when $\theta = \pi/2$. This gives

$$\tilde{C}_2(\theta) = 0 \tag{A.13}$$

Substituting Equation A.13 into Equation A.12 results in the following solution for $\tilde{\sigma}_r(\rho,\theta)$

$$\tilde{\sigma}_r(\rho,\theta) = \tilde{\sigma}_r^{AB}(\rho) + \rho\,(1-\sin\theta) \tag{A.14}$$

Note that in Equation A.14, $\tilde{\sigma}_r^{AB}(\rho)$ is given by Equation A.5.

With Equations A.11 and A.14, the scaled hoop stress minus the scaled radial stress throughout the integration circle becomes

$$\tilde{\sigma}_\theta(\rho,\theta) - \tilde{\sigma}_r(\rho,\theta) = \tilde{\sigma}_\theta^{AB} - \tilde{\sigma}_r^{AB} = 2\tilde{c} \tag{A.15}$$

In view of Equation A.3, Equation A.14 indicates that in the extended Caquot's solution all material in the integration circle (and not just the material along the segment A-B) is in plastic failure.

Finally, the particular form of the scaled radial stress at the boundary of the integration circle is obtained considering $\rho = \xi$ in Equation A.14. This gives

$$\tilde{\sigma}_r(\xi,\theta) = \tilde{q}_s + \xi\,(1-\sin\theta) \tag{A.16}$$

The equation above is used in the next section to show that Caquot's solution is a statically admissible solution.

A.3 Compatibility of stresses at the boundary of the integration circle

The objective of this section is to show that stresses approaching the integration circle boundary from *within* the integration circle are compatible with the stresses approaching the boundary from *outside* the integration circle as represented in Figure A.2.

Considering Equations 2.1 and 2.2 with $y = a\rho\sin\theta$, and the scaling rule for stresses given by Equations 2.7 and 2.8, the scaled in-situ vertical and horizontal stresses existing outside the integration circle are

$$\tilde{\sigma}_y^o(\rho,\theta) = \tilde{q}_s + \xi - \rho\,\sin\theta \tag{A.17}$$

and

$$\tilde{\sigma}_x^o(\rho,\theta) = K_o\,\tilde{q}_s + K_o\,(\xi - \rho\,\sin\theta) \tag{A.18}$$

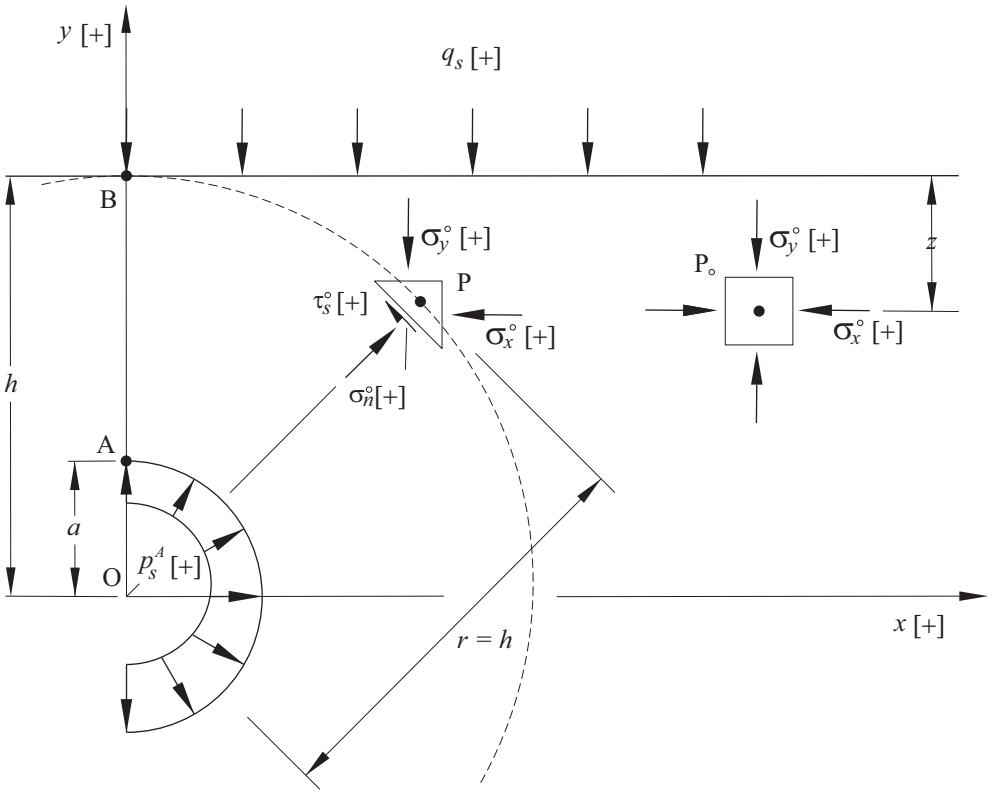

Figure A.2: Extended Caquot's model as applied to the analysis of stability of shallow circular cavities in plastic material, with particular reference to the stresses at the at the boundary of the integration circle

On the integration circle boundary, the scaled in-situ normal and shear stresses can be computed from Equations A.17 and A.18 using the classical stress transformations formulas (Jaeger & Cook, 1979)

$$\tilde{\sigma}_n^o = \tilde{\sigma}_x^o \cos^2\theta + \tilde{\sigma}_y^o \sin^2\theta \tag{A.19}$$

and

$$\tilde{\tau}_s^o = \frac{\tilde{\sigma}_y^o - \tilde{\sigma}_x^o}{2} \sin 2\theta \tag{A.20}$$

Replacing Equations A.17 and A.18, into Equations A.19 and A.20, taking $\rho = \xi$, and considering the particular case $K_o = 1$ (the case in which in-situ horizontal and vertical stresses

are equal), the scaled in-situ normal and shear stresses at the boundary of the integration circle become

$$\tilde{\sigma}_n^o = \tilde{q}_s + \xi\,(1 - \sin\theta) \tag{A.21}$$

and

$$\tilde{\tau}_s^o = 0 \tag{A.22}$$

Equation A.21 is the same Equation A.16, indicating that there is continuity of normal stress at the boundary of the integration circle. Also the fact that the initial shear stress at the boundary of the integration circle is null (Equation A.22) indicates that there is also continuity of shear stresses at the boundary of the integration circle (when $K_o = 1$). Both observations imply that Caquot's extended solution is a statically admissible solution, and therefore an upper bound for the factor of safety defined by Equation 2.20, again when the lateral earth pressure coefficient K_o is equal to one.

Appendix B

Derivation of Caquot's solution accounting for water in the ground

The objective of this appendix is to present the derivation of the equations conforming the extended Caquot's solution that accounts for water in the ground as presented in Section 3.2 in Chapter 3.

For the sake of clarity and space, and in contrast with Appendix A that presents the solution for the full integration circle, this appendix provides the steps required for obtaining the solution of stress quantities by integration of the equilibrium equations along the crown-surface segment A-B only.

B.1 Solution of stresses along cavity crown-surface segment

The two cases discussed in Chapter 3, namely, the cases of water surface above and below the ground surface, are presented separately below.

B.1.1 Case of water surface above or at ground surface

The solution is obtained considering the same equation of equilibrium of forces in the radial direction presented in Appendix A, as given by Equation A.1. The same assumptions discussed in Section A.1 will apply here. Because in the case to be considered here the ground is fully saturated and the scaling rule for stresses given by Equations 2.7 and 2.8 still assume to refer to the dry unit weight of the ground, the equilibrium equation in the radial direction (Equation A.1) which now includes the saturated unit weight of the material, is written in the following form

$$\frac{d\tilde{\sigma}_r^{AB}}{d\rho} + k\,\frac{\tilde{\sigma}_r^{AB} - \tilde{\sigma}_\theta^{AB}}{\rho} + f_{sd} = 0 \tag{B.1}$$

where the coefficient f_{sd} represents the ratio of saturated and unit weight of the material (see Equation 3.10).

The integration of Equation B.1 is done using the following boundary condition

$$\tilde{\sigma}_r^{AB} = \tilde{q}_s^T \quad \text{at} \quad \rho = \xi \tag{B.2}$$

where $\tilde{q}_s^T$ is the scaled total ground surcharge load, that as discussed in Section 3.2 can be decomposed in mechanical and hydraulic parts.

Using the resulting solution for the radial stress, $\tilde{\sigma}_r^{AB}$, the total internal pressure at the crown of the cavity, $\tilde{p}_s^T$, which as also explained in Section 3.1 can be decomposed in mechanical and hydraulic parts, is obtained using the following boundary condition

$$\tilde{\sigma}_r^{AB} = \tilde{p}_s^T \quad \text{at} \quad \rho = 1 \tag{B.3}$$

This gives

$$\tilde{p}_s^T = \tilde{q}_s^T + f_{sd}\,(\xi - 1) - 2\tilde{c}\,k \ln \xi \tag{B.4}$$

Equation B.4 is the same Equation 3.18 presented in Section 3.2.

B.1.2 Case of water surface below or at ground surface

When the water surface is below ground surface at a position ξ_w, two regions are assumed to exist above the ground, a top region where the material is dry, and a lower region where the material is saturated.

For the top region, considering the same assumptions discussed in Section A.1, the equilibrium equation for the radial direction (Equation A.1) which includes the saturated unit weight of the material, is written in the following form

$$\frac{d\tilde{\sigma}_r^{AB}}{d\rho} + k\,\frac{\tilde{\sigma}_r^{AB} - \tilde{\sigma}_\theta^{AB}}{\rho} + 1 = 0 \tag{B.5}$$

Note that in contrast with Equation B.1 that applies to saturated ground, the last term in the equation above is one, rather than f_{sd}.

For the bottom region, where the material is assumed to be saturated, the very same equilibrium equation defined in Section B.1.1(Equation B.1) applies.

Combined integration of Equations B.5 and B.1 is thereafter done using the following boundary conditions:

For the top region (i.e., to the general solution resulting from integration of Equation B.5)

$$\begin{aligned} \tilde{\sigma}_r^{AB} &= \tilde{q}_s^T \quad \text{at} \quad \rho = \xi \\ \tilde{\sigma}_r^{AB} &= \tilde{\sigma}_r^{\xi_w} \quad \text{at} \quad \rho = \xi_w \end{aligned} \tag{B.6}$$

For the bottom region (i.e., to the general solution resulting from integration of Equation B.1)

$$\begin{aligned} \tilde{\sigma}_r^{AB} &= \tilde{\sigma}_r^{\xi_w} \quad \text{at} \quad \rho = \xi_w \\ \tilde{\sigma}_r^{AB} &= \tilde{p}_s^T \quad \text{at} \quad \rho = 1 \end{aligned} \tag{B.7}$$

In Equations B.6 and B.7, $\tilde{\sigma}_r^{\xi_w}$ represents the radial stress at the boundary between dry (or top) and saturated (or bottom) regions.

Application of the procedure described above yields the scaled internal pressure of the cavity required for equilibrium

$$\tilde{p}_s^T = \tilde{q}_s^T + f_{sd}\left(\xi + \xi_w - 1\right) - \xi_w - 2\tilde{c}k\ln\xi \tag{B.8}$$

Equation B.8 is the same Equation 3.19 presented in Section 3.3.